Experimental evaluation of actuation systems for a gait-assistive active orthosis using a test bench

Auteur : Vansighen, Timothée
Promoteur(s) : Bruls, Olivier
Faculté : Faculté des Sciences appliquées
Diplôme : Master en ingénieur civil mécanicien, à finalité spécialisée en génie mécanique
Année académique : 2016-2017
URI/URL : http://hdl.handle.net/2268.2/3258

ATFE0013-1 : Master Thesis

Experimental evaluation of actuation systems for a gait-assistive active orthosis using a test bench

---

Graduation Studies conducted for obtaining the Master's degree in Mechanical Engineering by VANSIGHEN Timothée

University of Liège - Faculty of Applied Sciences
Academic Year 2016 – 2017
August 20, 2017

Academic promoters: Pr. Olivier BRÜLS
Pr. Josep Maria FONT-LLAGUNES

Abstract

The current master thesis takes place in the framework of rehabilitation and reeducation engineering systems. In order to support spinal cord injured subjects in their daily life, a low-cost active knee-ankle-foot orthosis prototype is currently developed within the *Biomechanical Engineering Lab* of the *Universitat Politècnica de Catalunya*.

In order to fulfil the natural knee requirements and to ensure the safest interaction between the subject and the orthosis, the development of a series elastic actuator knee joint is an active research topic. To experimentally estimate the usefulness of such actuator, a test bench has been constructed in the lab. The test bench consists of the actuator to which loads can be submitted to simulate human gait. A series of sensors are used and calibrated to control the system and have reliable measurements.

Investigations of the theoretical dynamic behaviour of the system are done in order to compare with the experimental trials. Tests are used to determine the physical parameters and disturbances influencing the dynamics of the system. It is concluded that friction is highly present and has not to be neglected.

From the energetic point of view, a comparison of the mechanical and electrical energy consumption is done between the actuator with and without the elastic element. On the other hand, an electromagnetic clutch is also implemented on the test bench to lock the system for small knee angle variations. This might decrease the comfort of the patient but also decrease the global energy consumption per gait cycle. Lastly, an electro-mechanical simulation tool of the system is implemented enabling offline results and improving the control.

Contents

1 Introduction

1.1 Motivation

Throughout anyone's life, no one is protected against accidents, paralysis or any other disease that can lead to a significant reduction of mobility. Furthermore, aging, which is biologically inevitable over the years, can also induce many other physical troubles, resulting in the same difficulty in movement.

Affected people often feel isolated. This may lead to the appearance of additional psychological or relational disorders. It is therefore essential that these individuals can benefit from aids tailored to their daily needs to continue to live in the best conditions possible.

Disabled people are, in most of the cases, placed in a wheelchair. Unfortunately, not all wheelchairs are motorized. However, this solution is far to be the most optimal one. Indeed, in addition to the lack of infrastructure, people still lose more physical abilities due to the motionless sitting position in their chair.

A more suitable solution appeared with the emergence of exoskeletons and orthoses. These devices provide the patient with the support in force and in displacement of the members that this one is not able to supply anymore alone. Many types of research have been conducted to provide compatible human-robot exoskeletons to reproduce as accurate as possible the natural biomechanical human gait cycles.

The *Biomechanical Engineering Lab* of the *Universitat Politècnica de Catalunya* is developing the *HYBOR* project which consists in the conception and construction of a prototype of low-cost active knee-ankle-foot orthoses to assist gait of spinal cord injured subjects. This prototype is electrically actuated at the knee joints. The gait cycle is controlled by taking into account the reverse ground reaction torque. Improvements in the reliability and efficiency of the prototype, as well as predictions based on the musculoskeletal system and the inclusion of a series elastic actuator, are still active research topics.

1.2 Goals

The purpose of this research is to evaluate the experimental functioning of the knee actuation system. Three actuation systems are studied: the direct actuation, the series elastic actuation and the clutchable series elastic actuation. Experimental measurements are performed on a test bench to which the actuation system is connected in opposition with a load motor on the same axis. Steady-state, as well as dynamic tests of healthy gait cycle data are conducted.

The test bench has primarily been established to calibrate the sensors to have reliable measurements. Thanks to the experimental trials, the mechanical and electrical performances of the system are evaluated. A comparison of the experimental model and the theoretical model is made through physical parameters identification and simulation.

Eventually, the limitations of the capacities of the actual test bench are defined for further improvements of the system.

1.3 Orthosis prototype

The current master thesis is realised within the framework of the project *HYBOR: Low-cost motor-FES hybrid orthosis for the gait of spinal cord injured subjects and simulation methods to support the design and adaptation.* The project reference is DPI2015-65959-C3-2-R and funded

by the Ministry of Economy and Competitiveness (MINECO) of Spain for the period between January 2016 and December 2018. This project is done in collaboration with the University of La Coruña and the University of Extremadura.

The aim of the prototype is to build a low-cost active knee-ankle-foot orthosis for rehabilitation of patients suffering from spinal cord injuries, in which the knee joint is active while the ankle joint remains passive. The actual prototype is presented in Figure 1a. The knee actuator on the current achieved prototype has a direct transmission composed of an electric DC motor which can be locked during the stance phase of the gait cycle and rotate during the swing phase, as represented in Figure 1b. The system is wearable and controlled by a computer located in the back of the patient. The battery, the motor drivers and the data acquisition system are also located in the back of the patient with the controller. A series of sensors are used for motor rotation controls thanks to encoders and inertial measurement units (IMU) to measure the angular position in the space of each shank of the orthosis and predict motion intention. The inertial measurement units are composed of a gyroscope, an accelerometer and a magnetometer. Furthermore, force sensing resistors are located at the foot plant to measure the foot ground reaction [51].

The active improvement topics are:

1. Increasing the robustness, the usability, the portability and the efficiency of the system.
2. Developing function electrical stimulation (FES) that can activate muscle contraction thanks to small electrical stimulation. This could improve the own capacities of the patient and decrease the influence of the orthosis by coupling the human and the robot power.
3. Evaluating the medical impact of the system to predict its adaptability for as many patients as possible.
4. Enhancing the simulation methods for designing and adaptation thanks to human-like movements analysis.

An improvement of the project concerning the efficiency of the system to reach as much as possible a human-like motion and energy storage efficiency is developed in [12] thanks to a series elastic actuation. To evaluate the accuracy of the actuator and its ability to track a human-like gait, a test bench has been constructed.

(a) Orthosis prototype

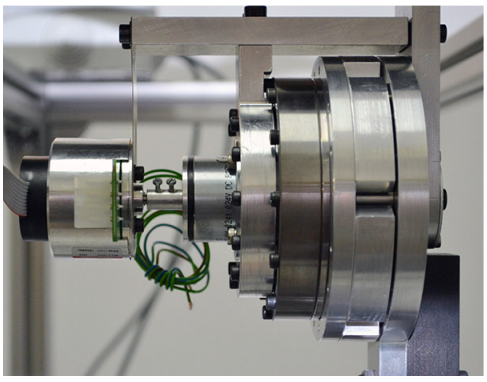

(b) Current actuator

Figure 1 – Current orthosis prototype and actuation system

2 Human gait biomechanics

In this section, the human gait dynamics is detailed from a biomechanical point of view. This analysis is needed to deduce the requirements that the prototype should be able to provide to the patients.

2.1 Neuromuscular signal transmission

The human movements are produced by the neuromusculoskeletal system as represented in Figure 2. Muscles are the only active tissues able to generate force. Tendons allow to connect muscles to bones and transmit the force coming from the muscles. The bones are then able to rotate as lever arms around the joints of the body to produce the desired movements. The muscles themselves consist of a hierarchical structure composed of successively bundles of fascicles, fibers, myofibrils and myofilaments. The execution of a movement is commanded by the brain. In this way, a nervous electrical signal is sent by the brain through the spinal cord. The motor unit contained in the spinal cord transmits the information to the muscle fibers which will contract the muscles in the right way. A feedback control loop enables to change the configuration of movements.

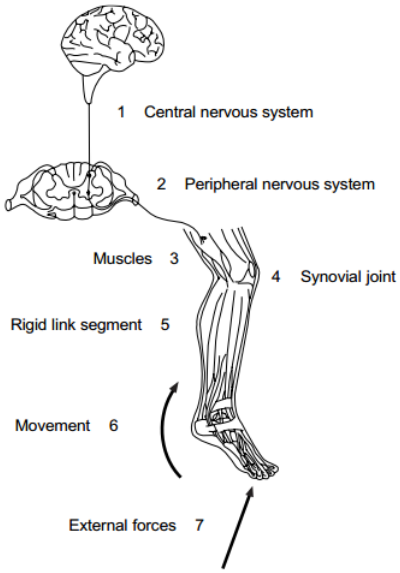

Figure 2 – Functional basis of walking [11]

2.1.1 Troubles induced by spinal cord injuries

Spinal cord injuries prevent the transmission of the information signals from the brain to the muscles. These injuries result in most cases from an accident but may also be the consequence of diseases. Spinal cord injuries are in this way the cause of the appearance of many motor troubles. Rehabilitation treatments are usually provided to the patients suffering from those troubles through kinesiotherapeutic exercises to recover as much autonomy as possible. Robotic devices are also more and more used for those applications for numerous advantages as described in Section 3.

2.2 Human gait cycle

As represented in Figure 3, the human body can be described following three anatomical planes: the coronal (or frontal) plane separating the body into its anterior and posterior parts, the sagittal plane separating the body into its left and right parts and the transverse (or axial) plane

separating the body into its upper and lower parts [40]. The main movements take place in the sagittal plane. The positive sign ankle rotation is the plantar flexion while the negative sign is the dorsiflexion. The hip kinematics is described by three rotational degrees of freedom in the three planes similarly to the ankle joint. The knee is generally outlined by a single rotational joint in the sagittal plane [17].

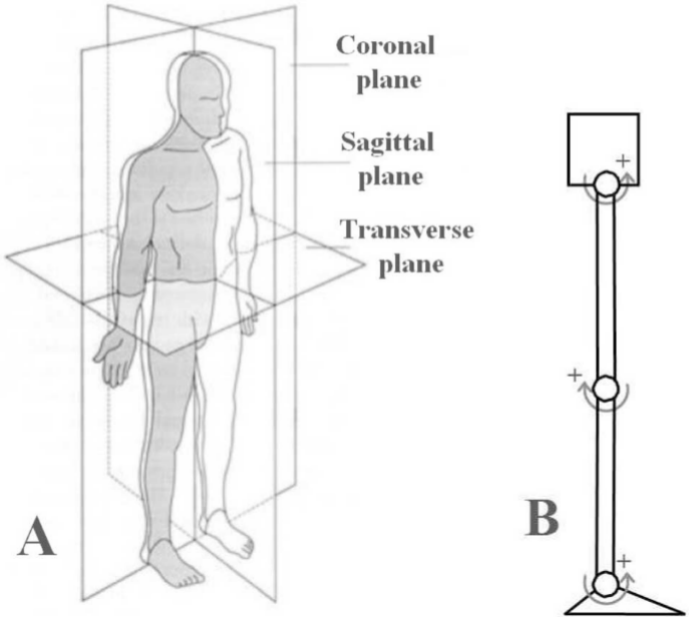

Figure 3 – Anatomical planes according to the human body (A), leg joints representation at rest in the sagittal plane (B) [17]

The human gait cycle is a repeatable sequence. The assumption that all the successive cycles are the same is an acceptable assumption for most of the people in steady-state walking. As represented in Figure 4, the entire human gait cycle is usually analyzed starting from one heel strike to the next one. It can be divided into two main phases [11], [49], [50]:

1. The stance phase: it represents approximately 60% of the gait cycle. The foot is in contact with the ground. This phase can be decomposed in sub-phases:
   — Heel strike: only the heel is in contact with the ground.
   — Foot flat: the entire sole of the foot is in contact with the ground.
   — Midstance: the body weight is supported by a single leg and the other leg swings over the supported one.
   — Heel off: the heel leaves the ground, and the primary support leg is in a pre-swinging movement.
   — Toe off: the primary support foot toe leaves the ground
2. The swing phase: it represents approximately 40% of the gait cycle. The foot is not in contact with the ground, and the leg is swinging to initiate a new gait cycle. This phase can be decomposed in sub-phases:
   — Acceleration: the opposite leg supports the body weight, and the initial leg is swinging.
   — Midswing: highest knee flexion angle when the foot overtakes the body.
   — Deceleration: decrease in the muscular activity to repeat the cycle with a new heel strike.

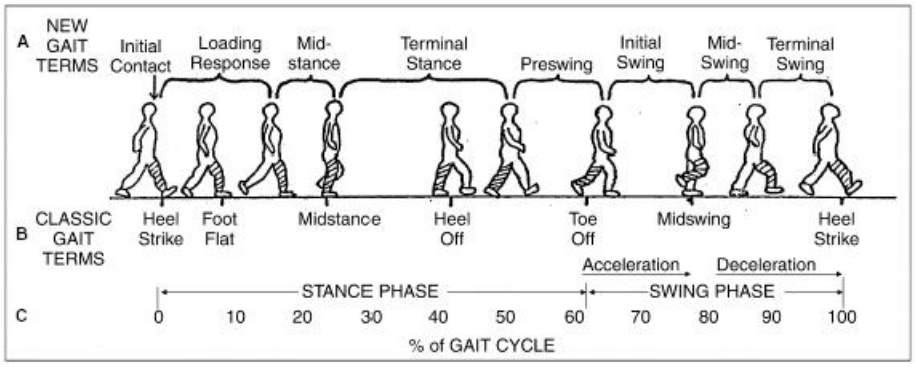

Figure 4 – Normal gait cycle [49]

2.3 Knee requirements

The general shape of the knee flexion angle during one gait cycle is represented in Figure 5. The data varies as a function of the morphology, the speed of walking and the health of each.

During stance phase, the knee is firstly fully extended for the heel strike. By convention, it corresponds to a flexion of 0 [°]. After that, the knee reaches almost 20 [°] during the loading response sub-phase. The extension of the knee continues again until the heel leaves the ground. At this point, the knee joint enters in flexion and reaches almost 60 [°] at the mid-swing and then comes in extension to restart a new gait cycle [14].

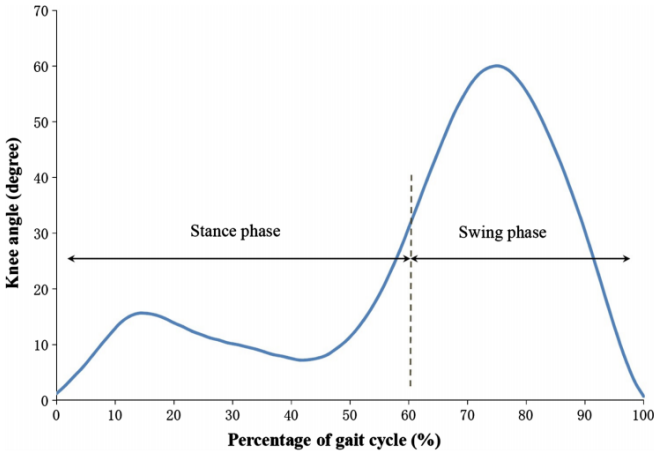

Figure 5 – Knee angle versus gait cycle [14]

By analyzing the knee flexion angle, some requirements concerning the knee joint stiffness can be deduced. It can be seen that the angle has significant variations as a function of the phases of the gait cycle. According to [16], to match the closer as possible the human like gait cycle, the knee joint stiffness needs three key features:

1. Compliant joint: during the stance phase, the knee joint angle has no big variations, and the knee joint behaviour acts as these of a spring with almost constant stiffness with only small hysteresis.
2. Stiff joint: at the beginning of the swing phase, when the toe leaves the ground, the knee joint has to be stiff for a quite small moment during which the energy provided by the ankle push off has to be efficiently transferred through the leading leg to readjust the body mass centre ahead.
3. Free joint: during the swing phase, the knee joint stiffness is also quite constant but with

a shallow slope. The stiffness of the knee joint must be the smallest possible.

2.4 Gait cycle data acquisition

To perform gait analysis, the usual method used is the Inverse Dynamics Problem in which the movements of the body are known, and the forces and torques responsible for the generation of the movements are computed. In practice, the Forward Dynamics Problem has much more computational cost and complexity, and is generally avoided [11].

As represented in Figure 6, different tools are used to record gait cycles. Firstly, markers are placed on the body subject. These are used to determine its kinematics. The 3D visual optical recording of the position of the markers is realised thanks to several cameras placed around the laboratory. The markers can be passive or active. In the case of passive markers, cameras can emit infrared light beams, and those are receipted back after reflexion on the spherical markers, while active markers can emit themselves light, as leds for example. An image registration in space is essential to express the recordings in the same reference axis. Secondly, ground reaction forces can be determined directly thanks to force plates embedded sensors placed on the ground. If the gait analysis needs to measure the muscular activity (electromyography) of the test subject, electrode sensors can be additionally put on the body skin to estimate the provided torques and forces [41].

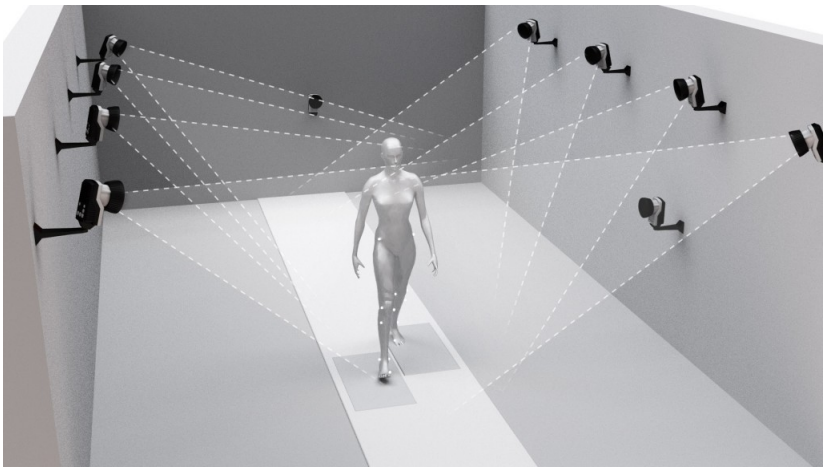

Figure 6 – Gait analysis laboratory [43]

3 State of the art of lower limb rehabilitation systems

3.1 Therapeutic rehabilitation

Before the introduction of robots in the rehabilitation and the assistance of walking applications, therapeutic rehabilitation sessions framed by specialists were generally planned to the recovery of the patient. The main advantage of this method is that the adapted care is provided to the patients according to their personal needs. However, many drawbacks can be pointed out. Firstly, there is often a lack of availability of rehabilitation sessions and a lack of efficiency due to their too low frequency. Indeed, during a traditional rehabilitation session, it is sometimes necessary to have at least the presence of three therapists at the same time to support and assist the disabled subject in its movement. Furthermore, these sessions generally have to be practised over an extended period which usually results in high expenses. The development of adapted tools or robots that the patients can use in daily living is a way to solve these disadvantages.

3.2 Active lower limb rehabilitation systems

The lower limb rehabilitation systems can be divided into several categories [2] as represented in Figure 7

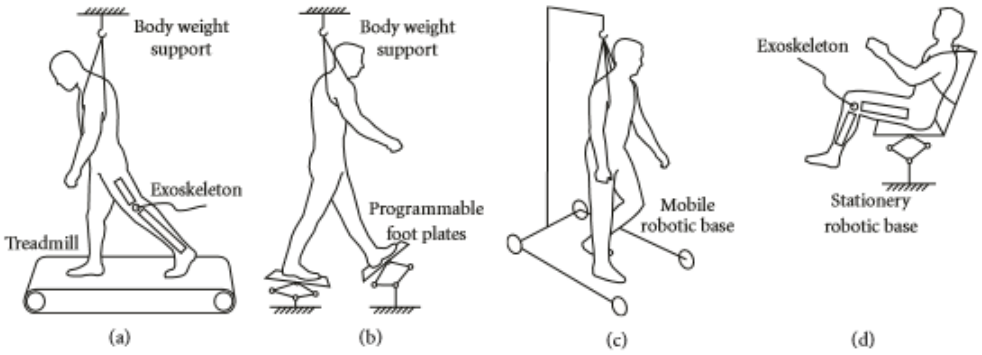

Figure 7 – Active lower limb rehabilitation systems: treadmill gait trainers (a), foot-plate-base gait trainers (b), over ground gait trainers (c), and stationary gait trainers (d) [2].

The challenge of the use of robots in this frame is that it has to provide to the patient the adapted care according to its needs. For example, in the case of a spasticity which causes the person to have a modification of the joints, a preprogramed trajectory of the movement could cause a severe additional wound. The unique morphology of every human being has to be taken into account.

3.2.1 Treadmill gait trainers

The first robots appeared within the framework of the rehabilitation, and the assistance of walking were supported on a treadmill. These systems received positive returns of the medical profession at the level of the reeducation. However, these are very greedy in energy and suffer from the fact that the patient is not able to move in the space for daily activities but only on a fixed point. Furthermore, driving speed of the treadmill is sometimes not adapted to the infirmity of the patient. For example, in the case in which this one suffers from a hemiparesis, whereby the time to make a step from a leg to the other one is not the same, the treadmill is hard to configure.

The *LOKOMAT* is represented as an example in Figure 8a. This system is the most experimented, and it consists of an active orthosis on a treadmill. The user is held on by the weight body support. The system enables a rehabilitation in a virtual environment. There are active

knee and hip joints and a synchronisation of the speeds of the orthoses and those of the treadmill. This system is one of the few treadmill gait trainers already commercialised. Other famous systems like the *LOPES*, *ARTHuR* or *ALEX* also enter in this category but are only at the clinical tests step.

3.2.2 Foot-plate-based gait trainers

The foot-plate-based gait trainers have the same characteristics as the treadmill gait trainers except that the walk is practised on over ground foot plates and no more on a treadmill itself. The foot plates can be adjusted to perform sequences regarding human-like gait cycles.

Nowadays, the *Gangtrainer GT I* is the only commercialised foot-plate-based gait trainer, but other prototypes are still clinically tested [2].

3.2.3 Over ground gait trainers

The mobile robots of rehabilitation over ground without foot plates have been developed later with the progress of the technologies and the better integration of the environment. The new features provided by this system is that the user can control its movement on his own, so that the exoskeleton legs can support the whole body weight and that the recovery is usually much faster and more efficient. It also offers a more sustainable solution. They can have several applications such as for daily application uses, for heavy works or even disaster applications.

The robot *BLEEX* has been developed by the American Defence and allows to supply more strength to the soldier, thanks to strong hydraulic actuators when this one is heavily charged. The robot can easily support up to 75 [kg] of load in the back.

Another currently commercialised robot is the *Robot Suit HAL-5* as represented in Figure 8c which is engineered to be used in everyday life from the size, the weight, the autonomy and the control. The control is hybrid so that the system can be adapted to people having still residual muscle functions (voluntary cybernetic control) or to people having no more muscle functions like those suffering from spinal cord injury (autonomous control). The voluntary cybernetic control is performed thanks to sensors placed on the skin which can detect the electrical activity within the muscles and used to determine the complementary power to realise the desired movement. The autonomous control consists of a pre-programmed sequence which can be activated by the user thanks to variations of mass centre measured by a 3D accelerometer placed in the lower back of the user.

(a) LOKOMAT (b) Gangtrainer GT I (c) HAL-5 (d) MotionMaker

Figure 8 – Lower-limb assistive robots

3.2.4 Stationary gait trainers

The stationary gait trainers are rehabilitation systems often used in muscular reinforcement, coordination improvement and training [2]. The most famous system is the *MotionMaker* as represented in Figure 8d. It is used for fitness training thanks to the simulation of the ground reaction torque during a gait cycle.

3.3 Knee-ankle-foot-orthosis and actuation

The main goal of an orthosis actuator is to be able to supply the required energy to recreate and support human movements. However, since there will be a direct human-robot interaction, the actuator must respect some biological conditions. As seen in Section 2.3, the knee joint has a varying stiffness along the gait cycle. The natural elasticity comes mainly from the tendons connecting the muscles to the bones. Many kinds of actuators have been developed, and it is still an active research topic in assistive robotics. Its number of joints usually defines the type of orthosis. The ankle-foot-orthosis, abbreviated as AFO, is used to resolve issues caused by drop-foot gait by guiding and limiting the plantar foot movements [23], [24], [7]. The knee-ankle-foot-orthosis, abbreviated as KAFO, additionally has a knee joint to support, assist and align the knee, ankle and foot [14]. The hip-knee-ankle-foot-orthosis system (HKAFO) can also be used to support all joints of the leg. The joints in the assistive exoskeleton can be passively or actively actuated, depending on the patient's troubles and objectives of rehabilitation [17].

The next part of this paper focuses on the knee-ankle-foot orthosis actuation systems. According to [14], there are three main types:

1. Passive KAFO: no external energy supply either no control for the knee joint.
2. Stance control KAFO (SCKAFO): locking system of the knee joint during the stance phase and releasing during the swing phase. This system has mostly passive knee joint.
3. Dynamic KAFO: a dynamic control law of the knee joint during the whole gait cycle. This has always an active joint.

3.3.1 Passive KAFOs

The first models of orthoses were passive. Indeed, they are the simplest and cheapest ones. These models are only able to support the body weight by an increase in the lower-limb strength thanks to the fixed knee joint during walking. A manually actionable locking system can be used for sit-and-stand motions [14]. Furthermore, no energy supply is provided, and the orthosis suffers from a lack of adaptability since it cannot be adapted to the most affected patients. Concerning the ergonomics, this kind of orthoses is quite uncomfortable for the patients and requires an extended training period to control the walking. The patient has to swing from one leg to the other one to vary the gravity centre spatially to reach stable conditions. This compensation of movements requires a bigger energy consumption from the user. For example, the *HAL* robots (Figure 8c) can have a passive ankle joint composed of simple restoring springs [23].

3.3.2 Stance control KAFOs

Compared to the passive KAFO devices, the SCKAFO allows a control of the knee motion during the stance phase thanks to the locking system. In this way, it allows to the patient to have a more natural gait and to diminish the global energy consumption. Many systems have been developed like the *Otto Bock Free Walk*, *Becker Orthopedic UTX* with a spring-loaded pawl lock, *Becker 9001 E-Knee Orthosis* with a magnetically activated clutch, hydraulic SCKAFO, quasi-passive compliant SCKAFO, etc. However, the reproduced gait cycle may have little differences caused by quick switches between the stance and swing phases or difficulties to go up and down stairs.

3.3.3 Active KAFOs

The evolution in the technological background allows developing active actuators for orthosis applications. Contrary to passive systems, active dynamic actuators can supply the energy by the addition of power providing or dissipating devices as well as control laws to provide the right amount of energy during each phase of the gait cycle. The active devices allow to generate the movements and increase the autonomy level of the patients. The need that must meet the actuator in such application is that it should be highly powerful, light and not too voluminous for its ease of transportation, human compatible and of low output mechanical impedance [22].

Direct Actuation

Many mechanical, electrical, pneumatic or either hydraulic active actuators have been developed since the last century. A non-exhaustive list of technologies will be presented in this document.

The first appearance of such orthosis found in the literature was in 1935. It consists of a purely mechanical system in which the patient had to load a torsional spring located to supply the knee joint. A cam-follower system guides the knee joint trajectory. In 1942 was developed the first orthosis with external energy supply coming from hydraulic valves located at the hip and knee joints. The valves were controlled thanks to a manual opening and closing when reaching the desired angles of joints.

More recently, several research laboratories are very active on this topic. *HAL* robot uses DC rotary motors, *ARTHuR* uses linear motors. *BLEEX* also has hydraulic actuators while *Power Assist Suit* is composed of pneumatic actuators. Other electroactive polymers and rubber-muscle actuators have also been developed [3].

Compliant actuation

To characterise as close as possible human-like motions, the direct actuation is generally not the most consistent. Indeed, accurate actuators are generally too stiff and have a too high output impedance [25], [16]. Nowadays, the interaction between robots and human is highly developing in medical as well in industrial field. The robot has to ensure safety to the user. In general robotics application, the simplest safety precaution is to restrict access to the workspace area of the robot. However, for human-robot applications, the robot is configured to avoid to cause severe damages to a human in case of unexpected collisions or others. The solution usually cited is the use of compliant joint actuators. These provide more safety but generally suffer from a lack of position and speed accuracy [26]. The compliant actuator allows isolating the motor non-linearity and rotor inertia from the knee joint in the case of orthosis applications. The compliant part can be introduced in the actuator by in series (SEA) or parallel (PEA) by springs, dampers, hydraulic system [27], magnetorheological fluids, etc. In most current cases, the SEA with springs is implemented in orthosis systems.

The elastic component is placed between the load and the gearbox of the electrical motor and can also be used for torque measurement [28]. The elastic component can also play the role of shock absorbers for none desired manipulations [15]. Elasticity can be provided by different ways in the actuation system. A helical torsion spring can be introduced between the gear of a DC motor and the human joint directly. In this configuration, the spring is able to support high torques, and it decreases its sensitivity [42]. An improvement of it could be to place the spring between the worm gear and the output [36] or other customised elastic elements, *MACCEPA* [37], [15]. It can also have variable stiffness actuation [38].

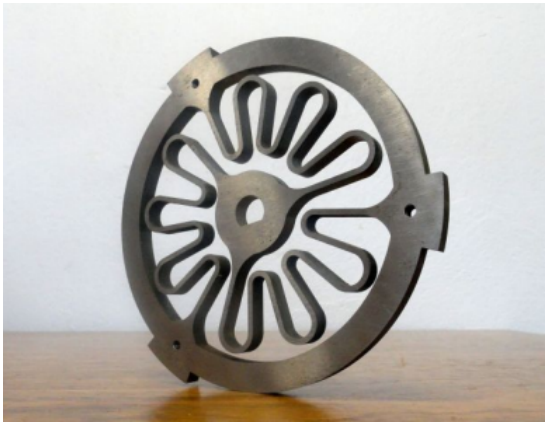

Figure 9 – Customised spring [15]

The control law mainly provides the robustness of these systems [5]. Different strategies of control law can be performed. In most of the cases, the SEA is controlled by an impedance control [14]. The springs providing the compliance are limiting the position accuracy but can have a robust speed or torque control [39]. However, a well-tuned control strategy is required since the compliance of those actuators induce new errors, dynamic effects, longer response time, settling time and overshoot in the transmission system.

Concerning magnetorheological actuators, the compliance is provided by a magnetorheological fluid usually located between the load and the motor as it is the case of usual springs. A magnetic field strongly influences a magnetorheological fluid. Its inherent viscosity can strongly vary, allowing to lock the system when this last one is high. It can decouple the motor from the load when this last one is too low, acting as a clutch or a variable stiffness controlled system. This kind of compliant actuator is a safe technology already used in orthosis application [34]. There also exists electrorheological fluids that are sensitive to an electric field, but these are rare due to the high energy consumption that they require.

3.4 Test bench for orthosis knee joints

To test the performances of an orthosis prototype, two methods can be performed. In most of the cases, the orthosis is evaluated directly on test subjects to determine the efficiency of the device, its reliability and capacity to reproduce the gait cycle. The ergonomics of the device for the patient or other clinical efficiency tests can also be determined by comparing the rehabilitation improvements of the patients with the orthosis and without using it [13].

On the other hand, some prototypes are sometimes also evaluated on a test bench. Indeed, some mechanical parameters are not reachable by a simple test on subjects since the device is not always working at its nominal capabilities. This method allows, for example, the evaluation of the maximum torque that the motor can exercise, the fatigue of the system, the friction, latency time, etc [13]. This method is usually more time-consuming because of the time taken to build the test bench or the calibration of all the needed sensors and may be more expensive. After that, non-exhaustive examples of test bench adapted to orthosis actuators will be further developed in this thesis.

Related to [33], a quasi-passive compliant stance control knee–ankle–foot orthosis (SCKAFO) is developed. Contrary to the usual locking system, during the stance phase the orthosis tends to control the natural shock absorption function of the knee. A spring is placed in parallel to the knee joint for the stance phase of the gait cycle while the joint is free to rotate for the swing

phase. The test bench built to evaluate its performances is represented in Figure 10a. It is composed of a four-bar linkage mechanism which is operated thanks to a servo motor to assess the performances of the knee joint. According to [20], which consists in an active knee-ankle orthosis, series elastic actuator is composed of DC motors and a torsional spring in series for paediatric patients. As represented in Figure 10b, the corresponding test bench of tracking evaluation is composed of a linear motor which is applying torque to the knee-ankle orthosis. A load cell, a framework to attach the module of the knee and ankle joint are used. The assembly forms a crank slider-like mechanism.

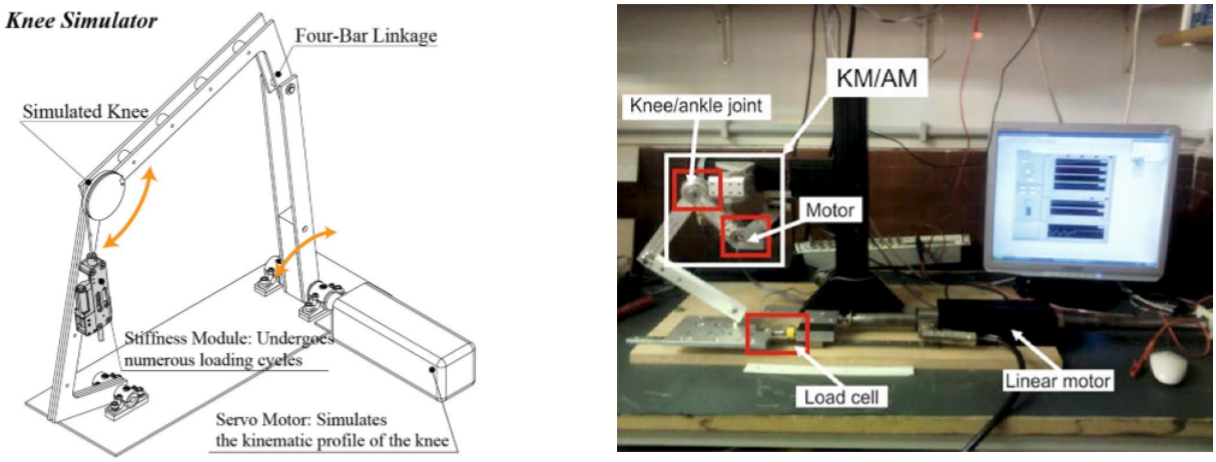

(a) Knee joint test bench for the compliance control module evaluation and the spring latency [33]

(b) Knee-ankle joint tracking evaluation test bench thanks to a linear actuator [20]

Figure 10 – Test benches

In [7] is developed a mechanical-rotary impedance actuator (the *MeRIA*) which can induce a variable stiffness and joint motion at the same time. The associated test bench is represented in Figure 11. It consists in a framework where the actuator is coupled to a torque sensor that measures the resulting torque on the axis when a lever arm applies a load on the other extremity. A magnetic encoder is recording the angular position of the shaft.

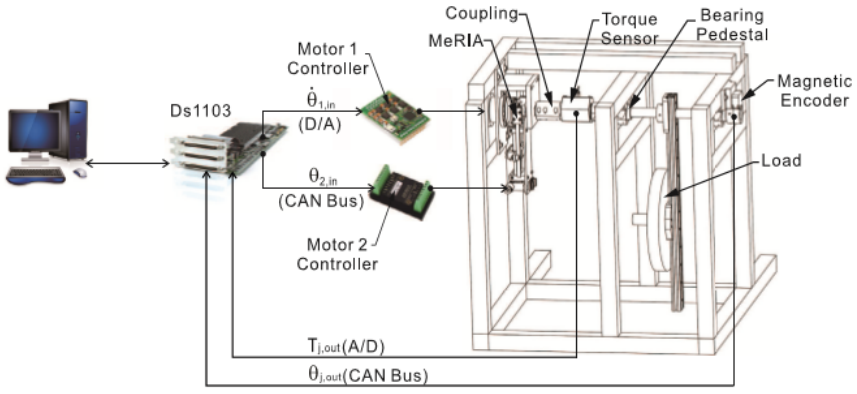

Figure 11 – Test bench for the *MeRIA* actuator [7]

In Figure 12 is represented the test bench of the *ARES* prototype. It is composed of two rotating segments around the knee joint. An extension spring connected to the shank induces variable torque at the joint. The actuator consists of a main motor providing the rotation and a second motor that emulates stiffness variations linearly. To test the reliability of the prototype, the tracking of the command that the main motor has to follow, while the load is measured thanks to a rotary magnetic encoder [16].

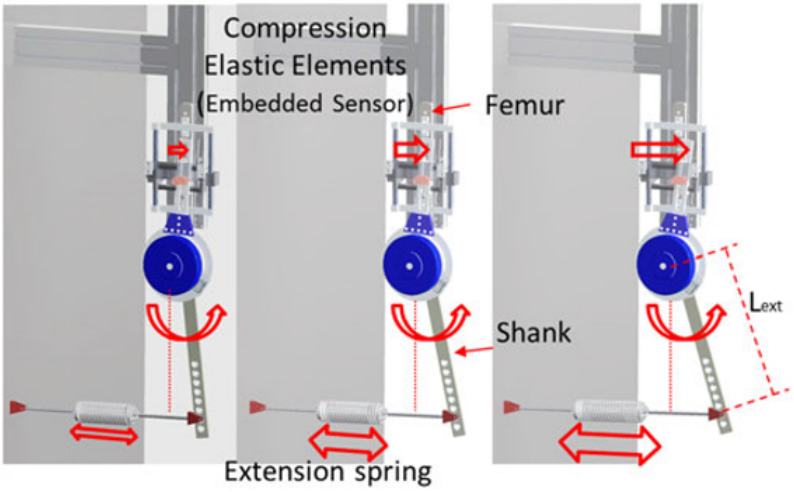

Figure 12 – Test bench for the *ARES* orthoses [16]

According to [13], the modelled test bench of the series elastic actuation system is performed thanks to another kind of pendulum which is tuned to have a human-leg behaviour. The pendulum can rotate around the knee joint. The shank and foot inertia are represented thanks to two weights. An external wrench can be applied to the foot part, representing the gravitational torque and inertial resistance of the pendulum [12], and can be measured thanks to a load cell. The test bench is represented in Figure 13.

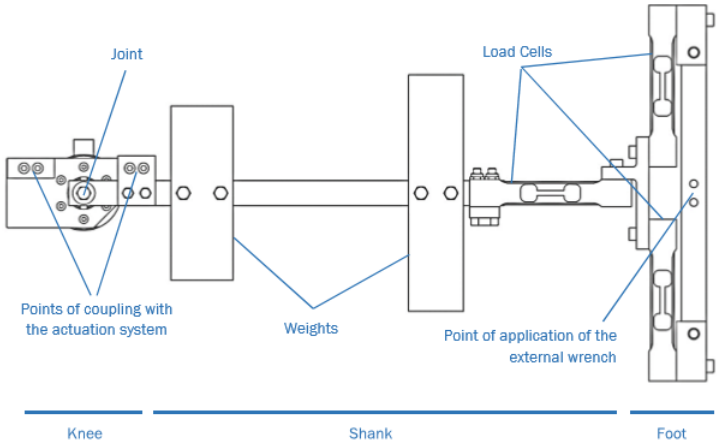

Figure 13 – Leg test bench according to [12]

4 Test bench and sensor calibration

The current test bench of the laboratory is represented in Figure 14.

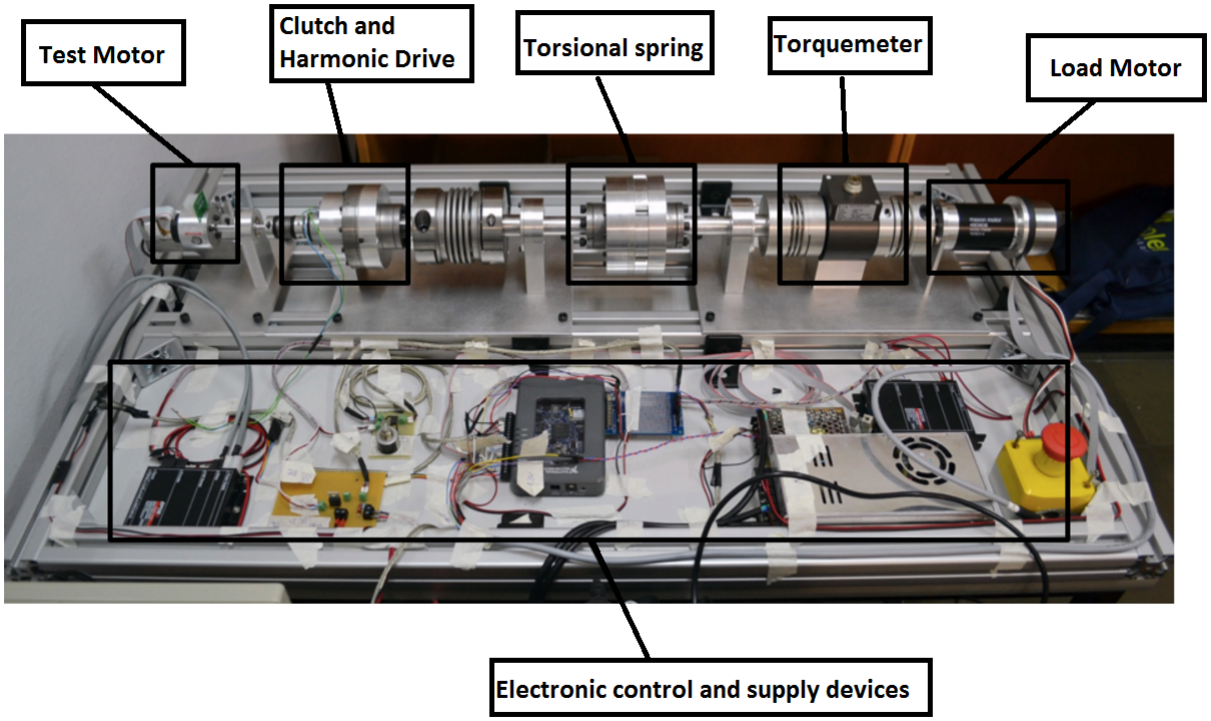

Figure 14 – SEA Testbench

Basically, it consists of an axis composed of a compliant actuation system to which a load disturbance can be applied. The load disturbance is provided by a load motor which is in dual configuration towards the compliant actuation system. The test motor drives the actuation system, and the compliance is obtained by adding a torsional spring connecting element in series between the actuation and the load.

Thanks to the test bench, it becomes possible to experimentally tests the series elastic actuator in the case of human gait cycle applications. The main aim is to evaluate the performances and tracking capabilities of the series elastic actuator while applying a load disturbance.

The simulation of the virtual behaviour of the knee joint is done by imposing the test motor to track the reference gait position or velocity of a healthy subject. On the other hand, the ground reaction torque knee is simulated thanks to the load motor. The test bench is controlled thanks to the main microcontroller (*National Instruments, MyRIO*). The microcontroller commands the drivers of each motor to provide them with the right amount of energy. The microcontroller also allows the collection and writing of instantaneous information coming from the different sensors needed to control the test bench correctly. The assembled configuration and control of the test bench is presented in more details in the next subsections.

4.1 Assembly

Test motor

The mechanical power of the series elastic actuation is provided by a brushless DC electric motor *EC45 flat* which can supply up to 70 [W]. A DC brushless motor is generally composed of

a rotor and a fixed stator. Magnetic induction is created through the excitation windings when these are electrically supplied. This magnetic induction is then perceived by the rotor surrounded by a closed spire. The current inversion in the coil of the rotor is done electronically instead of using brushes, thanks to Hall sensors measuring the instantaneous position of the rotor. The brushless DC motor is more precise than the usual DC motor due to the elimination of the friction induced by the brushes. Furthermore, it can produce a high torque and work at high velocity.

The test motor generating the typical knee trajectory of the human gait cycle is mounted with a cantilever configuration. The test motor is powered thanks to a driver (*Maxon, EPOS 24/5*). The energy is provided by an external 24 [V] power supply. A current board sensor (*Allegro, ACS712ELC-20A-T*) is used to measure the electrical consumption of the motor and is placed in series with the power supply. A voltage divider is used to reduce the 24 [V] power supply to 3.3 [V] to make the signal readable by the microcontroller. The test motor is connected thanks to a coupling (*ETH, MK2 20*) to the harmonic drive. The speed and position of the motors are measured thanks to an encoder *MR TYPE L (Maxon Motor AG, Sachseln, Switzerland)* which allows discrete relative measurements.

Load cell

A load cell is connected to the test motor to measure its corresponding reaction torque. The used load cell is *Utilcell, M104,1.2kg*. The load cell allows to convert a measured force thanks to the deformation of strain gauges into an electrical readable signal. The signal is then amplified to be read by the microcontroller. A strain gauge consists of a conductive wire or film which often takes the configuration as represented in Figure 15. The application of an external force on the gauge induce strains. The electrical resistance of the gauge is in this way varying with the geometry and resistivity variations. The load cell is also supplied by another 13 [V] power supply (*TDK-Lambda, LS25-15*).

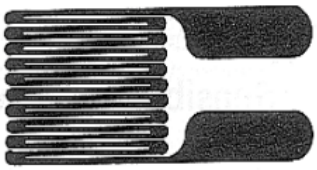

Figure 15 – Strain gauge

The gauges are attached to the load cell for which they measure the strain. Therefore the gauges and the load cell have to be mechanically compatible. The stiffness of the load cell and the gauges have to be similar so that the strains on the gauges are matching with those of the load cell.

Electromagnetic clutch

The electromagnetic clutch (*KEB, Combinorm 02.02.120*) is an electromechanical device used to engage or disengage the mechanical transmission between the test motor and the rest of the shaft of the test bench. A typical electromagnetic clutch is represented in Figure 16. The role of the clutch during the gait cycle is to lock the knee joint of the orthosis during the stance phase and reduce the global power consumption of the system. The test motor is engaged back during the swing phase of the gait cycle when the angle variation is important.

The clutch is supplied by the microcontroller passing through a *MOSFET (RFP50N06)*, al-

lowing to increase to signal voltage from 5 [V] to 24 [V].

The working principle of the clutch is based on friction. The electromagnetic clutch is composed of a coil, a rotor and a hub [45]. When a DC power source supplies electrically the coil, current is passing through the coil, and the magnetic field is created. The armature of the clutch will then be attracted thanks to the magnetisation of the rotor. The contact force between the surfaces is resulting in friction force which allows the engagement of the clutch. When the electrical power supply is removed, the clutch is disengaged, and the shaft is free to move without additional drag. Indeed, there is a restoring position of the armature and a creation of an air gap between the armature and the rotor. Contrary to mechanical clutches for which the generated friction pressure is produced thanks to springs, the magnitude of the friction will depend on the scale of the generated magnetic field.

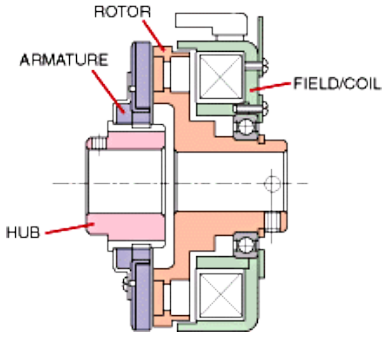

Figure 16 – Representation of an electromagnetic clutch [46]

Harmonic gear box

The gear box of the test motor is a harmonic drive (*KEB, SHD size 20, Ratio 160*). A typical harmonic drive is represented in Figure 17a.

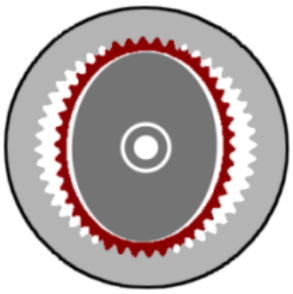

(a) Harmonic drive [47]

(b) Planetary gear

Figure 17 – Gear boxes implemented on the test bench

The harmonic drive helps to increase the torque of the orthosis motor to the magnitudes which will be reached in pratice. The main advantages of the harmonic drive compared to another type of gears are that it can allow a high reduction of speed, has a low backlash and that the input and output shafts are on the same axis. This is beneficial against misalignment. On the test bench, a high-speed reduction is also needed because the DC motor is not able to be very precise at low speed. On the test bench, the reduction rate is 160:1 (i_{HD}). Basically, a harmonic drive

is composed of an external rigid spline wheel with internal gearing, an internal flexible spline wheel with external gearing connected to the output axis and an elliptical element generating the deformation of the internal flexible hollow wheel. The elliptical element is deforming the flexible hollow wheel. Because this one generally has one or two gears less, it is rotating relatively to the external hollow wheel. The resulting efficiency of the harmonic drive used on the test bench is up to 0.65-0.7, depending on the velocity. The system is very rigid and allows a high precision. However, the global behaviour is not linear due to the flexibility of its components and high friction. In practice, there may be a small dependence of position. The gear box is connected to the torsional spring thanks to a coupling (*EHT, BKL 150*).

Torsional spring

The torsional spring provides compliance to the actuator. The torsional spring axis is connected to the torquemeter of the load motor thanks to a coupling (*ETH, BKE 60*). Its CAD representation is given in Figure 18.

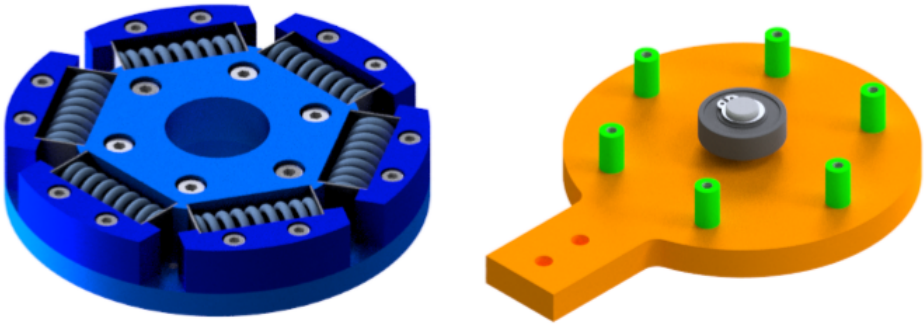

Figure 18 – Torsional spring representation. The torsional springs are represented on the left and are part of the actuation system [12].

It is composed of six compressive springs on a disk. The disk is connected to the axis thanks to cylindrical elements. Plastic components are used between the springs and the cylindrical elements to act as pre-compression elements to avoid significant mechanical stresses when rotational direction changes occur.

Torquemeter

A torquemeter is useful to measure the load torque resulting from the reaction of the ground. The selected one on this test bench is a rotary torque transducer (*ETH, DRBK-100*). It cannot support load over 100 [Nm]. The torquemeter is then connected to the load motor thanks to another coupling (*ETH, BKE 60*).

Like the load cell, the torquemeter is composed of four strain gauges for which the electrical resistance variations give a measurement of the torque.

Planetary gear box

Another gear box is located between the load motor and the rest of the shaft. It is the model *Maxon, GP 52 C, i=66*. It is a planetary gear box as represented in Figure 17b. As the harmonic drive, it also allows a coaxial movement of the input and output shaft, a high reduction ratio of 66:1 (i_{RED}) and a high efficiency. The gear with fixed axis are called *planets* while the other turning with their axis are called *satellites*.

Load motor

The reaction torque of the ground on the knee is generated by the load motor. The selected motor is a brushless DC motor (*Maxon, EC60, flat, 48V)*. The energy is provided to the motor thanks to another driver (*Maxon, ESCON 50/5*), supplied itself by another 48 [V] power supply. Again, an encoder (*MR TYPE L (Maxon Motor AG, Sachseln, Switzerland)*) is used to measure the position of the motor.

4.2 Control

The control of the test bench is realised with the software *LabView* and executed on the *MyRio* controller. To assure the execution in real time and due to high computation cost of all elements, the realised structure is network based. This means that the human-machine interface (inputs, commands and visualisation) is runned on a com, while the sensor signals and control are executed on the *MyRio*. Data is exchanged via a USB connection.

The general signal generation for the control of the test bench is shown in Figure 19. The command is introduced by the user thanks to the user interface. The user can enter the desired trajectory that the motor has to track. The motors can be commanded either in torque, velocity or position. The trajectory can be defined by its kind, amplitude and frequency. This command is an input of the *MyRio* microcontroller. Another input of the microcontroller is the type of control that is desired to track the reference signal. The associated parameters are also introduced by the user and usually have to be experimentally tuned by trial and error testing. Indeed, in practice, the signals are strongly dependent on perturbation effects. The measured signals of the sensors are also necessary data for the controller. It reads the encoder signal for both motors, the electrical power from the current sensor and voltage divider, and the signals coming from the load cell and torquemeter.

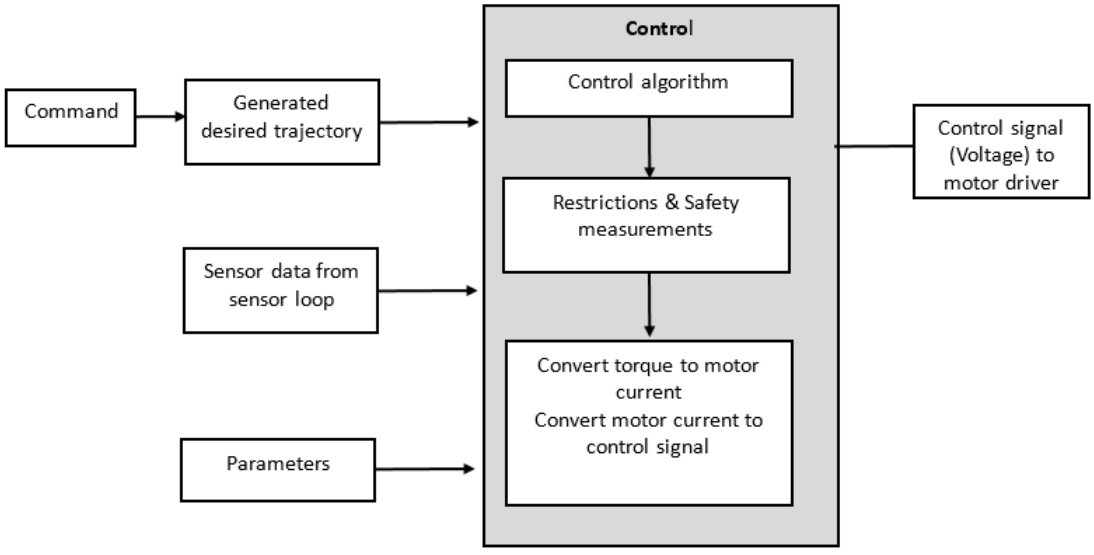

Figure 19 – Control signal generation on the test bench

Concerning the controller on itself, it commands the tracking of the reference trajectories. For safety purpose, some restrictions and precautions are implemented. Indeed, when one restriction is met, the execution of system will automatically stop to avoid any embarrassing incident as breaking of the materials. The restriction cases implemented are:

— A maximum deflection difference of the axis about 5 [°] avoiding a permanent deformation of the torsional spring.

— Torque limitations for both motors outside the range [-20; 20] [Nm].
— Absorbed input power in the driver when the motor is braking. The driver will immediately stop working to avoid its overheating and burning.
— Synchronisation trouble between all the components.

However, an emergency stop button is also added to the system, and it is highly recommended for the user to activate it if anything is happening differently as it is expected.

When the system is respecting the safety restriction, the converted control signal is sent to the driver which will supply the motor with the right amount of power.

The real time measurements and conditions are viewable on the user interface of the computer of the lab as represented in Figure 20. The user can see and compare the instantaneous actual and desired reference trajectories, the related torques at both motors, the output control voltage sent to the motor drivers and the activation state of the active clutch.

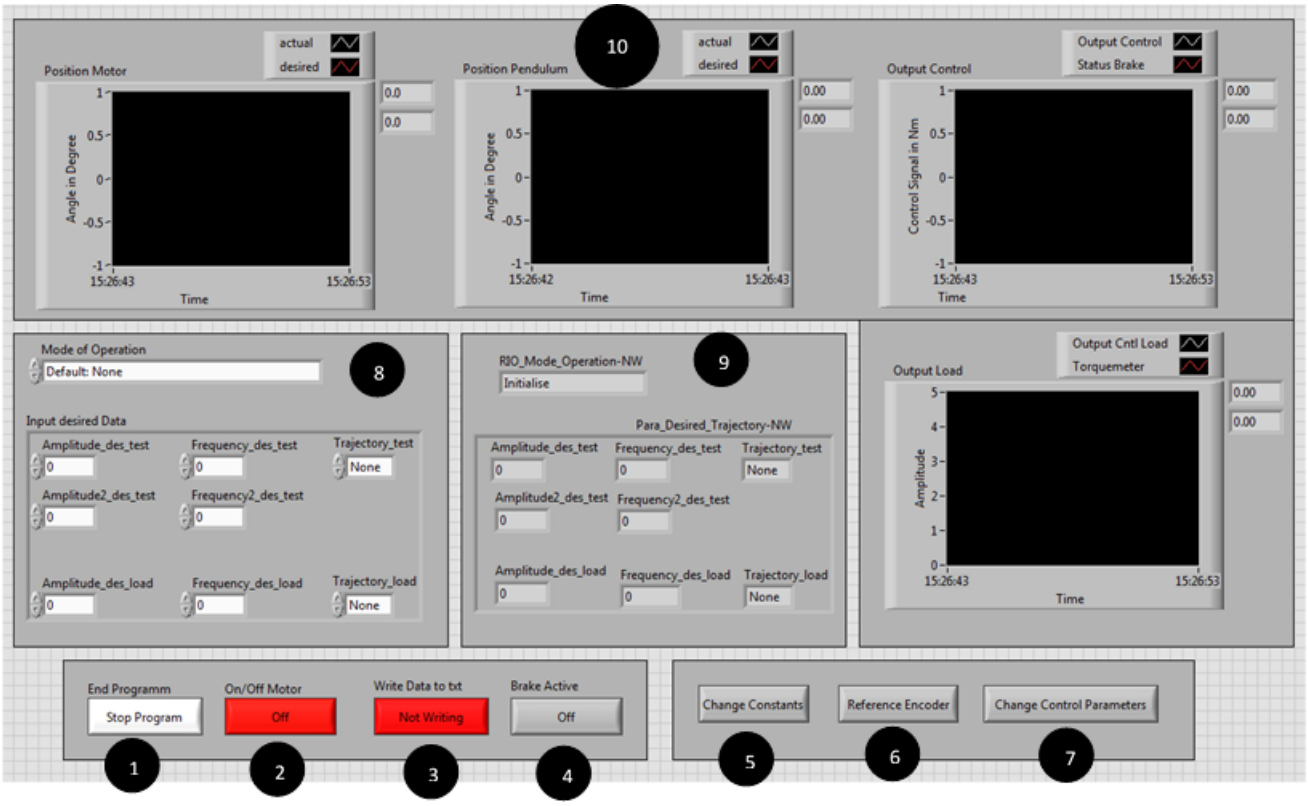

Figure 20 – User's interface of the test bench

4.3 Calibration of the sensors

A calibration of the different sensors is needed to ensure the reliability of the measurements. Even if the characteristic curves are most of the time given by the manufacturers of the sensors, some friction or conditions of application may make the characteristics curves differ in practice compared to the theoretical ones.

The sensors to calibrate are the torquemeter which measures the torque of the load part, the load cell which measures the torque of the actuation element and the voltage sensor which is used to measure the conversion of the output voltage of the power supply to the one needed for the microcontroller supply. The sensors are evaluated in their useful ranges of application.

Note that the encoders used at the motors level to measure their relative positions do not need to be calibrated since they consist of digital sensors. The other sensors are analogical.

The general iterative procedure used to calibrate the sensors is:

1. Application of a known physical quantity as torque or voltage, depending on the sensor measurements.
2. Measurement of the voltage output of the sensor corresponding to the physical quantity.
3. Correlation between the voltage output of the sensor and the known physical quantity.

4.3.1 Torquemeter calibration

The first calibrated sensor is the torquemeter which allows to measure the difference between the torque imposed by the microcontroller as an input of the load motor and the measured one by the torquemeter

To calibrate it, a known external torque has to be applied to the axis of the motor. The easiest way is applying various constant torques on the axis thanks to a steel calibration pendulum. To fix the pendulum on the load part axis, the elastic part is removed. The lever arm of the pendulum is a simple steel bar mounted to the axis thanks to a conical coupling at the opposite extremity of the load motor. This method allows to change the applied torque by changing the motor shaft angle.

The torque applied by the calibration pendulum on the axis and supposed to be measured by the torquemeter is given by

$$T = mgL_g \sin(\theta) \tag{1}$$

where $m = 1.94$ [kg] is the mass of the lever arm, $g = 9.81$ [m/s^2] is the gravity acceleration, $L_g = 0.25$ [m] is the distance between the axis and the mass centre of the pendulum and θ is the angle of the pendulum with respect to the vertical.

A *LabView* implementation of the procedure is used. It imposes to the load motor a slow triangular torque signal. The pendulum reaches the different imposed rotation angles thanks to the torque-angle relationship given by Equation 1 and stays static a few seconds due to static friction in the system. The corresponding torques are measured by the torquemeter and recorded by the microcontroller on an external memory.

In practice, the torquemeter is more powerful than the maximum torque that the lever arm of the pendulum can induce on the axis. The maximum working range of the torquemeter is therefore not evaluated and a limitation of the angle range has to be determined. The measurements have been done by angle increments of 2 [°] over the range [-90; 90] [°].

As represented in Figure 21, the static gains are evaluated by a correlation between the measured torques and positions. Due to the pendulum behaviour, it is first supposed that the static gain curve has a sinusoidal behaviour and that a nonlinear regression is used to approximate it and compensate the absolute angle position error. The gain output voltage curve is supposed to be

$$V = a + b \sin(\theta_{enc} + c) \tag{2}$$

Assuming that the rotation angle of the torquemeter is compensated by the measurements of the relative encoder and related to

$$\theta_{enc} + c = \theta \tag{3}$$

The torque voltage relationship is then evaluated by

$$T = \frac{mgL_g}{b}V - \frac{mgL_g}{b}a \tag{4}$$

with the computed parameters as presented in Table 1.

a [V]	b [V]	c [rad]
0.245	-0.008	-0.01

Table 1 – Torquemeter calibration parameters

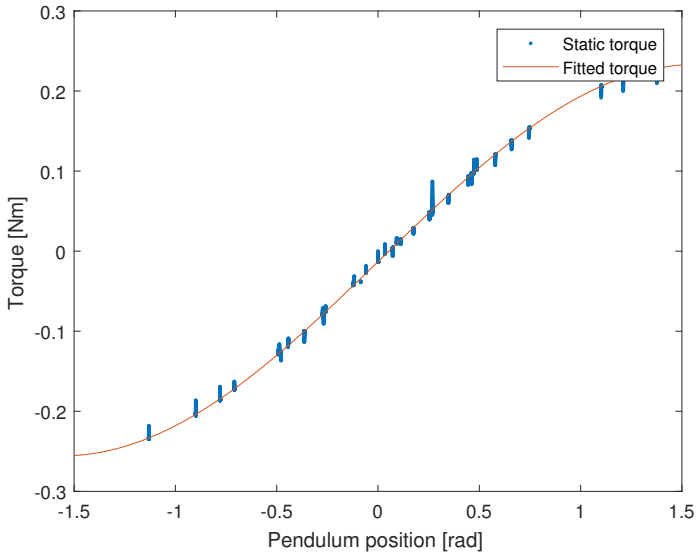

Figure 21 – Torque-pendulum angle gain curve for the torquemeter

4.3.2 Load cell calibration

The general idea of the calibration procedure for the load cell associated with the measure of the torque at the test motor is the same than the one for the torquemeter of the load motor.

Concerning the pendulum, the elastic coupling connecting the motor shaft to the harmonic drive is not able to maintain the pendulum. Therefore a support system has to be introduced for the measurements, as represented in Figure 22a. Its shaft is connected to the motor axis. The pendulum was manufactured in aluminium.

However, the test motor is not capable of generating enough continuous torque to lift the pendulum on the full measuring range. Furthermore, the load cell maximum allowed torque is lower than the maximum pendulum torque that the lever arm of the pendulum can produce. This means that forcing a motor position which puts more torque on the load cell than the maximum allowed will deform the load cell permanently. In practice, it is not recommended to have a rotation angle over 50 [°].

In order to apply the desired torque to the load cell a 3D printed brace is used to fix the motor stator to the pendulum axis (which is fixed to the motor rotor) effectively bypassing the motor (Figure 22b) while still being able to use the encoder motor to visualise and measure changes in the pendulum's position.

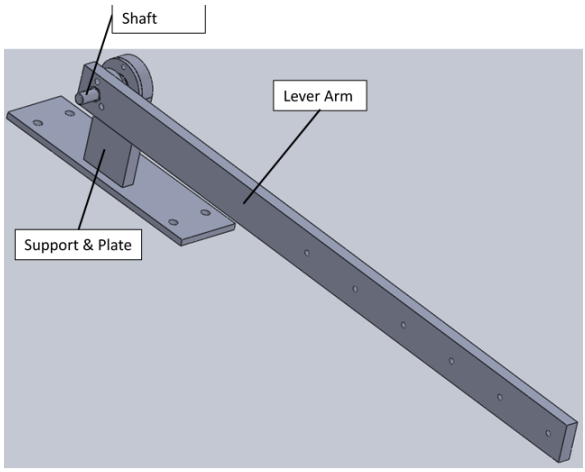

(a) Calibration pendulum for the load cell and its support

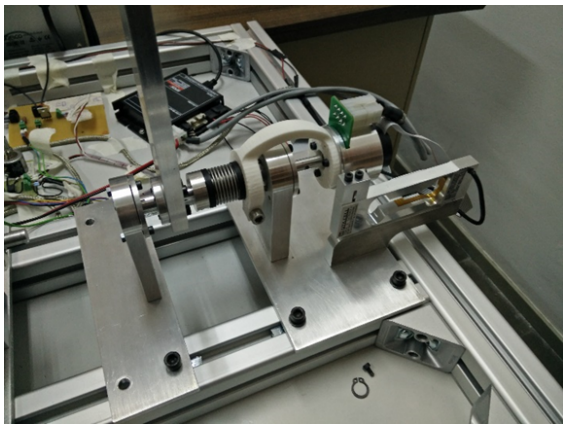

(b) Bypassing of the motor and pendulum fixation

Figure 22 – Load cell calibration

The following calibration steps focus on obtaining the data for the gain curve of the load cell. However, this has to be done by hand and not through the *LabView* software since the motor is bypassed. Different random angles of rotation of the pendulum are tested thanks to untightening and tightening the main screw on the brace.

The voltage from the load cell is recorded to find the gain curve of the sensor with the same method than to the one used for the torquemeter. The curve is presented in Figure 23. In practice, the potentiometer of the operational amplifier system for the load cell is adjusted to read 2.5 [V] at 25 [°] of the pendulum's rotation.

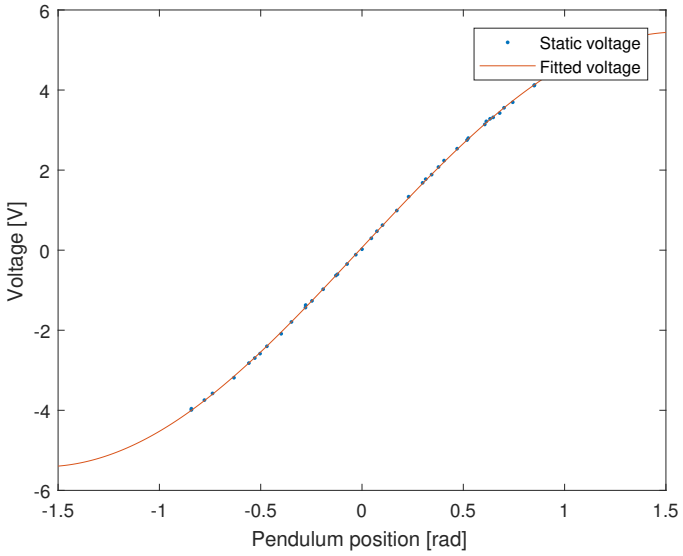

Figure 23 – Voltage - pendulum angle curve for the load cell

According to Equation 2, the parameters are computed as represented in Table 2.

a [V]	b [V]	c [rad]
5.43	0.001	0.019

Table 2 – Load cell calibration parameters

4.3.3 Voltage sensor calibration

The voltage sensor consists in a voltage divider with two resistances of theoretical values of 15.3 [Ω] and 2.4 [Ω]. These are useful to lower the output voltage coming from the generator supply (≈ 24 [V]) to transform as input of the microcontroller (3.3 [V]). The sensor measures how the power supply voltage is converted to the voltage measured at the microcontroller input.

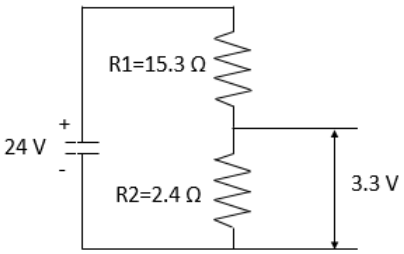

Figure 24 – Voltage divider

To perform such measurements, different input voltages at the power supply are generated. The tested voltage measured as well as the microcontroller voltage are compared. Note that the power supply voltage has to be measured thanks to a multimeter instead of taking the one displayed on the power supply device since this is not reliable and accurate. The voltage divider is represented in Figure 24.

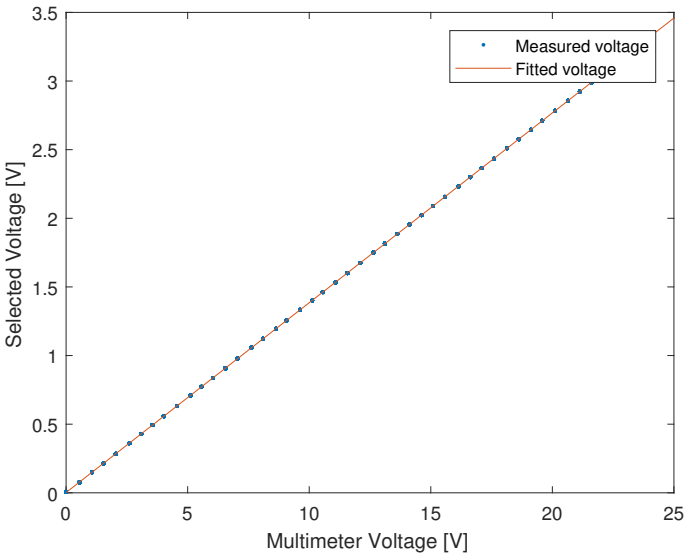

Figure 25 – Voltage-voltage gain curve of the voltage sensor

The theoretical voltage transformation according to the voltage divider is given by

$$V_{microcontroller} = \frac{V_{power} R_2}{R_1 + R_2} \tag{5}$$

The gain curve is supposed to be linear with a small offset as

$$V_{microcontroller} = a + bV_{power} \tag{6}$$

which gives the parameters represented in Table 3.

a [V]	b [-]
0.002	0.139

Table 3 – Voltage sensor calibration parameters

The calibration curve of the voltage sensor is represented in Figure 25.

4.3.4 Current sensor verification

The current sensor is used to measure the current supply of the motors and the electromagnetic clutch. In this case, no calibration is done but only a verification of the correctness of the values of current. The current sensor is composed of an evaluation board *(Allegro MicroSystems, ASEK712ELC-20A-T-DK)*, which already provides a board on which connectors are available. The board is designed up to 20 [A]. This is overdesigned for the *EC45 flat* motor which can give up to 70 [W]. However, the biggest measurement is up to 5 [A], which may be exceeded when the motor starts rotating.

Because the current consumption of the motor driver is also accessible, the current sensor has just been verified to give the same results. Regardless, no changes can be done on the board after calibration, and it is supposed to read the actual current.

5 Dynamic analysis

5.1 Direct actuator

From a functional point of view, the actuator can be summarised as represented in Figure 26. The positive direction of rotation around its principal axis of inertia is also represented as a reference.

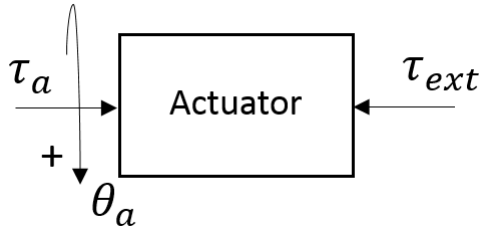

Figure 26 – Directly actuated system schema

In the case of rotational systems, the equation of motion from the angular momentum theorem can be written as

$$\boldsymbol{I}_a\boldsymbol{\alpha} = \sum \boldsymbol{\tau} \tag{7}$$

where $\boldsymbol{I}_a$ is the moment of inertia of the rotating body according to its main axis of inertia, $\boldsymbol{\alpha}$ is the angular acceleration vector and $\sum \boldsymbol{\tau}$ is the sum of all torques acting on the body towards the angular acceleration. In the case of direct actuation and only one degree of freedom in rotation, Equation 7 can be transformed as

$$I_a\ddot{\theta_a} = \tau_a - \tau_{ext} \tag{8}$$

The actuator of inertia I_a is able to generate a torque τ_a which is perturbed by the load torque τ_{ext} representing the external torques disturbances, inertial torques and gravitational torques of the orthosis. $\ddot{\theta_a}$ represents the angular acceleration of the actuator. The mechanical power P_a that needs to be provided the direct actuator is defined as

$$P_a = \tau_a\dot{\theta_a} \tag{9}$$

Eventually, gathering Equations 8 and 9 together yields

$$P_a = (I_a\ddot{\theta_a} + \tau_{ext})\dot{\theta_a} \tag{10}$$

With this kind of actuation system, it can be concluded that the mechanical power is increasing with increasing moment of inertia, external applied torque and increasing velocity.

5.2 Series elastic actuator

Similarly to the introduction of the directly actuated system in Section 5, the series elastic actuator can be modelled as represented in Figure 27. In this configuration, a spring is located after the actuator. The spring is considered as mass less. The spring can store and release potential energy when compressed or relaxed and generally contribute to a global decrease in energy consumption besides its human-like stiffness behaviour and robustness. The stiffness is a physical quantity defined as the capacity of a body to deform under applied external torque in the rotational case. The more rigid the material, the bigger the stiffness k, as

$$k = \frac{\tau}{\theta}[\text{Nm/rad}] \tag{11}$$

where τ [Nm] is the applied external torque on the body and θ [rad] is the angular deflection of the material.

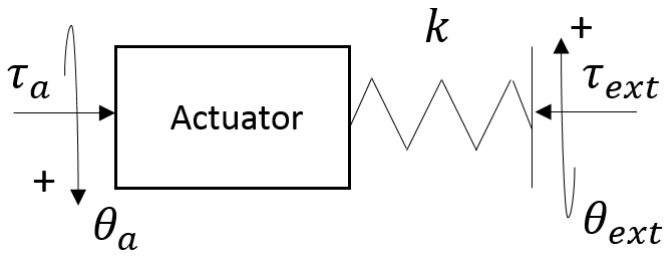

Figure 27 – Series elastic actuator representation

The additional contribution of the spring allows the equation of motion to become,

$$\begin{cases} I_a\ddot{\theta}_a + k(\Delta\theta) = \tau_a \\ k(\Delta\theta) = \tau_{ext} \end{cases} \tag{12}$$

where k denotes the stiffness of the spring and $\Delta\theta = \theta_a - \theta_{ext}$ denotes its deflection. The external torque is responsible for spring deformation. The power that the actuator is supposed to be able to supply is in this way given by

$$P_a = (I_a\ddot{\theta}_a + k\Delta\theta)\dot{\theta}_a \tag{13}$$

while the potential energy stored in the system is

$$E_{pot} = \frac{1}{2}k(\theta_a - \theta_{ext})^2 \tag{14}$$

5.3 Clutchable series elastic actuator

In the case of orthosis application, the use of a clutch may be useful to lock the knee joint during the stance phase of the gait cycle and can offer a free rotation of the joint during the swing phase.

In the test bench, the clutch is added in series on the shaft and takes place between the test motor and the harmonic drive as represented in Figure 28.

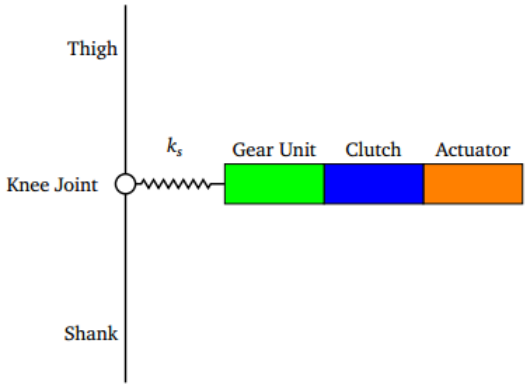

Figure 28 – Clutchable series elastic actuator schema [12]

The same equation as in Section 5.2 is used, except that the actuation is passive during the stance phase of the gait cycle. This means that only the electrical power supplying the electromagnetic clutch is used to lock the system and no mechanical power is spent. In this case, the power balance equation is transformed as

$$\begin{cases} P_a = (I_a\ddot{\theta}_a + k\Delta\theta)\dot{\theta}_a & \text{if clutch is activated} \\ P_a = 0 & \text{otherwise} \end{cases} \tag{15}$$

5.4 DC motor equations

Usually, the motors manufacturers give the datasheet of the motors with every physical, electrical and mechanical useful parameters used to construct the model of the motorised application. A review of the useful parameters of the test and load motor is available in Table 4.

	Test motor	Load motor
Mechanical data		
Moment of inertia of the rotor I [kg m^2]	$1.81\,10^{-4}$	$1.21\,10^{-4}$
Viscous damping c [Nms]	$1.31\,10^{-5}$	$5.647\,10^{-7}$
Torque constant K_m [Nm/A]	0.037	0.114
Electrical data		
Resistance R [Ω]	0.608	1.1
Inductance L [H]	$4.63\,10^{-4}$	$8.64\,10^{-4}$
Electromotive force constant K_e [V/rad/s]	0.037	0.145

Table 4 – Test motor data parameters

The DC motor system on its own can be mathematically separated between its mechanical and electrical parts. The global system of a DC motor can be summarised as represented in Figure 29.

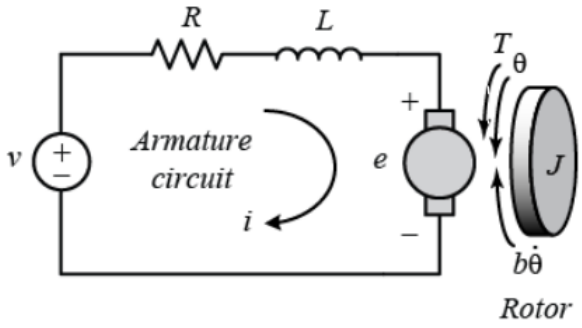

Figure 29 – Electromechanical representation of a DC motor [48]. Note that the inertia is in the future of this work expressed as I and the damping as c.

5.4.1 Mechanical equations

The mechanical part composing the DC motor is the motor's shaft inertia I, the torque exercising of the shaft T and the viscous damping c. Mathematically, the general equation of motion can be expressed as a differential equation of the angular shaft position

$$I\,\frac{d^2\theta(t)}{dt} + c\,\frac{\theta(t)}{dt} = T(t) \tag{16}$$

By considering that the generated torque is directly proportional to the supplied current into the rotor, the torque constant K_m yields

$$T(t) = K_m i(t) \tag{17}$$

Combining Equations 16 and 17 eventually yields

$$I\,\frac{d^2\theta(t)}{dt} + c\,\frac{\theta(t)}{dt} = K_m\,i(t) \tag{18}$$

The resulting mechanical power is given by

$$P_{mec}(t) = T(t)\dot{\theta}(t) \tag{19}$$

5.4.2 Electrical equations

The electrical part composing the DC motor is the so-called armature circuit. In this case, the armature circuit is composed of an equivalent resistance R, an equivalent inductance L and a back electro-motive force e appearing in the rotor of the motor due to the variation of magnetic field direction in the coils forming the motor. From Kirchhoff's law, the supplied voltage V is given by

$$V(t) = R\,i(t) + L\,\frac{di(t)}{dt} + e(t) \tag{20}$$

This induced voltage is proportional to the rotational speed of the rotor by a factor that corresponds to the DC motor's back electro-motive force constant K_e

$$e(t) = K_e\,\frac{d\theta(t)}{dt} \tag{21}$$

Combining Equations 20 and 21 eventually yields to the final electrical equation

$$V(t) = R\,i(t) + L\,\frac{di(t)}{dt} + K_e\,\frac{d\theta(t)}{dt} \tag{22}$$

The resulting electrical power is given by

$$P_{el}(t) = V(t)i(t) \tag{23}$$

5.5 Test bench dynamics

5.5.1 Series elastic actuator

In the case of the test bench dynamic modelling, a damper-spring-damper is considered. A spring of stiffness k is connecting the series elastic actuator and its load. A damper is taken into account for both parts of the test bench and physically represents the viscous friction and dissipation. The representation of the system is available in Figure 30. It consists of a rotating two degrees of freedom system.

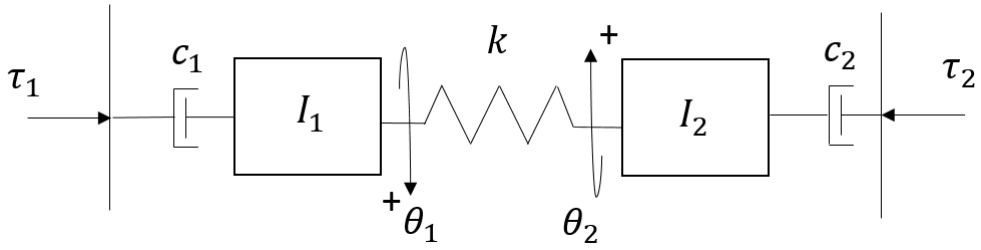

Figure 30 – Two degrees of freedom damped system

Generally speaking, the system can be mathematically represented by the application of the angular momentum theorem as

$$\mathbf{I}\ddot{\boldsymbol{\theta}} + \mathbf{C}\dot{\boldsymbol{\theta}} + \mathbf{K}\boldsymbol{\theta} = \mathbf{T}(\mathbf{t}) \tag{24}$$

where $\boldsymbol{\theta}$, $\dot{\boldsymbol{\theta}}$ and $\ddot{\boldsymbol{\theta}}$ denote respectively the position, speed and acceleration vectors. $\mathbf{I}$, $\mathbf{C}$ and $\mathbf{K}$ are respectively the inertia, damping and stiffness matrices. $\mathbf{T}(\mathbf{t})$ is the excitation force vector applied on each body as a function of time $\mathbf{t}$.

Considering the mechanical configuration of Figure 30 and by assumption of proportional damping, the system becomes

$$\begin{pmatrix} I_1 & 0 \\ 0 & I_2 \end{pmatrix}\begin{pmatrix} \ddot{\theta}_1 \\ \ddot{\theta}_2 \end{pmatrix} + \begin{pmatrix} c_1 & 0 \\ 0 & c_2 \end{pmatrix}\begin{pmatrix} \dot{\theta}_1 \\ \dot{\theta}_2 \end{pmatrix} + \begin{pmatrix} k & -k \\ -k & k \end{pmatrix}\begin{pmatrix} \theta_1 \\ \theta_2 \end{pmatrix} = \begin{pmatrix} \tau_1 \cdot i_{HD} \\ \tau_2 \cdot i_{RED} \end{pmatrix} \tag{25}$$

The subscribed numbers 1 and 2 are related to the inertia I, damping c, angular position θ, angular speed $\dot{\theta}$, angular acceleration $\ddot{\theta}$ and torque τ of the actuation part and load part, respectively. The reduction ratio of the harmonic drive ($i_{HD} = 160$) is associated to the actuation part, while that of the planetary gear box ($i_{RED} = 66$) is associated to the load part.

The known controlled variables are τ_2 and, θ_1, $\dot{\theta_1}$ and $\ddot{\theta_1}$. Even if the inertia of each part of the shaft, stiffness of the spring and damping of the motors are provided in the datasheets by the manufacturers, these would certainly not be reliable in practice. The assembly of the test bench, alignment or loading effects can have a high influence on it.

From Equation 25, the transfer functions of the global system can be obtained through:

$$\begin{cases} I_1\ddot{\theta_1} + c_1\dot{\theta_1} + k\theta_1 = i_{HD}\tau_1 + k\theta_2 \\ I_2\ddot{\theta_2} + c_2\dot{\theta_2} + k\theta_2 = i_{RED}\tau_2 + k\theta_1 \end{cases} \tag{26}$$

The transfer functions of the system can be developed from Equation 26 through Laplace transform as a function of speed, one gets

$$\begin{cases} (I_1 s^2 + c_1 s + k)\frac{W_1(s)}{s} = i_{HD}T_1(s) + k\frac{W_2(s)}{s} \\ (I_2 s^2 + c_2 s + k)\frac{W_2(s)}{s} = i_{RED}T_2(s) + k\frac{W_1(s)}{s} \end{cases} \tag{27}$$

The solution of the problem is obtained through

$$[(I_1 s + c_1 + \frac{k}{s})(I_2 s + c_2 + \frac{k}{s}) - \frac{k^2}{s^2}]W_2(s) = (I_2 s + c_2 + \frac{k}{s})i_{RED}T_2(s) + \frac{k}{s}i_{HD}T_1(s) \tag{28}$$

The four transfer functions are then obtained by computing the ratio of the angular velocity and the torque between each bodies.

$$H_1(s) = \frac{W_1(s)}{T_1(s)} = \frac{i_{HD}(I_2 s^2 + c_2 s + k)}{s^3(I_1 I_2) + s^2(I_1 c_2 + I_2 c_1) + s(c_1 c_2 + k(I_2 + I_1)) + k(c_1 + c_2)} \tag{29}$$

$$H_2(s) = \frac{W_1(s)}{T_2(s)} = \frac{i_{RED}k}{s^3(I_1 I_2) + s^2(I_1 c_2 + I_2 c_1) + s(c_1 c_2 + k(I_2 + I_1)) + k(c_1 + c_2)} \tag{30}$$

$$H_3(s) = \frac{W_2(s)}{T_1(s)} = \frac{i_{HD}k}{s^3(I_1 I_2) + s^2(I_1 c_2 + I_2 c_1) + s(c_1 c_2 + k(I_2 + I_1)) + k(c_1 + c_2)} \tag{31}$$

$$H_4(s) = \frac{W_2(s)}{T_2(s)} = \frac{i_{RED}(I_1 s^2 + c_1 s + k)}{s^3(I_1 I_2) + s^2(I_1 c_2 + I_2 c_1) + s(c_1 c_2 + k(I_2 + I_1)) + k(c_1 + c_2)} \tag{32}$$

such that

$$W_1(s) = H_1(s)T_1(s) + H_2(s)T_2(s) \tag{33}$$

$$W_2(s) = H_3(s)T_1(s) + H_4(s)T_2(s) \tag{34}$$

5.5.2 Direct actuator

In the case of the direct actuation, by comparison with the transfer functions associated with the series elastic actuator, there is no spring connecting the actuator and the load part. The connection is supposed to be perfectly rigid and the stiffness of infinite value, by definition. This also means that the two parts of the test bench form a unique body of inertia $I_1 + I_2$. Contrary to the series elastic actuator, both parts of the axis have the same position, which means that

$$\theta_1 = \theta_2 \tag{35}$$

The equation of motion becomes

$$(I_1 + I_2)\ddot{\theta}_1 + (c_1 + c_2)\dot{\theta}_1 = i_{HD}\tau_1 + i_{RED}\tau_2 \tag{36}$$

Once again, the transfer functions are found through Laplace transform as

$$H_1(s) = \frac{W_1(s)}{T_1(s)} = \frac{i_{HD}}{(I_1 + I_2)s + (c_1 + c_2)} \tag{37}$$

$$H_2(s) = \frac{W_1(s)}{T_2(s)} = \frac{i_{RED}}{(I_1 + I_2)s + (c_1 + c_2)} \tag{38}$$

6 Experimental procedure

6.1 Goal

The purpose of this section is to determine how the test bench will be analysed and its functioning verified. Different configurations of the actuation systems will be tested: the directly actuated system (DA), the series elastic actuator system (SEA) and the clutchable series elastic actuator system (CSEA).

The sensors used for the measurements are the torque transducer at the load motor, the load cell at the test motor, the encoders at the motors, and the voltage and current sensors to measure the electrical consumption. The experimental tests are implemented on *LabView* and launched on the test bench through the interface described in Section 4.2. The data are recorded by the microcontroller and analysed with *Matlab* and *Excel*.

The experimental procedure of the measurements on the test bench is done according to the type of signal trajectories that can be applied by the user to the motors. From a physical point of view, the trajectory references can either be the position, the speed or the torque. During experiments, the trajectory references used can either be constant signal values, sine wave trajectories, double sine wave trajectories or gait trajectories. For each configuration, the user is also able to mention the amplitude of the signal and its corresponding frequency.

To track the trajectories, control systems have to be experimentally tuned. Open-loop, as well as closed-loop control systems, can be performed, depending on the type of measurement that has to be performed.

The final goal is to evaluate the behaviour of the actuator for healthy human gait. A controlled position trajectory signal is imposed to the test motor while a controlled load torque signal is imposed to the load motor. The test motor is supposed to be able to maintain the reference signal whatever the load applied at the other extremity of the shaft. At the end of the measurements, the performances of the actuators are evaluated, and compared based on a *Simulink* simulation.

The sign convention applied to the test bench is shown in Figure 31. The extension torque, as represented in Figure 32b is considered as positive torque. This externally applied torque represents what the muscles have to provide during human gait. The quadriceps are then working in this case positively. Concerning the reference signal of the load motor, the goal is to recreate the ground reaction torque. In such case, the torque to apply is the inverted one of the signal represented in Figure 32b.

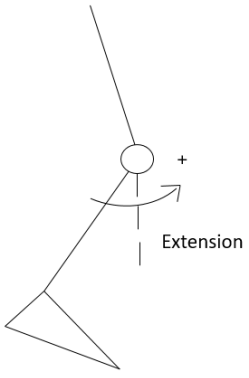

Figure 31 – Sign convention of positive extension of the shank relative to the thigh

The gait parameter values extracted from [6] will be used in the following of this work. This work compares the gait parameters among 20 adult (between 20 and 72 years) and 20 young (between 6 and 17 years) healthy subjects. These subjects have a rather slow walking speed of about 0.9 [m/s]. The knee angle θ, knee torque τ, knee power P over the gait cycle are represented in Figures 32a, 32b and 32c, respectively. These variables are represented as functions of the percentage of completion of the gait sequence. The knee stiffness can also be represented as the slope of the torque-angle characteristics curve, as represented in Figure 32d. Because the morphology of each subject is different, all the respective gaits are also different. The red curves are standing for the mean values of the measured parameters, while the yellow and blue ones are standing for the standard deviation of the measurements around the mean values.

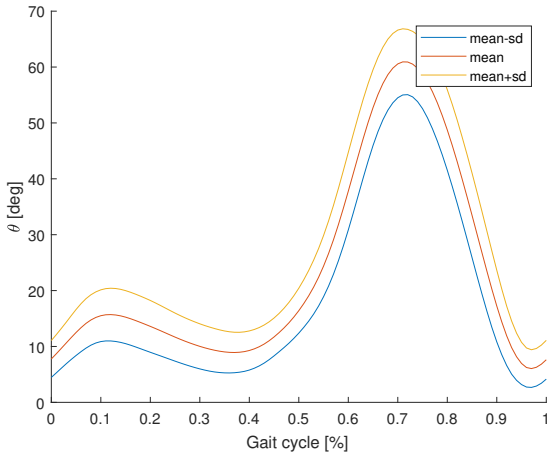

(a) Knee angle as a function of the percentage of gait cycle

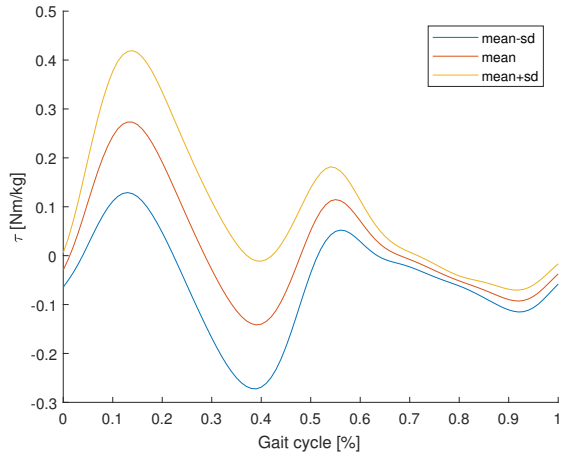

(b) Knee torque as a function of the percentage of gait cycle

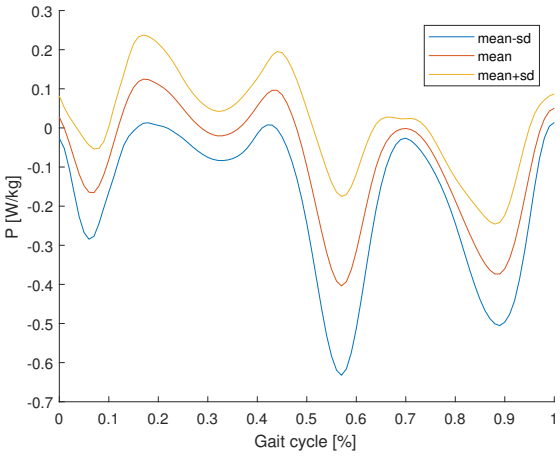

(c) Knee power as a function of the percentage of gait cycle

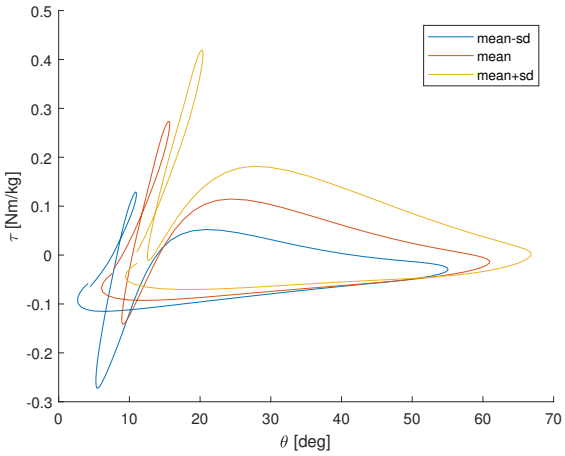

(d) Knee torque as a function of the knee angle

Figure 32 – Theoretical gait data

However, as detailed in Section 6.4, the test bench is not able to reach experimentally such high gait velocities combined with high torques.

6.2 Experimental control tuning

The role of the controller is to perform a feedback control of the system. There are existing a lot of different types of controllers. In the case of the test bench, a PID controller will be used for the direct actuation and the series elastic actuation while an impedance control is utilised in

the case of the clutchable series elastic actuator.

A system can be represented by its transfer function. The condition of stability of the system is met when all the poles of the transfer function are located on the left side of the polar plot. Namely, the real part of the poles has to be negative while the frequency of the oscillations of the system is determined by the imaginary part of the poles. Thanks to the controller placed in the closed-loop of the system, the poles of the transfer function can be changed, and the stability of the system can be corrected.

6.2.1 Control quality requirements

The performances of the controller are evaluated based on

- Settling time t_s: it represents the time that the response signal takes to be located in a region comprised around, generally, 5% of its reference value.
- Maximum overshoot M_p: it represents the maximum amplitude overlap of the response signal towards the reference value.
- Peak time t_p: it represents the response signal time associated to the maximum overshoot M_p.
- Rise time t_r: it represents the reactivity of the system. It is usually measured at the time corresponding to 90% of the amplitude of the reference signal.

The experimental tuning of the controllers has to be done firstly with a steady-state step function before refining it for dynamic trajectory purpose.

6.2.2 PID formulation

The PID controller is a combination of a proportional (P), integral (I) and derivative (D) actions. The implementation of such controller is simple and robust. The controller is producing a command signal $u(t)$ such that the error signal $e(t) = y(t) - u(t)$ between the reference value and the measured value is converging to 0. Mathematically, it can be expressed as

$$u(t) = k_p e(t) + k_i \int_0^t e dt + k_d \frac{de(t)}{dt} \tag{39}$$

The effect of the parameters are the following

1. Proportional parameters k_p
   - Reduces error as overshoot
   - Increases the bandwidth
   - Can make the system unstable if the parameters are badly chosen
2. Integral parameters k_i
   - Suppresses static error
   - Is proportional to the magnitude and duration of the error
   - Can cause overshoot proportional to the accumulation of the error over time
3. Derivative parameters k_p
   - Anticipates the system behaviour
   - Damps the system
   - Is highly sensitive at high frequency. Indeed, it is preferable to avoid the use of a derivative term at high frequency. For example, if the input reference of the system has the behaviour of a sinusoidal signal,

     $$i(t) = \sin(\omega t) \tag{40}$$

     which gives through derivation,

     $$\frac{di(t)}{dt} = \omega \cos(\omega t) \tag{41}$$

The signal will then be amplified by the frequency, which may quickly lead to instabilities of the system. In practice, there is inevitable high-frequency noise to which the control law can be not very well adapted. High derivative parameters have to be generally avoided in the typical case of experimental testing.

The tuned controller, for each experimental tests, is mentioned explicitly in the following of this thesis.

6.2.3 Impedance control formulation

An impedance control has been implemented in the *LabView* software to control the clutchable series elastic actuation. The general principle of the impedance control is to virtually add a desired stiffness k_d and damping d_d, located mutually in series with the series elastic actuation. This enables to control the mechanical impedance of the system by the relative motion control of the elastic actuator. More details can be found in [12].

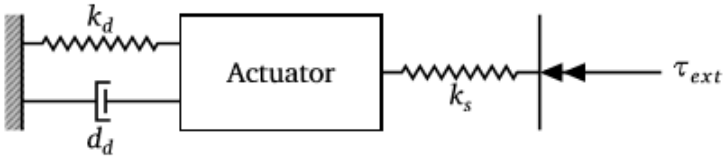

Figure 33 – Impedance control [12]

6.3 Perturbation sources

6.3.1 Friction and backlash

Friction is the mechanical resistance tangential force resulting from the contact between body surfaces. As represented in Figure 34, the friction is appearing in various forms. It depends strongly on the material physics of the bodies, the roughness of the contact surface, the lubrication, relative velocities as well as shaft misalignment.

The stiction is the static force required to split up stationary surfaces. On the other hand, the Coulombic force is generally constant, and it represents the tangential resistance force to counteract to generate a movement along the interfaces. Some systems, as DC motors, also exhibit viscous drag velocity which is directly proportional to the movement velocity [51].

The effect of friction on the numerical data is highly viewable and can be roughly estimated through friction models. It depends strongly on the amplitude and the frequency of the command signals.

On the other hand, backlash is also present on the test bench. It corresponds to the gap that can particularly exist in the gear boxes between the gear teeth. When changing of speed direction, the backlash causes the driven machine to rotate freely up to get in contact with the adjacent gear tooth. It is introducing an additional delay in the transmission, leading to hysteresis effect and non-linearity, depending on the actuation direction.

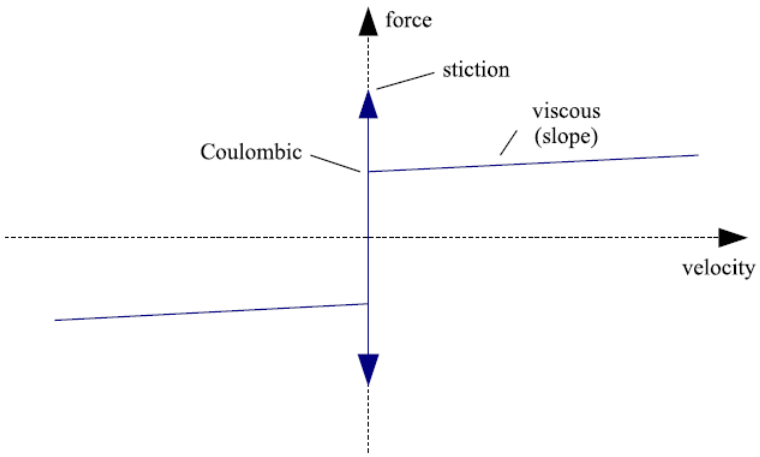

Figure 34 – Mechanical friction between body surfaces [51]

6.3.2 Noise, offset and simultaneity

Signal noise has to be properly filtered to analyse the data. Furthermore, one should also be careful of the simultaneous recordings of the data. Cables positions of the sensors are also highly influencing the measurements as well as the stability of the table on which the test bench takes place. Furthermore, some signal offsets have also to be taken into account even after the calibration of the sensors.

6.4 Gait limitation and scaling

First of all, the knee torque-speed characteristics is represented in Figure 35. This general case corresponds to subjects of 70 [kg] performing one gait cycle each second.

As it can be seen, four zones, corresponding to two different modes of operation, are present on the torque-speed characteristics:

1. Braking mode
   - Negative torque on the load motor and positive speed on the test motor
   - Positive torque on the load motor and negative speed on the test motor
2. Acceleration mode
   - Positive torque on the load motor and positive speed on the test motor
   - Negative torque on the load motor and negative speed on the test motor

The four regions are investigated to constitute the operational modes of the test bench and to find the best way to evaluate it.

One main problem that is directly met when adding increasing loading is that the test motor suddenly stops, caused by the safety limitations of its drivers when the nominal current is reached. The current limitations are for the test and load drivers of [-15;15] [A] and [-6;6] [A], respectively. Concerning the accelerating mode for which the two motors have the same direction of actuation, the limitations are expected to coincide with the maximum power that the hardware components can deliver. Concerning the braking mode, the actuation directions of both motors are opposite. This means that one motor tries to accelerate while the other one is braking. The limitations, in this case, are expected to be from the absorbing power capability of the hardware. There is a compromise to find between the bigness of the velocity and the torque to impose on the test bench.

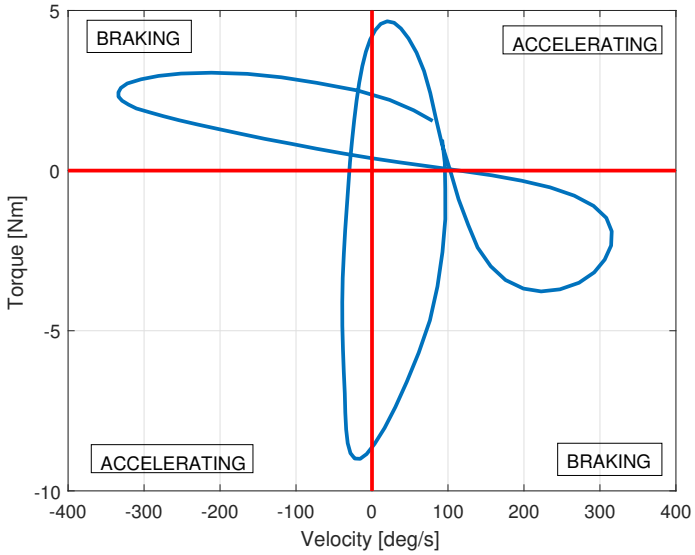

Figure 35 – Gait parameters and division of the modes

Care should then be taken for the imposed velocities and torques to avoid to activate the emergency stop or to break the devices.

6.4.1 Accelerating mode

Concerning the accelerating mode, the power flow is represented in Figure 36. In this case, both motors are putting mechanical power on the test bench at both sides of the harmonic drive and are rotating in the same direction.

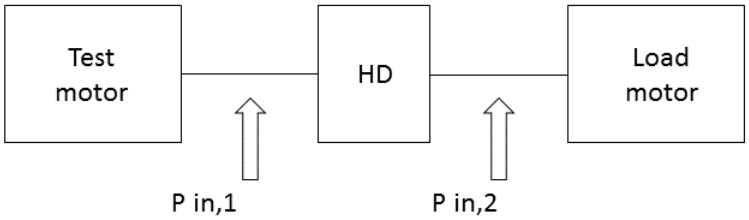

Figure 36 – Power flow in accelerating mode

After experimental trials, the driver of the load motor always shoots the first due to lower current limitation. From the datasheets of the driver (*ESCON*), it is described that the driver should always be supplied by a power source of

$$50 \geq V_{cc} \geq [\frac{U_N}{n_0}(n + \frac{\Delta n}{\Delta M}M) \cdot \frac{1}{0.98}] + 1 \tag{42}$$

where V_{cc} [V] is the power supply voltage of maximum magnitude of 50 [V]. Note also that the power supply in the laboratory is not able to supply such high voltage because it supplies also other electronic components which have lower limits. In such a case, the V_{cc} is limited to 48 [V]. U_N [V] is the nominal motor voltage, n_0 [rpm] is the motor no load speed at U_N, n [rpm] is the operating speed, $\frac{\Delta n}{\Delta M}$ [rpm/mNm] is the speed/torque gradient of the motor and M [mNm] is the operational torque.

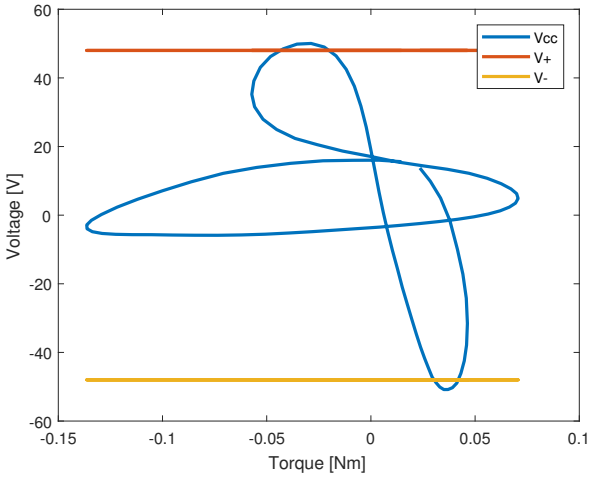

Figure 37 – Voltage limitation for the acceleration mode

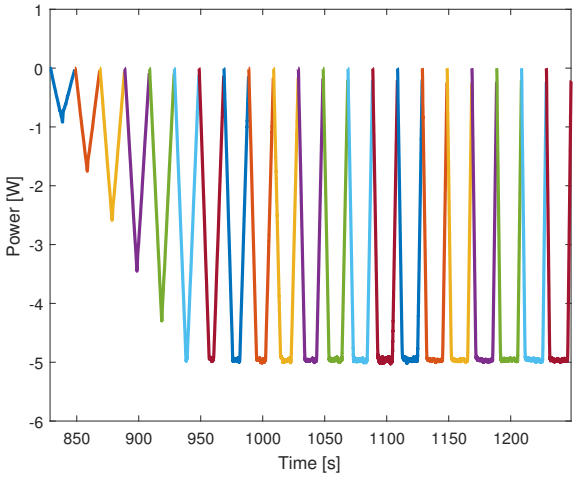

Figure 38 – Absorbed power limitation to an incremental load torque of 0.5 Nm at each new cycle, in the case of the braking mode

From a purely theoretical point of view, it can be seen in Figure 37 that the gait data scaling has well to be performed when the motor is in the accelerating mode. Indeed, the driver voltage is, for some points, located over the limitations.

On the other hand, one unknown is how large the motor can brake and therefore work as a generator. In fact, the limitation does not come from the motor on itself but from the driver and power supply which have not be configured to absorb such significant electrical power. The power supply has to be capable of receiving energy from the motor and stock or dissipate it through capacitors. In conclusion, the braking limitations of the load motors have to be carefully manually investigated through the experiments, as detailed in Section 6.4.2.

6.4.2 Braking mode

Regarding the braking mode, the imposed velocities and torques have opposite signs. By knowing that the motors on the test bench are located in a dual configuration, this means that the load motor has to brake when the axis is driven by the test motor. This also means that the global power flow of the system goes from the power input provided by the test motor to the power output of the load motor, passing through the harmonic drive, as represented in Figure 39.

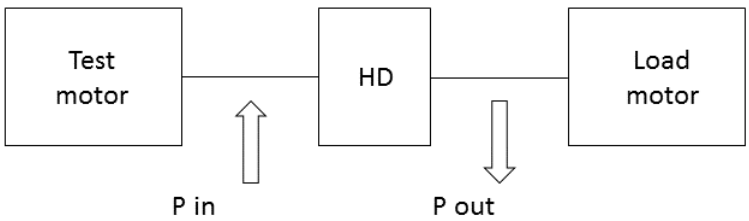

Figure 39 – Power flow in braking mode

The load motor is, in that case, absorbing the energy. In that case, hardware limitations appear. The current limitations of the driver have to be tested experimentally with taking care of the safety of the hardware. This constraint that the gait has to be scaled both in velocity and in

torque.

The experimental test done is measuring the response of a controlled triangle wave position at the test motor of constant maximum amplitude, with an incremental load torque of 0.5 [Nm] at each new cycle at the load motor side. If the current limitation of the driver is becoming higher, a risk of breaking is taken by burning the driver. In Figure 38, it can be seen that the driver braking power limitation of the load motor cannot absorb over 5 [W] before it shuts off.

To conclude, the gait to perform is scaled and is represented in Figure 40. The actuation system is tested for the case of gait cycles of 0.4 [Hz] corresponding to a gait cycle with a period of 2.5 seconds, such that the maximum applied external torque is 9 [Nm]. Note that in practice, the user is supposed to walk with clutches and all its weight is not supported by the orthosis.

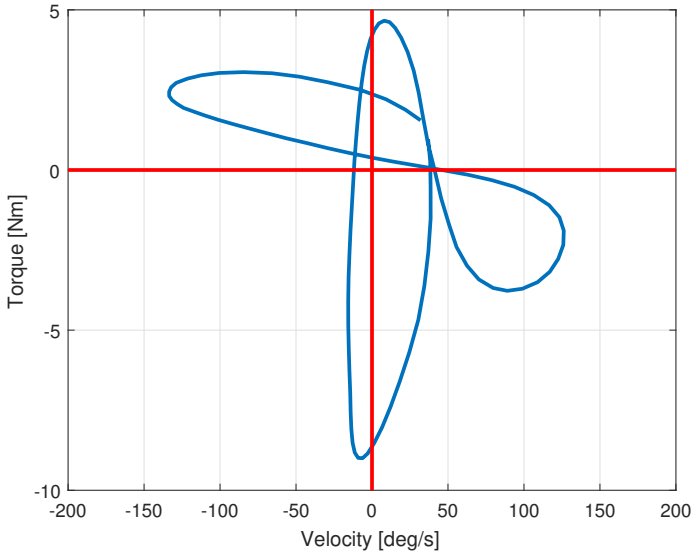

Figure 40 – Scaled gait parameters and division of the modes

According to the scaling, it is found that an 8^{th} order Fourier series can be used to adjust the curve as close as possible. The speed characteristics is computed through numerical derivation of the gait angle.

Mathematically, an 8^{th} order Fourier series is described as

$$\begin{aligned} f(x) = a_0 &+ a_1 cos(x\omega) + b_1 sin(x\omega) + a_2 cos(2x\omega) + b_2 sin(2x\omega) \\ &+ a_3 cos(3x\omega) + b_3 sin(3x\omega) + a_4 cos(4x\omega) + b_4 sin(4x\omega) \\ &+ a_5 cos(5x\omega) + b_5 sin(5x\omega) + a_6 cos(6x\omega) + b_6 sin(6x\omega) \\ &+ a_7 cos(7x\omega) + b_7 sin(7x\omega) + a_8 cos(8x\omega) + b_8 sin(8x\omega) \end{aligned} \tag{43}$$

It is chosen to norm the signals in order to be able to change them as easily as possible by only multiplying it by the desired value of amplitude. When computing the Fourier series it is theoretically advisable to use a series of three cycles so that the end of a cycle corresponds well to the beginning of the next cycle. The values of the parameters are available in Table 20 in the Appendix.

7 Physical parameters identification

Because all the measurements contain a lot of non-linearities, noise and are highly influenced by static friction and damping, the identification of the physical parameters is far from trivial. By taking all the perturbation sources into account, differences between the theoretical physical parameters and the experimental ones will inevitably appear. To identify the physical parameters influencing the dynamics of the system, the method used is a *top-down* decomposition of the problem for which firstly linear regression is used to approximate roughly the parameters. Non-linearities will then be progressively introduced in the model to match as closer as possible the reality.

Firstly, the parameters are identified through:

1. Identification of the equivalent stiffness of the series elastic actuator thanks to a load torque control.
2. Identification of equivalent inertia, damping and static friction torque on the actuation and load parts of the test bench, respectively. This is done thanks to an open-loop step response analysis to an input torque. This is a time domain analysis.
3. Identification of the dynamics of the global test bench assembly. This is a frequency domain analysis.

The results of both temporal and frequency domain analyses are complementary and will be criticised to obtain a correct equivalent estimation of the parameters.

7.1 Stiffness

To evaluate the effect of the use of the series elastic actuator, the stiffness of the torsional springs has to be experimentally determined. The theoretical designed value of the stiffness is 257.4 [Nm/rad]. However, due to the assembly configuration, it is advisable to reevaluate it in the case of the test bench.

When a load torque τ_2 is applied to the series elastic actuator, this one can be expressed as the product of the stiffness of the torsional springs and the angular deflection of the shaft, as

$$\tau_2 = k(\theta_1 - \theta_2) \tag{44}$$

where k is the equivalent stiffness and, θ_1 and θ_2 are the angular positions of the test and load motor, respectively.

Experimentally, the test motor is removed from the axis, and only the electromagnetic clutch is used to lock the test part at the harmonic drive level at a zero constant angular position. This imposes that $\theta_1 = 0$ [rad]. The angular position of the load motor is measured for different increments of positive and negative load torques, as it is represented in Figure 41a. The resulting stiffness is the slope of the curve, as represented in Figure 41b. The resulting experimental stiffness is computed by linear regression of the measurements, and a removing of the offset between the negative and positive applied torques has to be applied. This is resulting in an experimental stiffness of

$$k = \frac{\tau_2}{\theta_2} = 340.54[\text{Nm/rad}] \tag{45}$$

The experimental computed stiffness is much higher than the one designed initially. The measurement is highly influenced by the assembled components in series as elastic couplings and the harmonic drive. The experimentally computed stiffness can be so seen as the equivalent stiffness of the system.

The torsional stiffness of the harmonic drive can be evaluated thanks to the datasheets. It is known that the stiffness of the harmonic drive is varying with the magnitude of the applied torsional torque. Indeed, by considering the tested torque range, it is specified that for the load torque under 7 [Nm], the torsional stiffness corresponding to the harmonic drive is $1.3 \cdot 10^4$ [Nm/rad].

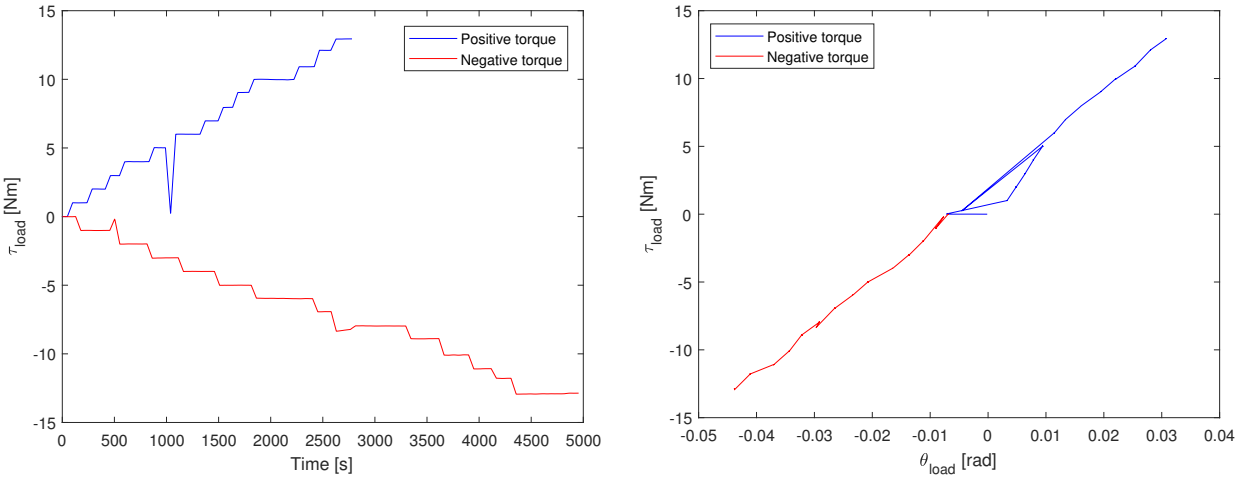

(a) Tested load torques

(b) Angular position of the load motor

Figure 41 – Stiffness evaluation

7.2 Inertia

7.2.1 Theoretical inertia

Thanks to the datasheets, the theoretical inertia of most of the bought components of the test bench can be found. The theoretical inertia of the manufactured elastic part is found thanks to the *SolidWorks* approximation. Note that no data of the ball bearings were available and are not taken into account in this theoretical inertial approximation. The values are available in Table 5. The components are enumerated from the motor to the elastic component as represented in Figure 14, for each part. The inertia of the aluminium shaft is also available.

Inertia actuation part [kgm^2]						
Test motor	Coupling 1	Clutch	Reduction	Harmonic drive	Elastic	Al rod
$1.81 \cdot 10^{-5}$	$2.9 \cdot 10^{-6}$	$2.1 \cdot 10^{-6}$	$9 \cdot 10^{-6}$	$1.8 \cdot 10^{-3}$	$4.771 \cdot 10^{-4}$	$2.71 \cdot 10^{-4}$
Inertia load part [kgm^2]						
Load motor	Reduction	Coupling 3	Torquemeter	Coupling 4	Elastic	Al rod
$1.21 \cdot 10^{-4}$	$1.67 \cdot 10^{-6}$	$1.8 \cdot 10^{-4}$	$4 \cdot 10^{-5}$	$1.8 \cdot 10^{-4}$	$4.912 \cdot 10^{-4}$	$3.73 \cdot 10^{-4}$

Table 5 – Test bench inertias

By taking the reduction ratios $i_{HD} = 160$ and $i_{RED} = 66$ into account, the inertia I_1 of the actuation part as well as the inertia I_2 of the load part can be computed as

$$I_1 = (I_{test} + I_{Coupling1} + I_{Clutch} + I_{HD}) \cdot i_{HD}^2 + I_{Coupling2} + I_{Elastic} + I_{rod} = 0.824[\text{kg m}^2] \quad (46)$$

$$I_2 = (I_{load} + I_{red}) \cdot i_{RED}^2 + I_{Coupling3} + I_{Torquemeter} + I_{Coupling4} + I_{Elastic} + I_{rod} = 0.535[\text{kg m}^2] \quad (47)$$

Because of the perturbation sources, the experimental inertia is expected to be higher. Note that no information about the damping and friction are at this stage theoretically well available,

except for the cases of the viscous friction of the motors and of the harmonic drive. However, these have to be necessarily experimentally recomputed.

7.2.2 Step response model

By separating the test bench in its actuation and load part at the elastic level, a first approximation of the dynamics of the system is computed to extract the physical parameters. The step response model is used to evaluate the angular velocity response of the system when a step torque is send to the motor.

Mathematically, the resulting angular velocity of each part can be obtained thanks to the transformation of Equation 25, as

$$T - T_{fr,static} = I\dot{\omega} + c\omega \tag{48}$$

where T is torque of the motor, $T_{fr,static}$ is the no load starting friction torque, I is the inertia, c is the damping and ω the resulting angular velocity. Passing through Laplace transform gives

$$T - T_{fr,static} = Is\omega + c\omega \tag{49}$$

Isolating ω leads to

$$\omega = \frac{T - T_{fr,static}}{Is + c} \tag{50}$$

Resolving the inverse Laplace transform,

$$\omega = \frac{T - T_{fr,static}}{I} \int_0^\tau e^{\frac{-ct}{I}} dt \tag{51}$$

Which results in the following final expression of ω

$$\omega = \frac{T - T_{fr,static}}{c}(1 - e^{\frac{-c\tau}{I}}) \tag{52}$$

In what follows, the inertia is assumed to be constant. However, the static friction torques, as well as the damping, are varying as functions of the direction of rotation, the amplitude and frequency of the input torque. $T_{fr,static}$ and c are then only valid for the same configuration of tests and have to be recomputed for any changes in the configuration.

7.2.3 Actuation part

The series elastic actuation part is separated from the load part of the test bench at the elastic connection level. On the remaining axis, the harmonic drive is supposed to induce the main disturbance in the subsystem due to the addition of high and non-linear friction behaviour.

The responses of the system to different step input torques are represented in Figure 42a. The encoders only enable to extract the physical parameters from the dynamics of Equation 52. The experimental measurements are fitted with the theoretical ones, and the physical parameters are then computed.

As it can been seen in Figure 42a, the system is, in most cases, oscillating around an average velocity after converging. The cyclic oscillations of the curves in Figure 42a are representative of the misalignment of the system as well as the position dependence of the elastic element composing the harmonic drive. Misalignment is hard to totally remove. The fitting of the model and the measurements allows to extract the inertial parameters. The measurements concerning the load part are represented in Figure 42b and detailed in Section 7.2.4.

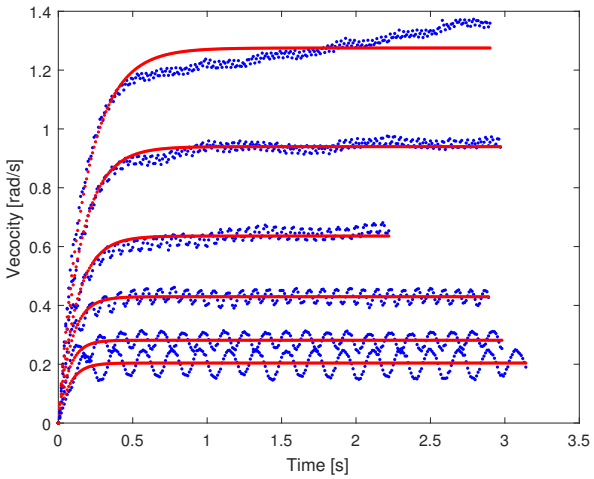

(a) Representation of the speed responses over time of the actuation part to a step load torque. The experimental data are represented in blue while the red lines are the fittings.

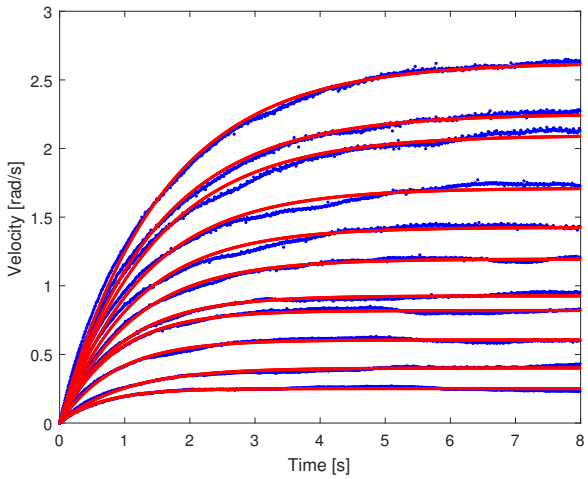

(b) Representation of the speed responses over time of the load part to a step load torque. The experimental data are represented in blue while the red lines are the fittings.

Figure 42 – Experimental responses to a step impulse

Note that the solution of the computation is not unique and is expected to be consistent with the theoretical values of inertia. The static friction $T_{fr,static1}$, damping c_1 and inertia I_1 of the actuation part are presented in Table 6.

T_1[Nm]	$T_{fr,static1}$ [Nm]	c_1[Nms/rad]	I_1[kgm^2]
5.864	4.077	8.754	0.653
6.515	3.817	9.585	0.673
7.819	4.201	8.422	0.718
9.122	4.562	7.170	0.852
10.425	4.869	5.911	0.853
11.728	5.266	5.067	0.914

Table 6 – Results of the actuation part computation

The conclusion of this numerical computation is that the system is strongly damped and contains high equivalent static friction torque. According to Table 6, the averaged inertia of the actuation part is evaluated to be of magnitude

$$I_1 = 0.825\,[\text{kgm}^2] \tag{53}$$

7.2.4 Load part

The same procedure as in Section 7.2.3 is done. The physical parameters $T_{fr,static2}$, c_2 and I_2 are extracted from the correlation of the experimental data as represented in Figure 42b. Because the load is low, the rotational resistance is low, and the system is highly reactive even for small input torques. The results of the experiments are available in Table 7.

T_2 [Nm]	$T_{fr,static2}$ [Nm]	c_2[Nms/rad]	J_2[kgm^2]
0.5	0.00002	1.989	1.324
0.6	0.00002	1.495	1.481
0.7	0.00002	1.155	0.983
0.8	0.00001	0.975	0.832
0.9	0.0009	0.97	0.927
1	0.275	0.606	0.677
1.1	0.45	0.455	0.544
1.2	0.437	0.445	0.579
1.3	0.412	0.423	0.619
1.4	0.422	0.433	0.640
1.5	0.404	0.417	0.648

Table 7 – Results of the load part computation

It can be seen that applying, in open-loop, torques over 1 [Nm] leads to a convergence of each parameter. Therefore, an averaging of the five last measurements gives an inertia of magnitude

$$I_2 = 0.605\,[\text{kgm}^2] \tag{54}$$

In comparison with the results of Section 7.2.3, the system is highly less damped, and the perturbative friction torque is much lower. There is less position dependency than for the actuation part.

7.3 Friction

In this section, a more detailed study of the static friction and damping is performed. Different methods can be performed for the evaluation of the static friction torque. The one used is applying a sinusoidal input torque to the motor. The measurements are repeated for several sinusoidal signals with increasing amplitudes and in the ranges of frequency that the test bench is supposed to be used. To evaluate the friction on the test bench for the gait application, the functioning of the test bench is localised for actuation frequencies around 0.5 [Hz].

A theoretical model is used to fit the experimental measurements as detailed in Section 7.3.1. The initial conditions are estimated thanks to a *Simulink* simulation.

7.3.1 Friction model

Friction is generally discontinued and impossible to remove. On the other hand, some mathematically models can be introduced in order to characterise it as Karnopp model, LuGre, Modified Dahl or M2 [51].

The model used in this paper is the one chosen in [12]. It is an iterative predictive model that enables to estimate the magnitude of the stiction friction ($\alpha_0 + \alpha_1$), Coulombic friction (α_1) and viscous friction (α_2) thanks to the following expression

$$T_{fr} = [\alpha_0 + \alpha_1 e^{-\beta_1|\dot{\theta}|} + \alpha_2(1 - e^{-\beta_2|\dot{\theta}|})]sign(\dot{\theta}) \tag{55}$$

where T_{fr} is the friction torque and $\dot{\theta}$ the angular velocity. This model makes the assumption that the friction torque is symmetric as a function of the velocity which may not exactly be the case in reality. According to the computed static friction, the global dynamic friction of the elastic actuator is computed thanks to Equation 48 as,

$$T_{fr}(\omega) = T_{fr,static} + c\omega = T - I\dot{\omega} - k\Delta\theta \tag{56}$$

where the last elastic term is removed when the torsional springs are not present. $\Delta\theta$ is the angular deflection between both parts of the torsional spring.

At low speed, the static friction torque is easy to estimate graphically and corresponds to the magnitude of the input torque when the velocity signal is stuck at zero velocity, or begins to rotate as presented, as an example of the *deadzones* in Figure 43d. The velocity is not able to track the required trajectory. Indeed, when changing of direction of rotation, the motor needs some time to increase its torque due to the inevitable presence of high static friction at low speed. The actuator has to provide additional torque to overcome the static friction. Note that the experimental inertia used in this part are the ones computed in Section 7.2.

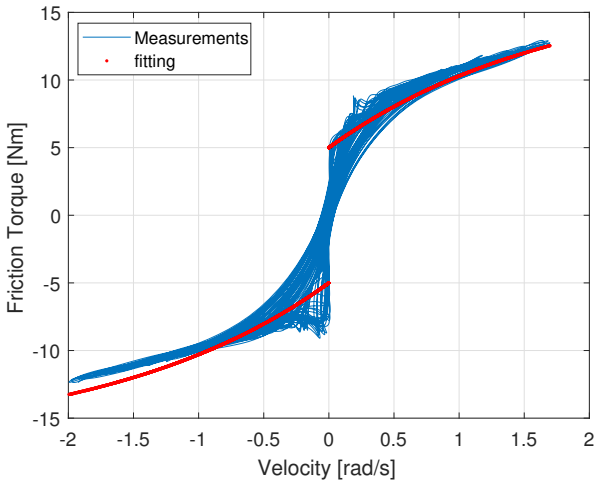

(a) Friction torque of the actuation part at a frequency of 0.5 [Hz] and for increasing applied input torque amplitude

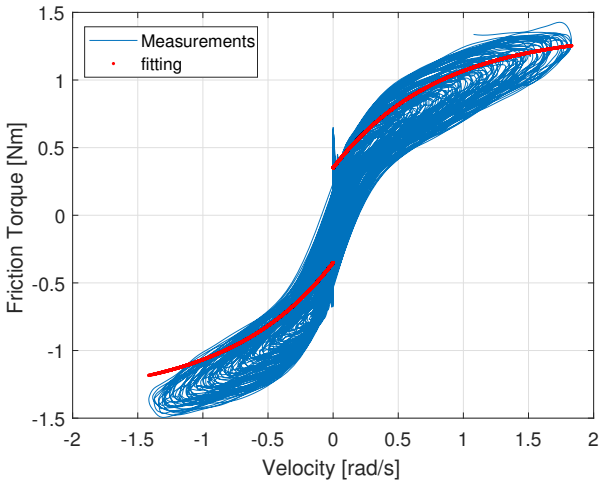

(b) Friction torque of the load part at a frequency of 0.5 [Hz] and for increasing applied input torque amplitude

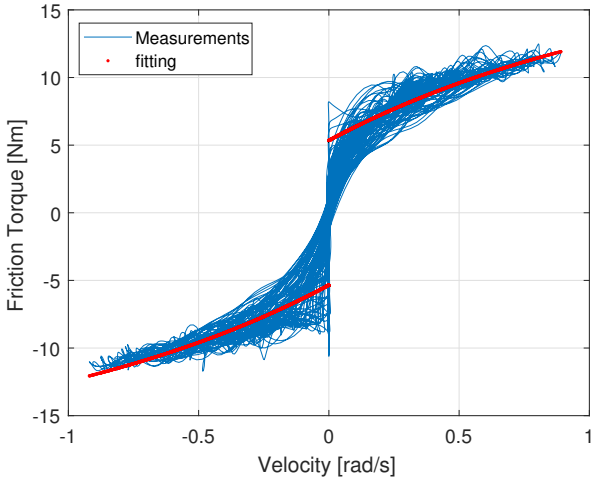

(c) Friction torque of the whole test bench at a frequency of 0.5 [Hz] for increasing applied input torque amplitude

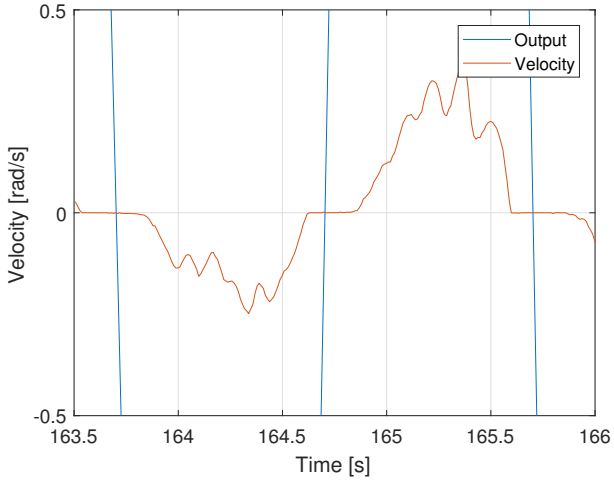

(d) Deadzone velocity signal example at 0.5 [Hz] with constant applied input torque amplitude

Figure 43 – Friction torque evaluation of the actuation and load parts

7.3.2 Actuation part

As can be seen in Figure 43a, the actuation part is highly damped and exhibits well Coulombic friction behaviour. The friction torque is computed thanks to Equation 56, while modelled by Equation 55. One should note that most of the friction is due to the harmonic drive. The relationship between the output of the controller as a function of speed is not linear, asymmetric and exhibits small hysteresis behaviour.

7.3.3 Load part

The evaluation of the friction torque of the load element is represented in Figure 43b. As can be seen, the load part is lower damped and is also asymmetric as a function of the velocity. It is due to more linearity brought by the planetary gear than the harmonic drive.

7.3.4 Global test bench

The friction torque associated to the global test bench is represented in Figure 43c. In this study, the total friction torque is supposed to be the absolute sum of the friction torque contained on both actuation and load axis of the test bench. After investigation of the initial parameters thanks to simulation, one gets the computed values of the static friction $T_{fr,static}$ and damping c as presented in Table 8. These values are considered constant for the same current ranges of frequency and amplitude.

	Global	Actuation part	Load part
$T_{fr,static}$ [Nm]	5.35	5	0.35
c [Nms/rad]	13	12	1

Table 8 – Dynamic friction torque

7.4 Frequency domain analysis

By assembling back the two parts of the test bench and adding the experimental computed stiffness k, one should be able to predict the dynamics and resonance of the system in the frequency domain, at least at a low frequency close to 0.5 [[Hz]. The assumption of damping to be constant as a function of the velocity is done at low speed.

7.4.1 Bode plots

Firstly, the experimental tests are performed in open-loop, namely without any controller. The method used is applying a sinusoidal input torque of constant amplitude and with increasing frequencies. Based on the measurements of the angular responses of both encoders, one should be able to build the Bode plots in amplitude and phase. The Bode plots are tools representing the response of the system, similar to the transfer function study. It also allows an estimation of the resonant frequency of the system to the input torques, as well as its global dynamics. Note that here, because friction is dependent on the frequency and the amplitude of the input torque, the estimations of the parameters done in Section 7 are not entirely correct in the entire frequency range. One should repeat all the tests in order to again to reevaluate them at each frequencies and amplitudes, which is not done for temporal constraints.

The analysis of the data is performed thanks to the Bode plot in amplitude and phase to eventually reach and confirm the different computed inertia, friction and damping through the whole axis of the test bench.

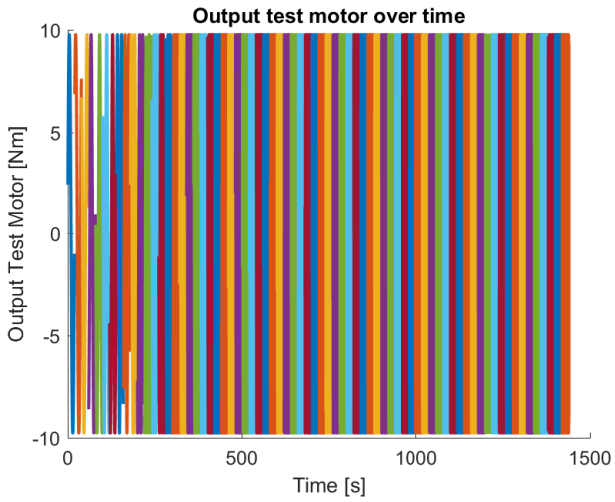

(a) Sinusoidal input torque over time with increasing frequency every 20 seconds

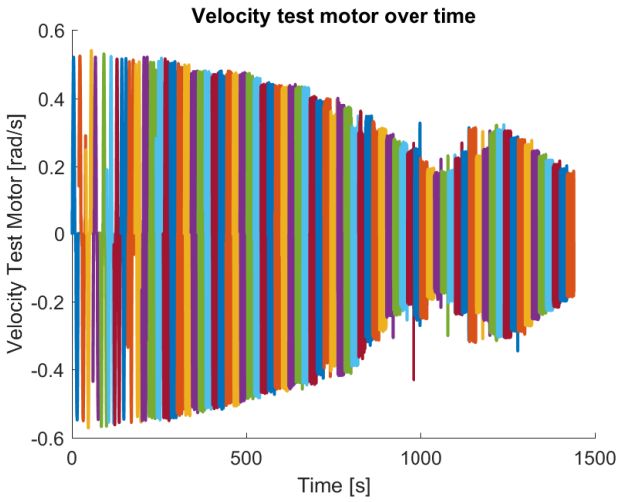

(b) Velocity output response of the test motor to an increasing of the amplitude of the input torque sinusoidal signal every 20 seconds

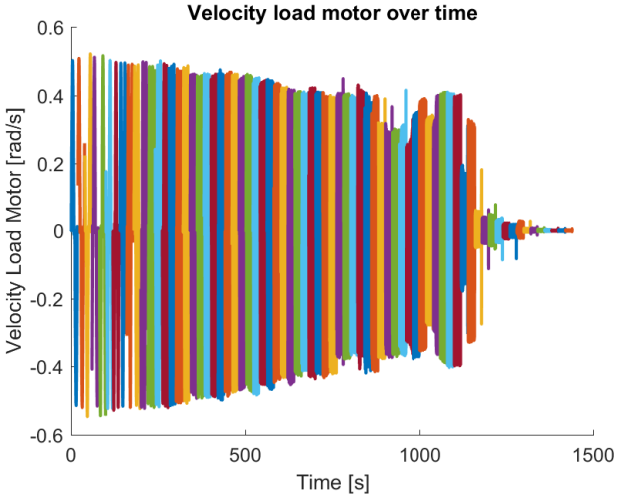

(c) Velocity output response of the load motor to an increasing of the amplitude of the input torque sinusoidal signal every 20 seconds

Figure 44 – Frequency domain input and output signals

The input torque provided to the test motor is a stepped sine signal of amplitude 10 [Nm] with a basic frequency of 0.05 [Hz]. The stepped sine signal is multiplied by a constant of $10^{\frac{1}{30}}$ [Hz] every 20 [s]. This value is freely chosen to have a sufficient number of well defined frequency step.

The behaviour of the input torque, of the test and load motor velocities are represented in Figure 44a, 44b and 44c, respectively. It can be seen that generally, the gains of the responses are decreasing with increasing excitation frequencies. Furthermore, the natural frequency of the system, and so of the torsional springs, can be observed by a sudden increase in gain in the transmission.

The amplitude and phase of the Bode plots are computed thanks to a non-linear sinusoidal

regression applied to the input torque, to test motor and load motor velocities.

$$\begin{cases} Output_{reg} = A\sin(\omega t + \phi) \\ V_{Test,reg} = A_{Test}\sin(\omega_{Test} t + \phi_{Test}) \\ V_{Load,reg} = A_{Load}\sin(\omega_{Load} t + \phi_{Load} \end{cases} \tag{57}$$

To compensate the torque lag induced by the static friction torque, the analysis should be done at least twice, first for the low-frequency excitation and after for the high-frequency excitation. The Bode plots in amplitude of the actuation part and the load part are represented in Figures 45a and 45b, respectively. To validate the identification and the Bode plot, one should be able to rebuild it by simulation. By taking the theoretical transfer functions and adding the non-linear static friction part, the simulated Bode plots are compared with the experimental ones at low frequency. For higher frequencies for which the static friction torque can be supposed as negligible, a linear prediction is presented based on the theoretical transfer functions.

Concerning the amplitude diagrams, the closer to 0 [dB], the better the output of the motor will follow its input. It is expected that the velocities of both motors will, in the beginning, have a lower velocity than the desired ones. The gains are progressively diminishing with increasing frequencies until reaching the natural frequency of the torsional spring when to speed will again increase for both motors.

A comparison of the mathematical Bode diagrams can be useful to estimate the actual inertia, damping and stiffness of the system. However, friction is strongly affecting the dynamics of the system. The resonant frequency of the system is defined as

$$\omega_0 = k\sqrt{eig\begin{pmatrix} 1/I_1 & -1/I_1 \\ -1/I_2 & 1/I_2 \end{pmatrix}} \tag{58}$$

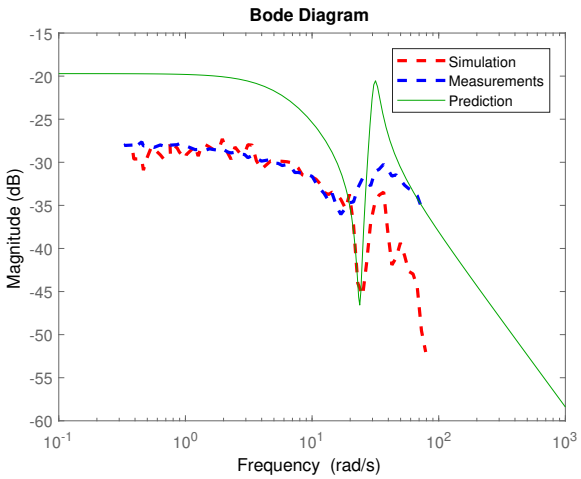

(a) Actuation part Bode plot: the measurement is the dashed blue line, the non-linear simulation is the red dashed line and the linear prediction is the green line.

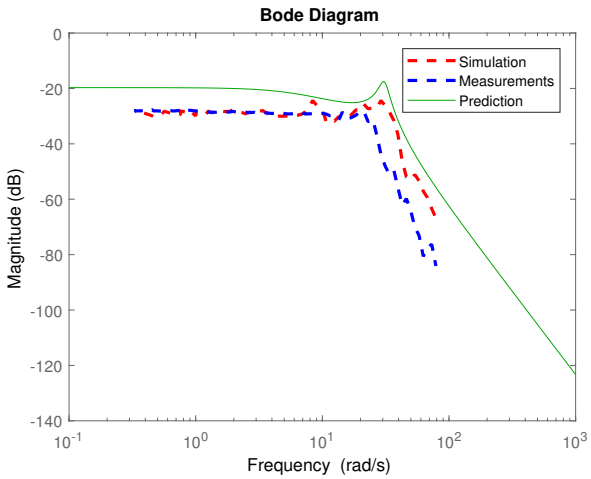

(b) Load part Bode plot: the measurement is the dashed blue line, the non-linear simulation is the red dashed line and the linear prediction is the green line.

Figure 45 – Amplitude Bode plots

The prediction has a resonant frequency of 31.23 [Hz], while the experimental one is estimated to be 21.3 [Hz] thanks to a comparative evaluation by the Complex Mode Indicator Function [42].

Concerning the actuation part, it can be observed that the simulation model is respecting well the measurements at low frequency. Indeed, the same order of values is found either for the damping and inertia. At higher frequency, the measurements are converging to the linear prediction model in which no static friction is included. However, concerning the load part, the damping is well converging to the same values compared to the simulation model. Among others, in the case of higher velocities frequencies applied to the load motor, after the resonance, the load motor is not able to handle the desired velocity since the variations are too fast. The movement cannot be transmitted to the load. There might be an equivalent reduction of the stiffness at high frequency, as well as viscous friction torque which might be not negligible compared to the other terms of the denominator of Equation 31. However, no more additional tests have been conducted and the prediction model with constant damping, inertia and stiffness will be used in this work since the tested gait is always produced at relatively low frequency.

8 Performance evaluation

8.1 Goal

The purpose of this section is to identify the performances of the system in the cases when this one is actuated thanks to the direct actuator, the series elastic actuator or the clutchable series elastic actuator. Firstly, a study of the performances of the system in steady-state mode is done to build a prediction model of the dynamic behaviour of the system. Eventually, the conclusions will be used to determine if it is consistent or not to use the series elastic actuation in this kind of application.

8.2 Definition of the performance of the system

To determine the criteria of comparison of the performances of the system, some preliminary investigation tests are performed to understand the actual behaviour of the system. The tests are conducted in the velocity-torque ranges of the human gait characteristics.

8.3 Mechanical efficiency

The mechanical efficiency of the test bench is firstly studied in both braking and accelerating modes of operation in the context of gait application. The modes were discussed in Section 6.4.

8.3.1 Braking mode

Concerning the specific case of the braking regions of the human gait cycle, the mechanical efficiency is defined as the ratio of the output power P_{out} and the input power P_{in} of the system, and can be computed as

$$\eta = \frac{P_{out}}{P_{in}} = \frac{V_{Load}\tau_{Load}}{V_{Test}\tau_{Test}} \tag{59}$$

where V_{Load} and τ_{Load} refer to the velocity and the torque of the load part of the test bench, while V_{Test} and τ_{Test} refer to the velocity and the torque of the actuation part.

In this case, the load is driven by the test motor. The efficiency computation in the accessible physical ranges is illustrated in Figures 46a and 46b for the quadrant corresponding to positive velocity at the test motor and negative torque imposed by the load motor. The same results are expected for the other braking quadrant.

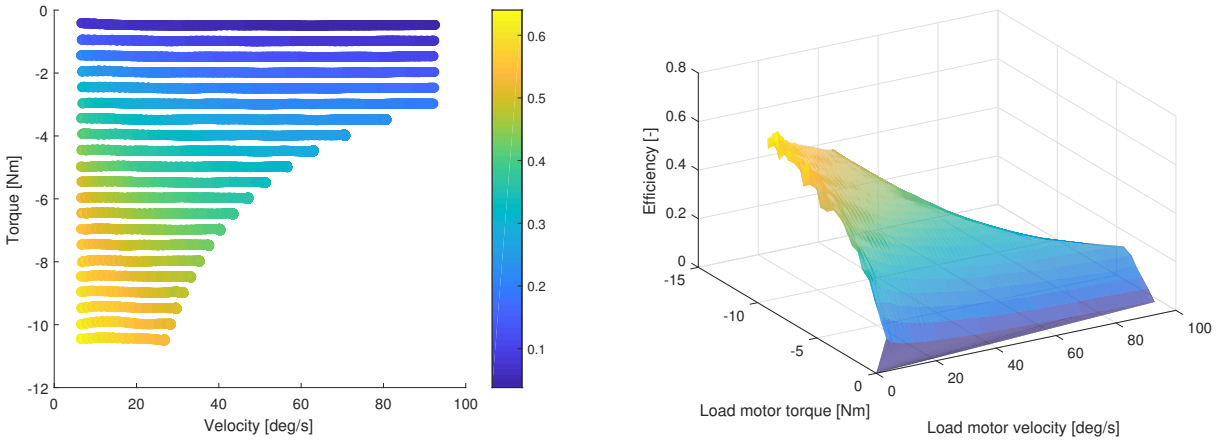

(a) Mechanical efficiency

(b) Mechanical efficiency surface fitting

Figure 46 – Evolution of mechanical efficiency in braking mode

As a conclusion, the bigger the torque and the lower the velocity, the bigger the mechanical efficiency. At constant torque, the efficiency is larger at low speed. Indeed, friction torque on the test bench increases with velocity. Unfortunately, the current model is limited by the driver safety limitations which make it stop, as it can be seen in Figure 46a. In this case, the mechanical efficiency reaches values over 0.6. This is in the range of the maximum efficiency supported by the harmonic drive.

8.3.2 Accelerating mode

Concerning the performance evaluation in the case of the acceleration mode, the notion of mechanical efficiency can not be consistently treated. Indeed, the acceleration mode can be divided into three phases, as represented in Table 9. In this table, the different phases are determined as a function of the magnitude of the test motor velocity. For each phase, it is indicated which motor is accelerating or braking. For example, by imposing a constant load motor torque, one gets

Test motor velocity [rad/s]	Accelerating motor	Braking motor	Efficiency η[-]	Comment
Very slow	Load motor	Test motor	$0<\eta=\frac{V_{Load}\tau_{Load}}{V_{Test}\tau_{Test}}<1$	Relatively high inner friction in the test motor and through the harmonic drive. The mode of operation is still in the braking mode. The test motor still drives the load.
Slow	Load motor and test motor	-	$0<\eta=\frac{V_{Test}\tau_{Test}}{V_{Load}\tau_{Load}}<1$	Static friction is crossed over and the test motor begins accelerating, with still $\tau_{Load} > \tau_{Test}$. The mode of operation switches in acceleration mode. The load drives the shaft.
High	Load motor and test motor	-	Not well defined	Both motors are accelerating and more over with higher velocities.

Table 9 – Acceleration mode phases

In the case of the test bench, the mechanical efficiency analysis cannot be performed when both imposed velocities and torques have to same sign. Indeed, both motors are inputting power that is dissipated in the form of heat and friction. The study of the mechanical efficiency of the system would not be physically consistent since the output power is not clearly measurable for this kind of application.

For this reason, one would not prefer to use the efficiency as the physical quantity to evaluate the performance of the system, but the equivalent lost torque through the harmonic drive as described in Section 8.4.

8.4 Power balance of the system

The investigation of the power balance of the system can be represented as in Figure 47. The sign convention used is also described. The shaft composed of the torsional springs of stiffness k and the harmonic drive is receiving power from the test and load motors.

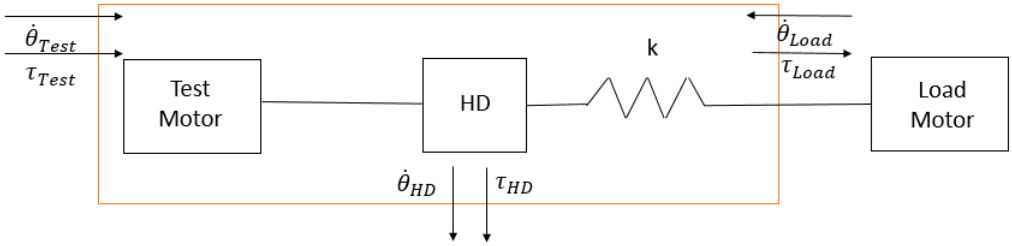

Figure 47 – Representation of the system

From a power point of view, the test bench can be represented as in Figure 48.

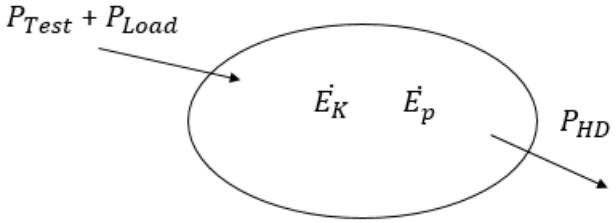

Figure 48 – Power balance representation of the system

Mathematically, the power balance is the sum of all the powers present in the system as

$$P_{Test} + P_{Load} + P_{HD} = \dot{E}_K + \dot{E}_p \tag{60}$$

Depending on if the motors are braking or accelerating and their direction of rotation, P_{Test} and P_{Load} can be negative as well as positive, while the lost power of the harmonic drive P_{HD} is always negative due to friction and heat losses. $\dot{E}_K$ is the derivative of the kinetic energy of the shaft. The kinetic energy is defined by the amount of energy involved in the rotation of the shaft. Mathematically, it can be defined as

$$E_K = \frac{1}{2}(I_{Test}\dot{\theta}_{Test}^2 + I_{Load}\dot{\theta}_{Load}^2) \tag{61}$$

where I_{Test} and $\dot{\theta}_{Test}$ denote the inertia and the velocity of the actuation part, while I_{Load} and $\dot{\theta}_{Load}$ are the ones corresponding to the load part. The derivative of the kinetic energy is defined as

$$\dot{E}_K = I_{Test}\dot{\theta}_{Test}\ddot{\theta}_{Test} + I_{Load}\dot{\theta}_{Load}\ddot{\theta}_{Load} \tag{62}$$

$\dot{E}_p$ represents the derivative of the potential energy of the system. In the case of a series elastic actuator, the potential energy corresponds to the amount of energy that can be stored in the torsional springs. By definition the potential energy can be written as

$$E_p = \frac{1}{2}k(\theta_{Test} - \theta_{Load})^2 \tag{63}$$

By derivation, one gets

$$\dot{E}_p = k(\theta_{Test} - \theta_{Load})(\dot{\theta}_{Test} - \dot{\theta}_{Load}) \tag{64}$$

In steady-state mode, the right part of Equation 60 cancels out and the power lost in the harmonic drive is

$$P_{HD,ss} = -P_{Test} - P_{Load} = \dot{\theta}_{Test}\tau_{HD,ss} \tag{65}$$

where, $\tau_{HD,ss}$ is the equivalent torque lost in the harmonic drive.

8.5 Steady-state evaluation

First of all, the performances of the system are evaluated when the system is performing in steady-state mode. Based on that results, one should be able to predict the performances of the system when working in dynamic mode.

In steady-state mode, the elastic effects are not present in the system, and the tests are performed thanks to the direct actuation system. To perform experiments with the direct actuator, the angular displacement of the torsional spring is constrained. This is made through three 3D printed plates surrounding the elastic element. They are attached to it thanks to four screws on each plate, as represented in Figure 49. The additional inertia of the plates is considered to be negligible in comparison to the one of the rest of the shaft.

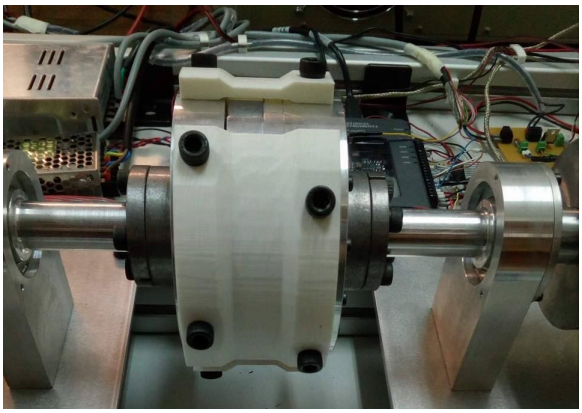

Figure 49 – Strengthening of the elastic component for direct actuation tests

The evaluation of the performance of the system as a function of its torque and its velocity is done by controlling the system in closed-loop. The velocity is controlled on the test motor while the load motor is controlled by torque, to recreate the torque-velocity relationship of the system. The controllers used in this section are PIDs and are experimentally tuned to track their imposed references. Concerning the evaluation procedure, constant velocities at the test motor and constant torques at the load motor are tested over the range of the velocity-torque characteristics covered by the human gait. The tested velocities are [-150; -130; -110; -90; -70; -50; -30; -20; 10; -6; -3; 0; 3; 6; 10; 20; 30; 50; 70; 90; 110; 130; 150] [deg/s] corresponding to the limitations of the maximum torque range that the hardware of the test bench can offer. The tested velocity-torque relationship points as well as those corresponding to the gait data which are represented in Figure 50a. Based on the filtering of the data recordings, the equivalent torque at the harmonic drive $\tau_{HD,ss}$ can be computed. For these tests, the experimental tuned parameters for the PID controllers are represented in Table 10.

	Test motor	Load motor
k_p	350	1.5
k_i	100	0.5
k_d	0	0.2

Table 10 – PID parameters

In Figure 50b, $\tau_{HD,ss}$ is represented as a surface function of the applied load torques and velocities. A 5^{th} order polynomial regression of the $\tau_{HD,ss}$ surface is used to predict the global mechanical performances of the actuation. The regression of the surface has to be done for both signs of the velocity. By naming x the torque of the load motor and y the velocity of the test

motor, one gets

$$\begin{aligned} f(x,y) = p_{00} + p_{10}x + p_{01}y + p_{20}x^2 + p_{11}xy + p_{02}y^2 + p_{30}x^3 + p_{21}x^2y \\ + p_{12}xy^2 + p_{03}y^3 + p_{40}x^4 + p_{31}x^3y + p_{22}x^2y^2 \\ + p_{13}xy^3 + p_{04}y^4 + p_{50}x^5 + p_{41}x^4y + p_{32}x^3y^2 \\ + p_{23}x^2y^3 + p_{14}xy^4 + p_{05}y^5 \end{aligned} \tag{66}$$

The associated parameters are available in Table 21 in Appendix.

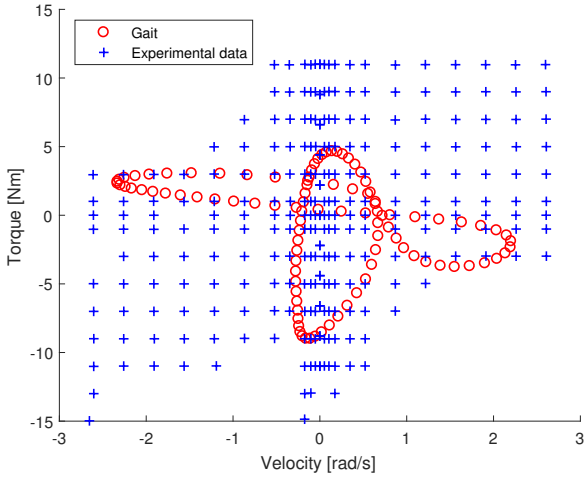

(a) Experimental data points tested on the test bench and gait data

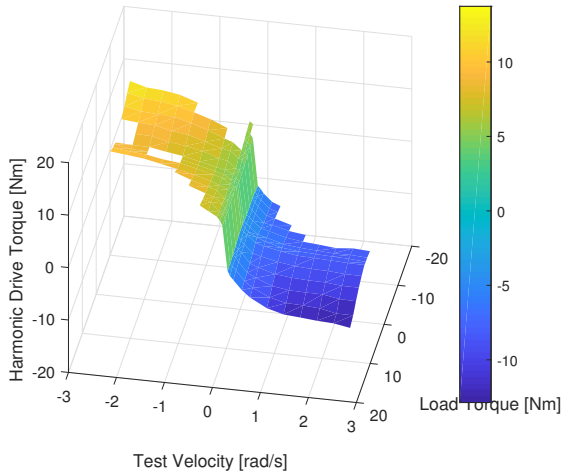

(b) Equivalent torque $\tau_{HD,ss}$ surface at the harmonic drive

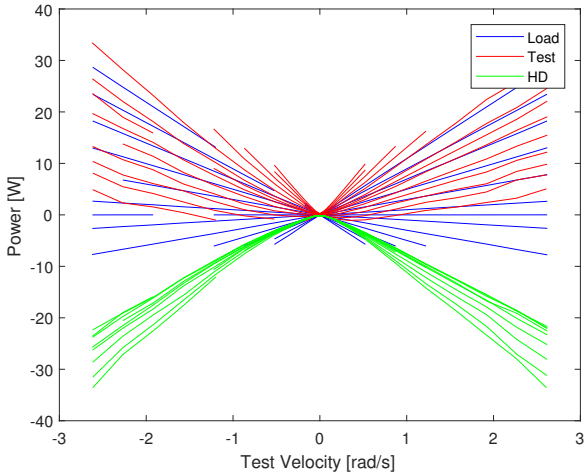

(c) Equivalent mechanical power at the harmonic drive at both motors

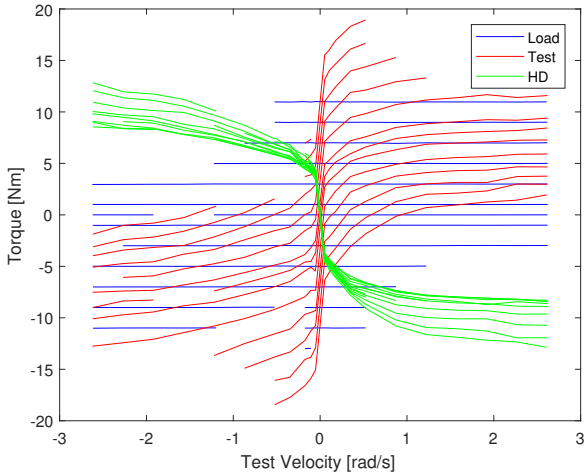

(d) Equivalent mechanical torque at the harmonic drive at both motors

Figure 50 – Steady-state evaluation

It can be noted that the surface is not perfectly symmetrical due to friction torques depending on the direction of rotation of the motors. It can be seen that the smaller the load torque, the smaller $\tau_{HD,ss}$ in absolute value. Note also that because of the no load starting friction torque, Coulombic friction is located on the zero velocity axis of the graph. Indeed, the load torque acts as a disturbance on the system that the test motor has to overcome as well. Because the harmonic drive is always the source of power losses, $P_{HD,ss}$ is indeed always negative as represented in Figure 50c. This implies that for negative velocities, $\tau_{HD,ss}$ must always be positive while negative for positive velocities.

8.6 Comparison with the datasheets of the harmonic drive

The harmonic drive is without any doubt the biggest source of friction and perturbation on the test bench. To interpret the results of the experimental measurements, these are compared with the ones given in the catalogue.

8.6.1 No load running torque

The no load running torque is defined as the torque needed on the high-velocity side of the harmonic drive to maintain the angular velocity rotation when no load torque is applied to the low-speed side of the harmonic drive. In the datasheets, measurements are available for four working velocities. The no load running torque is presented as a function of the ambient temperature. For this application, the temperature is assumed to be constant and of 25 [°C].

The values extracted from the datasheets are compared with the polynomial regression of the surface for negative and positive velocities, as represented in Table 11. The indicated velocities correspond to those of the motor, at the low-velocity side.

Velocity [rad/s]	Torque datasheets [Nm]	Torque exp,p [Nm]	Torque exp,n [Nm]
0.33	0.04	-0.04	0.034
0.65	0.06	-0.045	0.04
1.31	0.085	-0.05	0.05
2.29	0.095	-0.05	0.055

Table 11 – No load running torque

From this study, it can be graphically seen in Figure 51 that the torque prediction of the datasheets is always higher than the experimental measurements. The datasheet is overestimating the measured torque of the actual system. Indeed, the no load condition is never really met when the whole test bench is assembled. However, the increasing torque behaviour is respected. The values also stand in the same order of magnitude. The no load running torque data from the catalogue cannot be taken in consideration in this case.

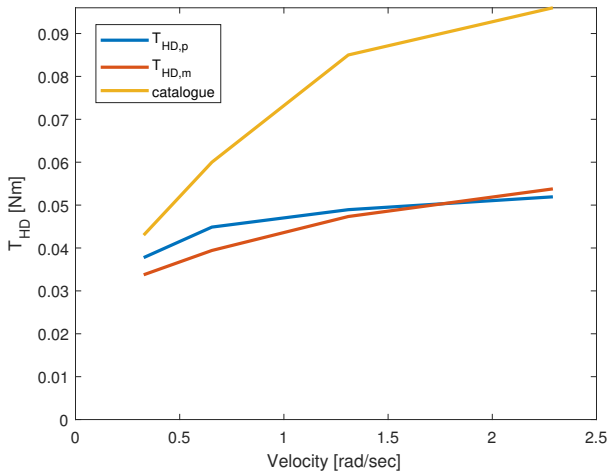

Figure 51 – No load running torque comparison

8.6.2 No load starting torque

The no load starting torque represents the torque needed at the high-velocity side to begin the rotation when no load is applied on the low-velocity side. In this case, only one data is

available concerning the harmonic drive in the catalogue. It corresponds to 0.22 [Nm] to start the harmonic drive rotation.

The experimental no load starting torque is manually evaluated by trial error tests. Torque is applied to the test motor without applying any load torque at the load motor. The experimental starting torque at the high-velocity side of the harmonic drive is then estimated to be of 0.04 [Nm]. To conclude, the experimental measurement and the value from the catalogue for the no load starting torque are even not of the same order of magnitude. The experimental operational conditions are too far from the datasheet ones. Once again, only the experimental measurements have to be taken into account.

8.6.3 No load back driving torque

The no load back driving torque can be defined as the torque needed at the low-velocity side of the harmonic drive to start the rotation of the low-velocity side of the harmonic drive when no load torque is applied on the high-velocity side. Indeed, this is the case of the application when the test motor is braking.

The value given in the datasheet is 42 [Nm]. However, it is specified in the catalogue that this approximated value is not applicable when a load torque is present at the high-velocity side of the harmonic drive.

The experimental no load back driving torque is evaluated using the same procedure as for the no load starting torque. The only difference is that the applied torques have to be inverted. Eventually, one gets an experimental no load back driving torque of 6.78 [Nm]. Once again, because there is a one order of difference between the experimental estimation and the value from the catalogue, the latter does not have to be taken into account for the test bench application.

8.6.4 Mechanical efficiency

One can also compare the mechanical efficiencies for accessible regions of the speed-torque characteristics. In the datasheets, the efficiency of the transmission through the harmonic drive depends heavily on the input velocity, load torque, ambient temperature and lubrication. To evaluate the mechanical efficiency, the first approximation is computed as a function of the temperature to which a compensation coefficient has to be applied as a function of the applied load torque.

By taking into account the assumptions of grease lubrication and of an ambient temperature of 25 [°C], one can get the efficiency only dependent of the temperature $\eta(T)$, for different velocity ranges, while the global mechanical efficiency as a function of the load is defined as

$$\eta(\tau, T) = \eta(T)K(\tau) \tag{67}$$

where K is the compensation coefficient. This value is determined thanks to the torque factor V, defined as

$$V(\tau) = \frac{\tau}{\tau_N} \tag{68}$$

where τ is the applied load torque while τ_N is the rated torque at rated speed. In the case of the harmonic drive, the rated torque is of $\tau_N = 28$ [Nm]. Unfortunately, no information is available for torque factors V under K values under 0.2, corresponding to a minimum load torque of around 6 [Nm]. In order to do a comparison, one can take load torque of 11, 7 and 6 [Nm] for the corresponding increasing velocities. The comparison between the experimental

and approximated values from the catalogue is represented in Figure 52. As it can be seen, the efficiency of the test bench matches closely with the ones of the datasheet.

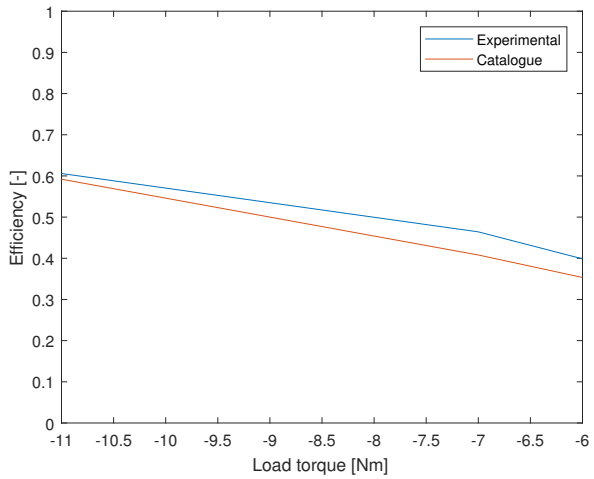

Figure 52 – Mechanical efficiency: comparison between the measurements and the catalogue

8.7 Dynamic evaluation

8.7.1 Mechanical performance

In this part, the tests are done dynamically with the direct actuation and the series elastic actuation. The human gait cycle is implemented and tested on the test bench. Once again, the PID controllers are experimentally tuned, and the results strongly depend on it. The perfect experimental tuning of the controllers is also difficult online, especially for the varying sign velocity stages. Hardware limitations also restrict proper manual tuning. The experimental parameters of the PID controllers used in this section are represented in Table 12. An estimation of the experimental power consumptions is performed. The results are compared in Section 9 where simulation is performed with an improved control tuning.

	Test motor	Load motor
k_p	2000	1
k_i	300	10
k_d	100	0.3

Table 12 – PID parameters

Contrary to the steady-state evaluation, an inertial term has to be added to the prediction of $\tau_{HD,ss}$. Indeed, in that case, the acceleration of the actuator has to be taken into consideration. The predicted τ_{HD} in the dynamical mode becomes

$$\tau_{HD} = \tau_{HD,ss} + (I_{Test} + I_{Load})\alpha \tag{69}$$

where α is the angular acceleration of the theoretical human gait knee angle. The computed torque losses by the harmonic drive is represented in Figures 53a and 53b, respectively. The contribution of the kinetic and potential energy rate are represented in Figure 53c.

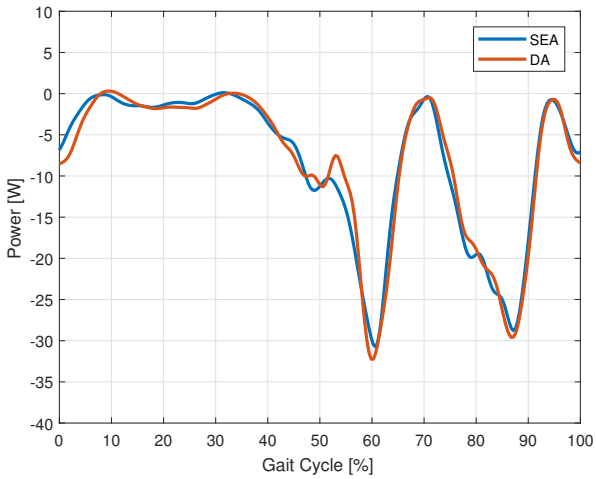

(a) Power of the harmonic drive P_{HD} evaluation

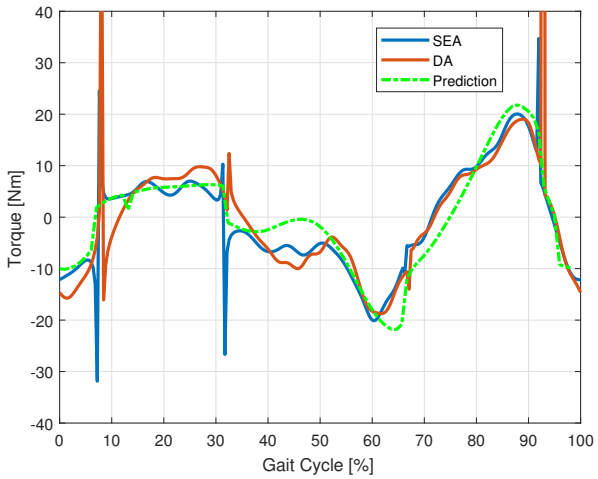

(b) Torque of the harmonic drive τ_{HD} evaluation

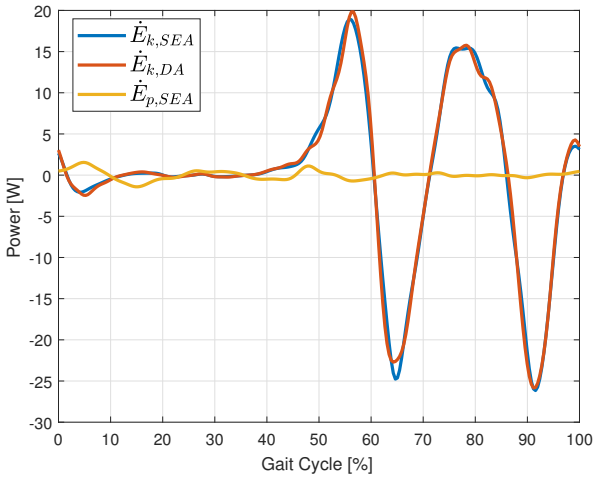

(c) Potential and kinetic energy rate

Figure 53 – Mechanical performances comparison between the direct actuator and the series elastic actuator

The prediction coming from the steady-state performance evaluation seems to be a rather good tool to predict the dynamic behaviour. As it can be seen, the differences between the series elastic actuator and the direct actuator are very small. The series elastic actuator allows a local decrease of P_{HD} and τ_{HD} during the stance phase of the gait cycle. The contribution of $\dot{E}_p$ is more present during the stance phase than during the swing phase. Indeed, during the stance phase, the foot is in contact with the ground. The compression of the spring can be seen as a shock absorber among others for heel strike sequence. $\dot{E}_p$ is in this gait application quite low. To get more advantages of the series elastic actuator from the power point of view, one should certainly low the stiffness of the current spring or improve the strengthening of the direct actuator which seems to be not perfectly rigid. It is comprised approximately between -1.5 [W] and 1.5 [W]. Concerning $\dot{E}_k$, the behaviour is also very similar for both actuators.

The global mechanical energy consumption of the harmonic drive, over the gait cycle time of 2.5 seconds, is deduced by integration of the corresponding mechanical power P_{HD} for the direct actuator and the series elastic actuator. The values are presented in Table 13 as well

as the potential and kinetic energy rates.

	E_{HD} [J]	E_k [J]	E_p [J]
SEA	-51.57	40.17	2.51
DA	-51.2	39.68	-

Table 13 – Power energy analysis of the harmonic drive between the series elastic actuator and the direct actuator

For the possible tested gait, it can be seen that energy lost through the harmonic drive by using the series elastic actuator and the direct actuator is very close.

Note also that a filtering is performed on the data. The velocity and acceleration signals are derivated from the cubic spline interpolation of the position signal to avoid the iterative addition of numerical errors. The torque measurements are used after a low-pass filtering of its power spectral content.

8.7.2 Electrical performance

The electrical global energy consumption of the actuators over the gait cycle is deduced from the integration of the corresponding mechanical power of the test motor and the electrical input power delivered by the power supply and the driver to the motor. The electrical power of the motors is defined as

$$P_{el} = VI \tag{70}$$

where V is the voltage of the power supply and I, the current injected into it. The mechanical power associated to the test motor is computed as

$$P_{mec} = V_{Test}\tau_{Test} \tag{71}$$

where V_{Test} is the test motor velocity, τ_{Test} is the mechanical measured torque. The power consumptions are represented in Figure 54. Numerically, the energy consumptions are computed as presented in Table 14.

	Mechanical Energy [J]	Electrical Energy [J]
SEA	64.76	169.86
DA	64.18	168.57

Table 14 – Electrical consumption of the SEA and DA

During the swing phase, the actuators have an increasing velocity up to the first power peak. The power then decreases due to a reduction in speed variations and applied load torque down to 0 [Nm] which corresponds to the maximum amplitude of the knee angle during the gait cycle. At this point there is no load applied because the foot is no more in contact with the ground, the test motor then has to brake and absorbs power. Concerning the second power peak, the applied load torque increases while the test motor has to accelerate again to reach the desired velocity. After the second power peak, the velocity of the knee joint is decreasing down to zero to start the stance phase again.

The use of a series elastic actuator does not experimentally allow a power reduction consumption over the whole gait cycle. On the other hand, again, the mechanical power is locally little reduced during the stance phase, where the spring is the most compressed. The series elastic actuator is certainly improving the safety of the human-orthosis interaction and its comfort. However, this effect is limited in the measurements. The results are also depending on the quality of the control. Therefore, the development of a simulation tool is prescribed.

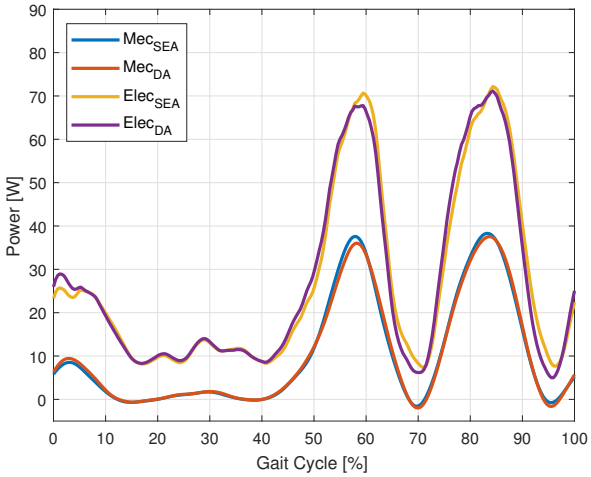

Figure 54 – Mechanical and electrical power associated to the test motor

Concerning the electrical efficiency, it can be deduced that is the best during the swing phase of the gait cycle, namely with low applied load torque and high knee angle variation. It is reaching efficiencies up to almost 0.5, for both actuators.

8.8 Clutchable series elastic actuator

In this section, the necessity of the electromagnetic clutch is evaluated. Two different types of tests are done in this section. The first test consists in evaluating the power consumption of the electromagnetic brake and to compare it with the one required by the test motor to brake and hold a permanent position, whatever the applied torque is. The braking electrical power is measured for the clutch as well as for the test motor. For this experiment, the load motor is manually deflected over the maximum torque ranges [-20; 20] [Nm] allowed on the test bench, as represented in Figure 55a. The electrical power is computed thanks to the current sensor and the voltage divider. The electrical power consumptions of the clutch and of the test motor while braking to keep the same angular position are represented in Figure 55b.

Note that a continuous electrical offset consumption of 7 [W] from the hardware has to be removed from the measurements to deduce the electrical supply needed by the clutch. As it can be seen, the electrical consumption of the electromagnetic clutch is constant all over the braking time. Its magnitude is close to 6 [W] while the power consumption of the test motor is varying during braking. At the beginning of the braking, the electrical consumption jumps up to 10 [W]. The electrical power decreases then close to 0 [W] when the load torque is again decreasing down to 0 [Nm]. For negative applied load torque, the electrical power consumption also goes up to 10 [W] on the way to the minimum load torque while it is consuming back 0 [W] for increasing load torques up to 0 [Nm]. The electrical braking power is in phase with the braking torque measured by the load cell. In this case, the clutch braking is using almost 12% more electrical power than the motor braking.

The use of an electromagnetic brake may be electrically more efficient in the case of the application of high load torque with high variations. During the stance phase of the gait cycle, the torque is supposed to be large compared to the swing phase, and the electrical consumption is expected to be lower by braking with the clutch.

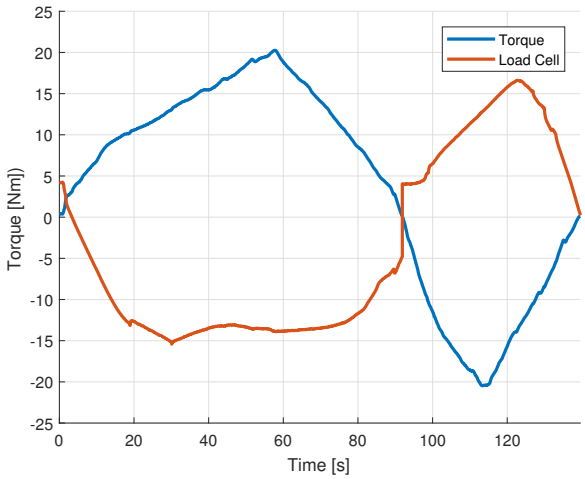

(a) External manually applied torque and the torque read by the load cell

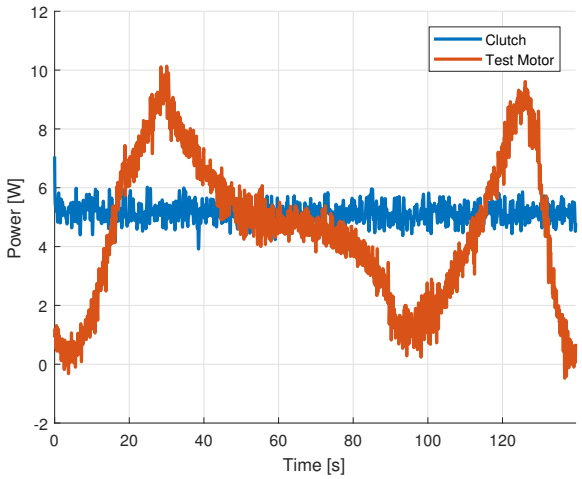

(b) Electrical power consumption of the clutch and the test motor when braking

Figure 55 – Comparison between clutch braking and motor braking

The second performed test is the mechanical and electrical power evaluation of the series elastic actuator with and without the use of the clutch during the stance phase. Note that here, the electromagnetic clutch is activated for the low angle variations, as it can be seen in Figure 56a. This period is a bit more extended than the stance phase only. However, in this section, for some hardware limitations coming from the drivers, it is not possible to use the initial gait cycle of the previous parts. Indeed, in practice it is not possible to put as much load torque as needed to expect to see the effectiveness of the clutch. Furthermore, the system is in this case way harder to control because when braking or removing the brake all the power flow of the system is highly perturbed. A compromise found to evaluate the effectiveness of the clutch over the gait cycle has been made by reducing the knee angle down to a maximum amplitude of 50 [°] during the swing phase, while the applied load torque is still of 9 [Nm]. For higher amplitudes of knee angle deflection or load torques, the drivers are not able to absorb the braking power and shut up in their safety modes. The controller used in this section is the impedance controller as described in section 6.2.3. Its deep description is not part of the thesis. The simulation of the clutchable series elastic actuator is done by using a PID controller as detailed in Section 9.4.2.

In Figure 56a, the position tracking is respected compared to the desired position signal for the series elastic actuator with and without the use of the clutch. Concerning the mechanical and electrical power consumption in Figure 56b, several observations can be done.

- Braking time
  1. SEA: The test motor has to brake because of the low position variations and relatively high applied load torque. Electrical and mechanical power are then negative when energy is absorbed and positive when energy is provided to the system.
  2. CSEA: The mechanical power consumption becomes null due to the electromagnetic clutch which provides all the electrical power needed to hold the position of the test motor. The electrical power consumption is also mostly constant during all the braking time.
- Non braking time
  1. SEA: Two power peaks are met. The test motor is driving the shaft and has to accelerate to reach the desired velocity.
  2. CSEA: The same kind of behaviour is met without the use of a clutch. Only one main

difference is discussed. When dislocking the joint, the test motor has to accelerate quicker to reach the desired position at the corresponding right time. Indeed, the mechanical power was null when locked.

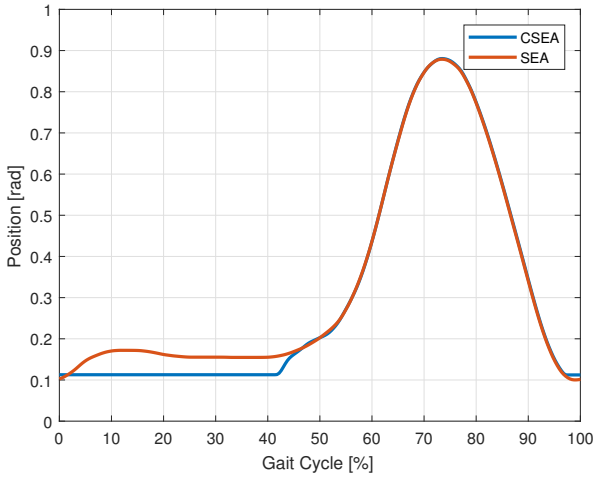

(a) Position tracking in the case of the SEA with and without clutch

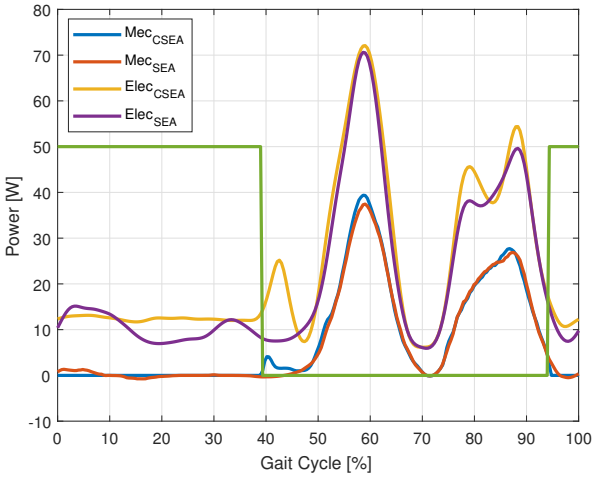

(b) Power consumption in the case of the SEA with and without clutch. The green line is the activation signal of the clutch equals to 1 when activated and to 0 when deactivated. For the clearness of the graph, this last is multiplied by 50.

Figure 56 – Clutchable series elastic actuator and series elastic actuator evaluation

The energy consumptions per gait cycle of 2.5 seconds are shown in Table 15.

	Mechanical Energy [J]	Electrical Energy [J]
CSEA	49.49	146.32
SEA	47.43	129.51

Table 15 – Mechanical and electrical consumption of the series actuator with and without clutch

The locking of the system thanks to the electromagnetic clutch requires still a continuous electrical power of 6 [W] (in addition to the 7 [W] of continuous hardware consumption). The knee joint is locked half of the gait cycle which lasts 2.5 [s] in this case. Numerically, it represents almost an electrical energy of 7.5 [J]. In this particular case, it can be seen that the use of the locking system with a clutch has a larger energetic cost than following the normal gait cycle behaviour. Indeed, one needs almost 15 [J] more when braking with the electromagnetic clutch. The electrical efficiency is also worse. However, at a point when the gait cycle should be faster, the applied load torque higher or the control improved, the use of the clutch may be justified. However, this is experimentally not verifiable in the current case due to test bench hardware limitations.

9 Simulation and validity

In this section, an electro-mechanical simulation of the test bench has been implemented on *Simulink*. This implementation enables to to tune more precisely the controllers and validate the general parameters employed in the model for the current application.

9.1 Model strategy

The model of the test bench consists in controlling two DC motors. Since the two motors are coupled, a position or velocity controller is used to track the desired trajectory of the test motor while a torque controller is supposed to track the load disturbance induced by the load motor on the test motor.

The controllers used in the simulation are all PIDs. In order to control the system properly, the controller has to fulfill some requirements. It has to be robust because of the necessary safety conditions to ensure to the subjects. It also has to be fast reacting due to the big and rapid variations in angle, speed and stiffness required by a human knee during gait. The supplied current also has to be contained in the ranges of application of the motors and their drivers.

The construction of the model is done thanks to a *down-top* method with validation step by step of the subparts, before assembling all the components together.

9.2 DC motor

To model a DC motor, both electrical and mechanical equations have to be developed and properly combined. In control theory, the system is presented in the Laplace domain, and it consists in the arrangement of the transfer functions composing the system.

The transfer function of the armature part of the DC motor is developed thanks to the equations developed in Section 54, as

$$V(t) = R\,i(t) + L\,\frac{di(t)}{dt} + K_e\,\frac{d\theta(t)}{dt} \tag{72}$$

Let us apply the Laplace transform and express this equation in terms of the Laplace variable s. The last equation becomes,

$$\begin{aligned} V(s) &= R\,i(s) + L\,s\,i(s) + K_e\,s\,\theta(s) \\ &= R\,i(s) + L\,s\,i(s) + e(s) \\ &= i(s)\ (L\,s + R) + e(s), \end{aligned} \tag{73}$$

where e is the back electromotive force. In such case, the electrical transfer function can be expressed as the ratio between the current and the voltage applied to the motor, so that

$$\frac{i(s)}{V(s) - e(s)} = \frac{1}{L\,s + R} \tag{74}$$

This transfer function gets as input the difference between the input voltage and the back electromotive force and has the armature current as output. However, torque and current are proportionally related by $T(t) = K_m\,i(t)$. Therefore, the transfer function of the armature part becomes

$$H_{el}(s) = \frac{T(s)}{V(s) - e(s)} = \frac{K_m}{L\,s + R} \tag{75}$$

The general representation of the test bench has to include the combination of Equation 75 to the contribution of the mechanical transfer functions developed in Section 5.5. As an example, the ratio between the output mechanical angular speed of a motor and its input voltage, is computed as the product of the electrical and mechanical transfer functions, as

$$H_{global}(s) = \frac{\omega(s)}{V(s)} = H_{el}(s) \cdot H_{mec}(s) \tag{76}$$

The general representation of an open-loop DC motor in *Simulink* is available in Figure 57. The figure is an image of the electrical and mechanical relationship in the DC motor. The values of the parameters used are experimentally identified in Section 7. A current saturation block is also introduced to characterise the electrical limitations of the components supplying the motor.

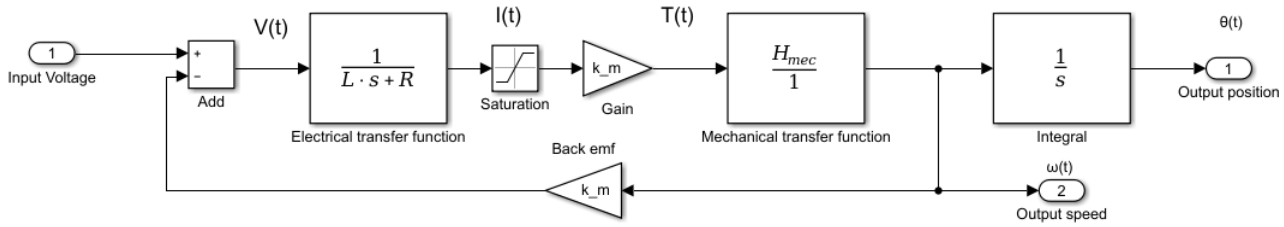

Figure 57 – System representation of a general DC motor

9.3 Test bench

In this subsection, the construction of the model, its control and the generated restuls of the test are discussed.

9.3.1 Friction torque

As detailed in the previous sections, the viscous friction torque represents the damping of the mechanical transfer functions and has not to be applied again on the model as a torque disturbance. However, the non-linearity induced by the static friction torque has to be deducted of the output torque of the motor, depending on the sign of the velocity. In this way, the static friction torque is computed as represented in Figure 58.

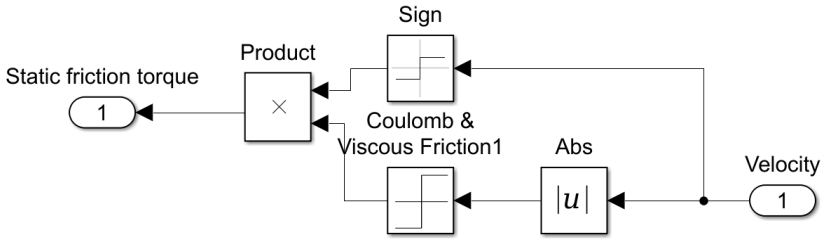

Figure 58 – Static friction torque model

9.3.2 Electromagnetic clutch

The electromagnetic clutch can be added to the system. Because the knee joint is supposed to be commanded to repeat the same sequence, the electromagnetic clutch is activated based on the time progress through the gait cycle. However, it can also be possible to do it based on the angular velocity or position of the motor for more practical and adaptive use.

The generated friction torque has to act in the opposite direction of the sign of the motor velocity. If the command signal to brake is activated, a friction torque of 0.75 [Nm] is produced to brake the system. The activation of the command signal to brake is equal to 1, and deactivated when the command signal is equal to 0. The clutch is located downstream of the harmonic drive so that the resulting torque has to be multiplied by the gear ratio i_{HD}. The general model of the electromagnetic clutch is represented in Figure 59.

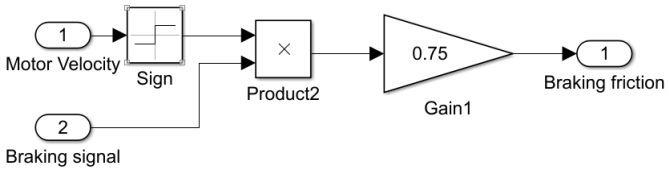

Figure 59 – Electromagnetic clutch model

The general representation of the assembled elements of the test bench is available in Figure 65 in Appendix.

9.3.3 Control

Depending on the tests, the test motor is controlled either by velocity when evaluating it in steady-state mode, while a position control is used for dynamic analysis of the system. Mathematically, the velocity is the derivative of the position, and the controller design is similar. For this reason, only the position controller is discussed in this section. A typical PID position controller is presented as in Figure 60.

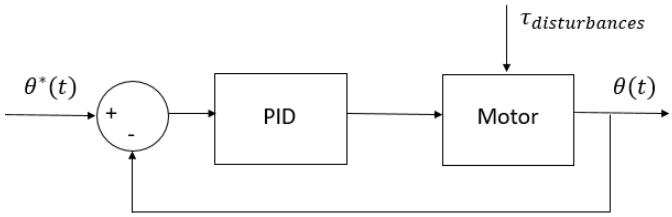

Figure 60 – Position control loop representation

The desired position trajectory is the input reference of the system. The controller takes as input the error between the reference position and the measured one. The output signal of the PID controller is then passing through the internal electrical armature of the motor to compute the torque. The torque is then transformed thanks to the mechanical transfer functions into the resulting measured position. A torque disturbance has also to be included to introduce all the disturbances of the surrounding environment which can interfere with the system.

The load motor is controlled in torque. However, from a physical point a view, the torque is directly proportional to the current in the armature of the motor. For this reason, a current controller is usually implemented. When controlling the current, it may be advisable to only use a PI controller because of the high-frequency signals that may disturb the system. A typical PID current controller can be presented as in Figure 61.

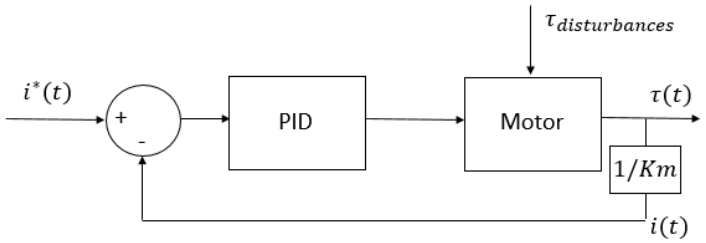

Figure 61 – Current control loop representation

In order to tune k_p, k_i and k_d, namely the proportional, integrative and derivative parameters of the PID controller, different methods exist:

1. Experimental: A rough estimation of the parameters can be found based on the controller requirements. However, finding the optimal values is very difficult. It is even more the case due to the inevitable differences between the practical test bench and the theoretical simulation.

2. Graphical: Some graphical tools can help to manually tune the parameters, as the Root Locus Method or thanks to the Bode and Nyquist plot analysis.

3. Numerical: Some numerical methods have been developed to tune the parameters as automatically as possible. Some examples are the Ziegler–Nichols method, the magnitude optimum method or the symmetrical optimum method. On the other hand, the numerical methods may be quickly limited depending on the applications.

However, since the two motors are strongly coupled and their control is in cascade configurations and working at the same range of frequency, the numerical methods are usually not sufficient. Based on the previous experimental controllers parameters, it is eventually chosen to refine manually the tuning of the controller, after implementing the Ziegler-Nichols method. The goal is to reach the most acceptable controller as possible. Controllers are firstly tuned regarding the responses of the system to a step reference signal, before applying the gait characteristics.

9.4 Results

On one hand, in this section the mechanical and electrical experimental and simulated powers are compared. Concerning the electrical performances, because the experimental voltage supply is measured based on an external sensor of the system, the voltage is not simulated. However, the voltage supply signal is always lightly oscillating around 24 [V] in practice. Note that in order to validate the model, the references imposed at both motors were firstly the experimentally measured signals. After this, the theoretical references are introduced in the system. The model is only valid for the current gait application assumptions. Small differences between the theoretical model and the test bench are expected, due to the previous assumptions. All the non-linearities such as position dependency, varying friction or hysteresis effect are also not introduced in the system. For some extensions, the physical parameters of the model have to be modified.

9.4.1 Direct actuator and series elastic actuator comparison

The simulation between the direct actuator and the series elastic actuator in terms of trajectory tracking is represented in Figure 62a for the test motor while the trajectory of the load motor is

represented in Figure 62b. The parameters of the controllers are presented in Table 16.

	Experimental		DA		SEA	
	Test motor	Load motor	Test motor	Load motor	Test motor	Load motor
k_p	2000	1	6300	100	6210	100
k_i	300	10	0.22	1	0.19	1
k_d	100	0.3	0.05	0	0.045	0

Table 16 – SEA and DA controllers comparison

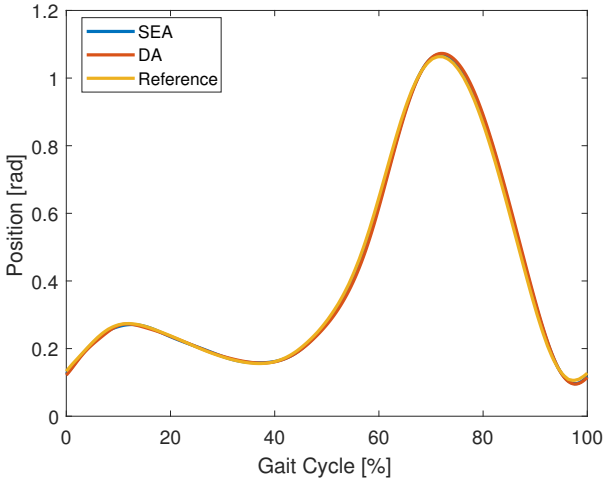

(a) Test motor trajectory

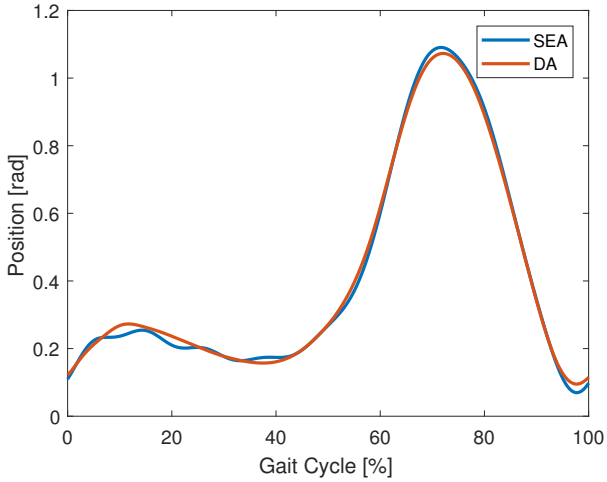

(b) Load motor trajectory

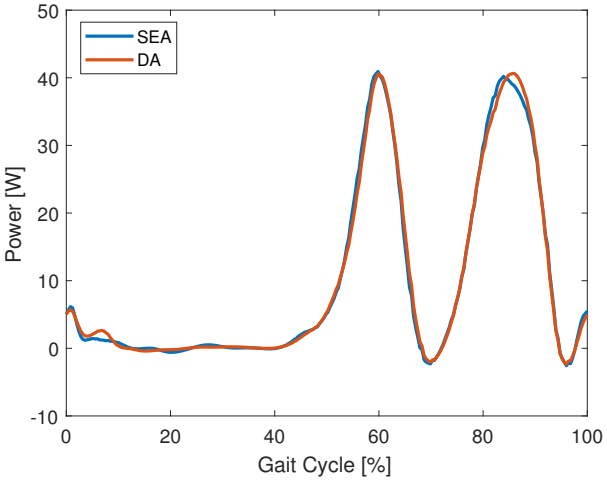

(c) Mechanical power consumption

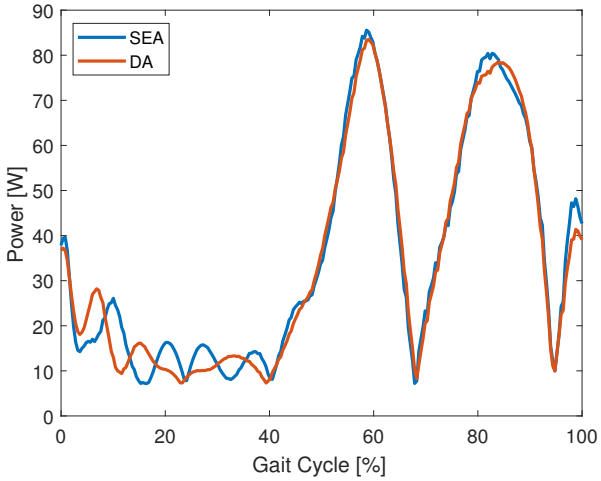

(d) Electrical power consumption

Figure 62 – DA and SEA comparison

The test motor tracking is well respected thanks to the good control. Concerning the series elastic actuator, it can be seen that the position difference between the position of the motors is bigger in the case of the series elastic actuator when varying the direction of the velocity. Indeed, at these stages of the gait cycle, the springs are compressed, potential energy is stored in it, and a position delay occurs between each shaft on both sides of the elastic part.

Concerning the mechanical power consumption, this is represented in Figure 62c. As it was seen in Section 8.7.1, the differences between the direct actuator and the series elastic actuator were very small. The results are well corresponding to the experimental measurements.

The tuning of the new controller is reinforcing the tracking but more torque has to be provided by the test motor to respect the reference signals. The predictions of the energy consumptions are presented in Table 17. The continuous consumption of the 7 [W] is also included in the electrical power simulation.

	Mechanical Energy [J]	Electrical Energy [J]
SEA	75.64	181.23
DA	74.78	180.95

Table 17 – Power consumption of the SEA and DA comparison

In this kind of application, the use of a series elastic actuator may be justified by a general decrease in mechanical power during the stance phase of the gait cycle during which the knee may be less loaded due to energy storage in the spring. However, to enjoy the power benefice of the addition of the springs to the actuation system, the user could accept to reduce the reliability of the control as it was tested experimentally.

9.4.2 Series elastic actuator and clutchable series elastic actuator comparison

The electromagnetic clutch that can allow a locking of the actuation system during small position variations is also added to the system. The experimental control is an impedance controller while in the simulation, a PID controller is implemented. The same gait scaled gait is used than experimentally. The position tracking and the mechanical and electrical power consumption are represented in Figures 63a, 63b and 63c, respectively. The parameters of the controller are presented in Table 18.

	Simulation	
	Test motor	Load motor
k_p	6210	100
k_i	0.27	1
k_d	0	0

Table 18 – CSEA and DA controllers comparison

Compared to the experimental measurements, the tracking is improved. In this way, the simulation allows to extend the measurements. It can be computed that in this case the clutch is more electrically efficient than it was tested in practice as it can be seen in Table 19.

	Mechanical Energy [J]	Electrical Energy [J]
CSEA	50.63	151.06
SEA	49.7	160.69

Table 19 – Power consumption of the CSEA and SEA

It is important to note that the simulation part of the thesis was performed after leaving the traineeship at *Universitat Politècnica de Cataluyna* and the new computed controllers have not been tested on the actual test bench.

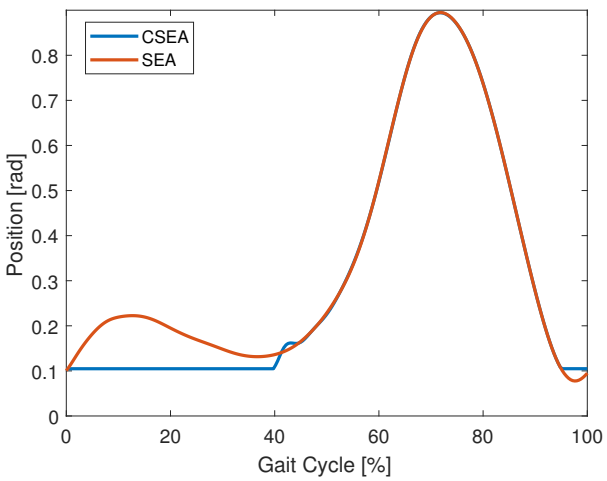

(a) Test motor trajectory

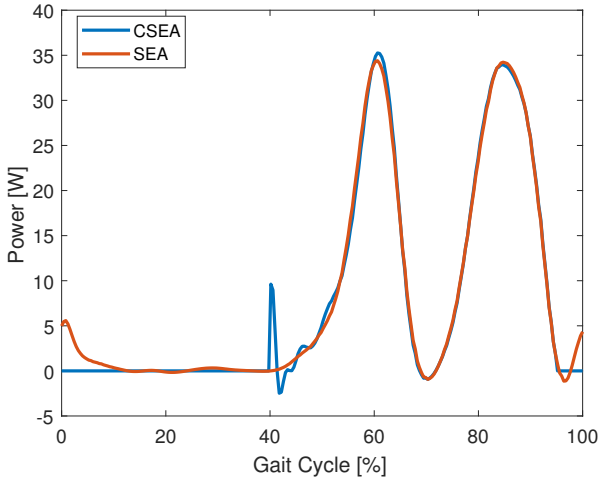

(b) Mechanical power consumption

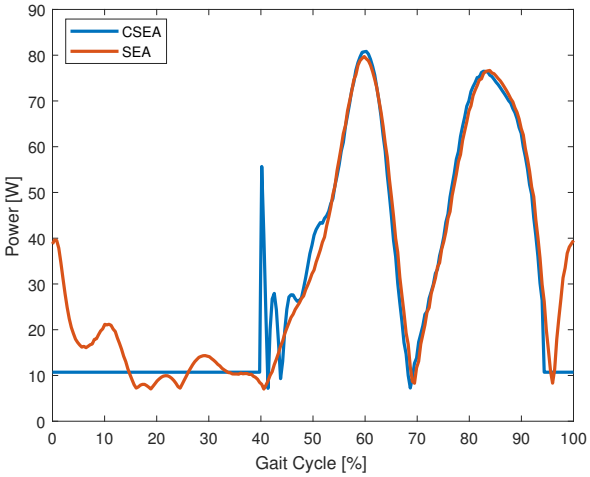

(c) Electrical power consumption

Figure 63 – SEA and CSEA comparison

10 Engineering cost and planning

10.1 Engineering Cost

The main costs are due to the engineering working hours done to realise the current master thesis. The engineering cost is calculated based on an estimation of around 900 hours of work done by a junior engineer as well as a supervision of a senior engineer, estimated around 100 hours of work.

All the test bench was already mounted and manufactured before beginning the master thesis. The test bench is estimated to have a value of €7000 on itself, including the cost of the purchase of the different components as well as the manufacturing costs. The electrical consumption of the computers as well as the electrical supply of the test bench are hard to estimate and will not be taken into account in this approximation.

Title	Amount [h]	Unit Price	Total [€]	
Junior Engineering	900	30 €/h	27000 €	
Senior Engineering	100	50 €/h	5000 €	
			32000 €	TOTAL

10.2 GANTT diagram

The GANTT diagram is an organisational tool to plan the tasks that have to be successively done as well as the time prediction and limits to execute them. At several times, the objectives of the work had to be redetermined during the trainee session caused by some experimental constraints. This is totally normal in engineering research when dealing with experimental work. The GANTT diagram is presented in Figure 64.

Figure 64 – GANTT diagram

11 Conclusion

In the framework of this work, an evaluation of a test bench designed for knee actuator systems has been conducted.

Firstly, the knee requirements, as well as the characteristics of human gait, have been studied. It was concluded that a human knee experiences significant variations of position and speed during gait. Its physiological stiffness is also varying over time, it has to be rigid during the stance phase, and the knee must be able to move almost freely during the swing phase of the gait cycle.

In order to be compatible with the physiological requirements, three actuators are tested. These are the direct actuator, the series elastic actuator and the clutchable series elastic actuator.

The limitations of the current test bench regarding electronics and mechanics have been evaluated to determine the experimental procedure. It is concluded that the system can only support very low gait of light subjects at this current stage.

First of all, to extract reliable measurements on the test bench, the sensors have to be properly calibrated. Secondly, the physical parameters influencing the dynamics of the system have been experimentally determined. These were the stiffness, the inertia and friction. The inertia and stiffness were considered as constant for each configuration while the friction torques were depending on the magnitude and frequency of the applied torques and velocities.

The performances of the system are evaluated by comparison of the series elastic actuator and the direct actuator through experimental tests and the development of an electro-mechanical simulation. An energy balance analysis of the system is performed and the power consumptions are evaluated. The results strongly depend on the tuning of the control systems.

Experimentally, hardware limitations restrict the extension of the tests and the tracking capabilities of the system. The results found experimentally and by simulation tend to the same conclusions. The power consumptions of both actuators are very similar. However, during the stance phase, the spring is able to lower the mechanical power consumption thanks to energy storage, even if that effect is quite limited. This might increase the comfort of the user as well as its safety. The power consumption also depends on how accurate the control system has to be.

On the other hand, the braking advantages of the clutch during the stance phase are evaluated in the case of the series elastic actuator. We can see through simulation that the addition of the electromagnetic clutch allows an electrical power consumption reduction with proper control tuning. Experimentally, the clutch may also be useful with some extensions of the constraints by implementing the test bench with more powerful drivers and motors.

To conclude, a first approximation of the capabilities of the test bench has been evaluated. Depending on the desired tests, the hardware could be improved as a further work. A replacement of the harmonic drive by a more linear gear box could also be an improvement. The stiffness of the spring should be a bit reduced to get more power advantages of the elastic actuation. Through strong experimental control design, the actuator could be firstly tested on healthy subjects, and then on unhealthy subjects when the experiments and safety purposes are validated.

Appendices

A General *Simulink* model representation

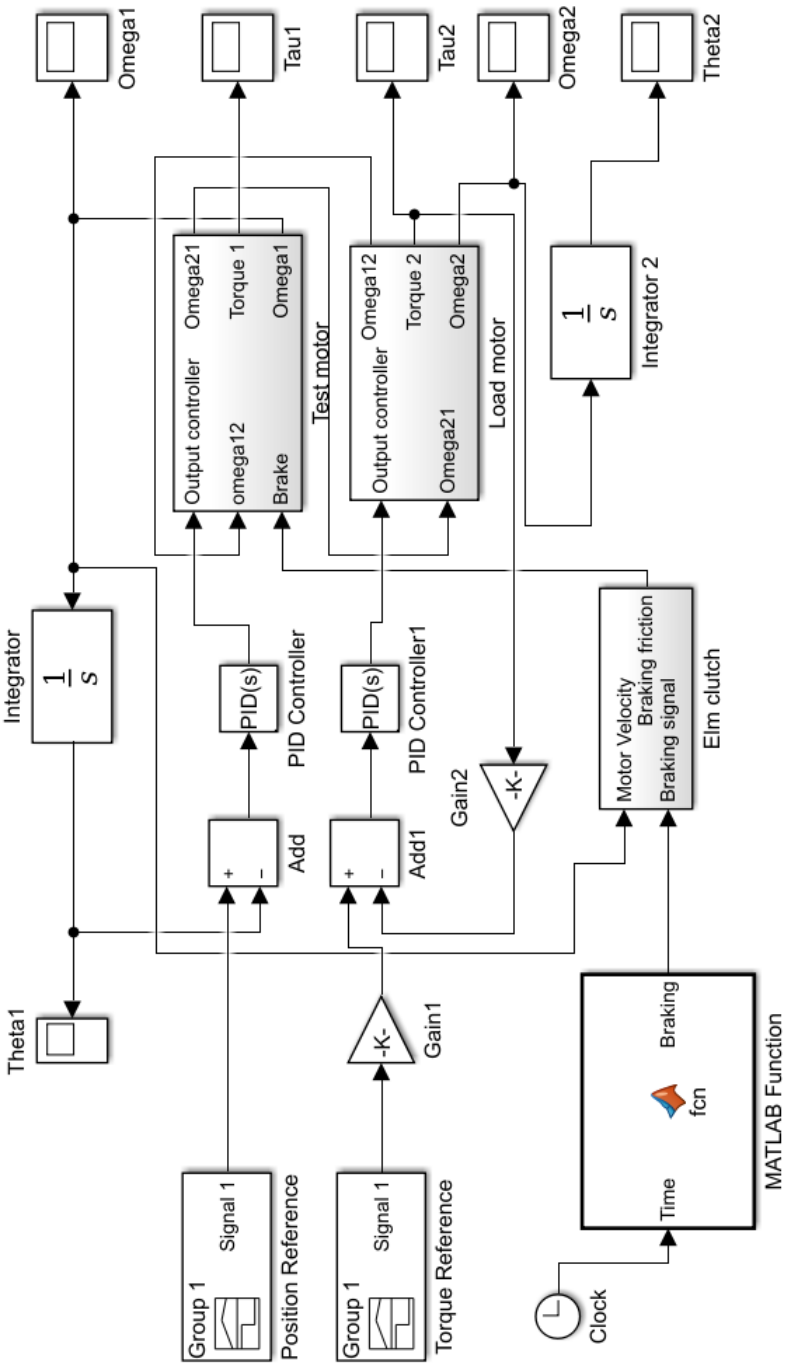

Figure 65 – Global model of the test bench implemented in *Simulink*

B Scaled gait data

	Angle	Torque		Angle	Torque
a_0	0.3884	-0.1507	ω	2π	2π
a_1	-0.07603	-0.221	b_1	-0.326	-0.3977
a_2	-0.1943	0.04218	b_2	0.1141	-0.9473
a_3	0.008267	0.4108	b_3	0.07186	0.03786
a_4	-0.001994	0.01918	b_4	0.005746	-0.1118
a_5	-0.004342	0.09149	b_5	0.01286	0.06741
a_6	0.003985	0.002324	b_6	0.002147	-0.01246
a_7	-0.0005321	0.002467	b_7	0.0009002	0.01965
a_8	0.001249	0.006651	b_8	0.0008244	0.004735

Table 20 – Torque-speed characteristics of the human gait fitting parameters values

C Steady-state τ_{HD} surface's parameters

	Positive speed	Negative speed		Positive speed	Negative speed
p_{00}	-3.218	3.307	p_{31}	0.0001224	-0.0009243
p_{10}	0.01472	0.02794	p_{22}	0.01372	-0.00336
p_{01}	-12.64	-9.783	p_{13}	0.05384	-0.05656
p_{20}	-0.00751	0.00712	p_{04}	2.726	-4.223
p_{11}	-0.1193	0.08683	p_{50}	2.842e-06	-1.666e-06
p_{02}	14.97	-13.52	p_{41}	0.0001339	4.649e-05
p_{30}	-0.0003623	-0.0002042	p_{32}	-0.0006464	-0.0001567
p_{21}	-0.0444	-0.02946	p_{23}	-0.0004289	-0.0006695
p_{12}	0.02536	-0.002438	p_{14}	-0.01816	-0.0147
p_{03}	-9.145	-11.03	p_{05}	-0.3143	-0.595
p_{40}	3.208e-05	-3.222e-05	-	-	-

Table 21 – Steady-state τ_{HD} surface's parameters for positive and negative speeds

References

[1] Makoto Kaneko and Yoshihiko Nakaruma (Eds.) (2010)*Robotics Research, the 13th International Sympposium ISRR*, Springer

[2] I. Diaz, J. J. Gil, and E. Sanchèz, "Lower-limb robotic rehabilitation: literature review and challenges", *Journal of Robotics*, November 2011.

[3] G. Bovi, M. Rabuffetti, P. Mazzoleni, and M. Ferrarin, "A multiple-task gait analysis approach: kinematic, kinetic and emg reference data for healthy young and adult subject," *Gait Posture*, vol. 33, no. 1, pp. 6-13, 2011.

[4] S. Mohammed, W. Huo, H. Rifaï, W. Hassani, and Y. Amira, "Robust Control of an Actuated Orthosis for Lower Limb Movement Restoration," *Intelligent Assistive Robotcs, Recent Advances in Assistive Robotics for Everyday Activities*, pp.385-400, 2015.

[5] K. Kong, J. Bae, M. Tomizuka,"Mechatronic Considerations for Actuation of Human Assistive Wearable Robotics: Robust Control of a Series Elastic Actuator,"' *Intelligent Assistive Robotcs, Recent Advances in Assistive Robotics for Everyday Activities*, pp.400-430, 2015.

[6] K. H. Low," Recent Development and Trends of Clinical-Based Gait Rehabilitation Robots," *Intelligent Assistive Robotics, Recent Advances in Assistive Robotics for Everyday Activities*, pp.41-76, 2015.

[7] L. Liu, S. Leonhardt, and B. J. E. Misgeld, "Design and control of a mechanical rotary variable impendance actuator,"*ScienceDirect/Mechatronics (39)*, pp. 226-236, November 2016.

[8] M. Laffranchi, L. Chen, N. Kashiri, J. Lee, N. G. Tsagarakis, and D. G. Caldwell," Developement and control of a series elastic actuator equipped with a semi active friction damper for human friendly robots,"*ScienceDirect/Robotics and Autonomous Systems (62)*, pp. 1827-1836, 2014.

[9] G. Chen, P. Qi, Z. Guo, and H. Yu, "Mechanical design and evalutation of a compact portable knee-ankle-foot robot for gait rehabilitation", *ScienceDirect/Mechanism and Machine Theory (103)*, pp. 51-64, 2016.

[10] K. D. Kaya and L Cetin, "Adaptive state feedback controller design for a rotary series elastic actuator",*Transactions of the Institute of Measurement and Control*, Vol. 39(1), pp. 61–74, 2017

[11] C. L. Vaughan, B. L. Davis, and J. C. O'Connor, "Gait Analysis Laboratory (2nd edition)", 1999.

[12] F. Stuhlenmiller, "Design of an Elastic Actuation System for a Gait-Assistive Active Orthosis for Incomplete Spinal Cord Injured Subjects," Master's thesis, Technische Universität Darmstadt and Universitat Politècnica de Cataluyna, 2016.

[13] D. Callejo Goena, "Design of a test bench to evaluate the dynamic performance of the actuation system of an active knee-ankle-foot orthosis," Master's thesis, Escloa Tècnica Superior d'Enginyera Industrial de Barcelona, 2014.

[14] F. Tian, M. Samir Hefzy, and M Elahinia, "State of the Art Review of Knee–Ankle–Foot Orthoses," *Annals of Biomedical Engineering*, Vol. 43, No. 2, pp. 427–44, February 2015.

[15] W. M. dos Santos and A. A. G. Siqueira, "Impedance Control of a Rotary Series Elastic Actuator for Knee Rehabilitation," *Proceedings of the 19th World Congress The International Federation of Automatic Control*, Cape Town, South Africa, August 24-29 2014.

[16] M. Cestari, D. Sanz-Merodio, J. C. Arevalo, and E. Garcia, "An Adjustable Compliant Joint for Lower-Limb Exoskeleton," 2015.

[17] A. M. Dollar and Hugh Herr, "Lower Extremity Exoskeletons and Active Orthoses: Challenges and State-of-the-Art," *IEEE Transaction on robotics* , Vol. 24, No. 1, February 2008.

[18] T. Yan, M. Cempini, C. M. Oddo, and N. Vitello, "Review of Assistive Strategies in Powered Lower-Limb Orthoses and Exoskeletons," September 7, 2014.

[19] S. Thapa, "Development of Robotic Lower-Limb Prothestic and Orthotic Devices," Master's thesis, University of Alabama, 2015.

[20] S. Rossi, F Patanè, F. Del Sette, and P. Cappa, "WAKE-up: a Wearable Ankle Knee Exoskeleton," *IEEE RAS and BioRob*, August 12-15, 2014.

[21] I.R. Muhammad and A. O. Noor Azuan, "Stance-Control Orthoses with Electromechanical Acutation Mechanism: Usefulness, Design Analysis and Directions to Overcome Challenges," *Journal of Neurology and Neuroscience*, vol 6, No 3:49, 2015.

[22] P. Beyl, K. Knaepen, S. Duerinck, M. Van Damme B. Vanderborght, R. Meeusen, and D. Lefeber,"Safe and Compliant Guidance by a Powered Knee Exoskeleton for Robot-Assisted Rehabilitation of Gait," *Advanced Robotics* 25:5, 513-535, DOI: 10.1163/016918611X558225, 2011.

[23] E. Garcia, D. Sanz-Merodio, M. Cestari, M. Perez, and J. Sancho, "An Active Knee Orthosis for the Physical Therapy of Neurological Disorders," *Advances in Intelligent Systems and Computing (AISC)*, Vol. 418, DOI: 10.1007/978-3-319-27149-1-26, 2015.

[24] J. M. Font-Llagunes, R. Pàmies-Vilà, J. Alonso, and U. Lugrí, "Simulation and design of an active orthosis for an incomplete spinal cord injured subject," *ScienceDirect Procedia IUTAM*, Volume 2, pp. 68-81, 2011.

[25] V. R. Ham, T. G. Sugar, B. Vanderborght, K. W. Hollander, D. Lefeber,"Compliant actuator designs: Review of actuators with passive adjustable compliance/controllable stiffness for robotic applications," *IEEE Robotics and Automation Magazine*, Vol. 16, pp. 81-94, 2009.

[26] S. Iyer, "Modeling and Testing of a Series Elastic Actuator with Controllable Damping", Master's thesis, WORCESTER POLYTECHNIC INSTITUTE, 2012.

[27] D.W. Robinson, G.A. Pratt, "Force controllable hydro-elastic actuator," *IEEE Robotics and Automation*, DOI: 10.1109/ROBOT.2000.844781, 2000.

[28] D.W. Robinson, G.A. Pratt, "Series elastic actuators," *IEEE Intelligent Robots and Systems*, DOI: 10.1109/IROS.1995.525827, 1995.

[29] H. Uustal and E. Baerga" *Physical Medicine and Rehabilitation Board Review Demos Medical* New York, NY, USA, 2004.

[30] A. L. S. Barbosa, G. Acioli Junior, and P. R. Barros *symmetrical optimum based PI control redesign* Anais do XX Congresso Brasileiro de Automática Belo Horizonte, MG, 20 a 24 de Setembro de 2014

[31] T. Verstraten, G. Mathijssen, R. Furnémont, B. Vanderborght, and D. Lefeber, "Modeling and design of geared DC motors for energy efficiency: Comparison between theory and experiments," *Mechatronics, Elsevier, September 2015*

[32] P.-J. Cheng, and H.-P. Huang "Model Matching Control for an Active-Passive Variable Stiffness Actuator,"*Mechatronics, Elsevier, September 2015*

[33] Shamaei K., Napolitano PC., and Dollar AM. "Design and functional evaluation of a quasi-passive compliant stance control knee-ankle-foot orthosis."*IEEE Trans Neural Syst Rehabil Eng. 2014 Mar;22(2):258-68. doi: 10.1109/TNSRE.2014.2305664*

[34] T. Kikuchi J. K. Oda "Development of a 6-DOF Rehabilitation Robot and its Software for Clinical Evaluation Based on Virtual Reality"*Conference Paper · Jun 2007*

[35] K. Kong, J. Bae, and M. Tomizuka "Control of rotary series elastic actuator for ideal force-mode actuation in human–robot interaction applications"*IEEE/ASME transactions on mechatronics, Volume 14*, 2009.

[36] K. Kong, J. Bae, and M. Tomizuka "A compact rotary series elastic actuator for human assistive systems"*IEEE/ASME transactions on mechatronics, Volume 17*, 2012.

[37] N. Tsagarakis, M. Laffranchi, B. Vanderborght, D. Caldwell "A compact soft actuator unit for small scale human friendly robots"*Robotics and Automation, 2009. ICRA'09. IEEE International Conference on*, 2009.

[38] R. Wang, H. Huang "An active-passive variable stiffness elastic actuator for safety robot systems"*Intelligent Robots and Systems (IROS), 2010 IEEE/RSJ International Conference on*, 2010.

[39] G. Wyeth "Demonstrating the Safety and Performance of a Velocity Sourced Series Elastic Actuator "*IEEE International Conference on Robotics and Automation*, 2008.

[40] D. Ruffoni, "Biomechanics," *Lecture 1, slide 25*, 2016-2017.

[41] O. Brüls, "Robotique biomédicale et prothèses actives," 2016-2017.

[42] J.-C. Golinval, "Vibration testing and experimental modal analysis", 2016-2017.

[43] `http://www.qualisys.com/applications/medical/gait-rehab/`, consulted on February 20, 2017.

[44] `http://www.mogi.bme.hu/TAMOP/robot_applications/ch07.html`, consulted between March 20-24, 2017.

[45] `http://www.mecholic.com/2016/01/electromagnetic-clutch-working-application-advantages.html`, consulted on April 6, 2017.

[46] `https://en.wikipedia.org/wiki/Electromagnetic_clutch`, consulted on April 6, 2017

[47] `http://www.keywordhut.com/aGFybW9uaWMgZHJpdmUgYW5pbWF0aW9u/`, consulted on April 3, 2017.

[48] `http://ctms.engin.umich.edu/CTMS/index.php?example=MotorSpeed&section=SystemModeling`, consulted between March 24-28, 2017

[49] `http://www.orthobullets.com/foot-and-ankle/7001/gait-cycle`, consulted on February 27, 2017.

[50] `http://www.physio-pedia.com/Gait#The_Gait_Cycle`, consulted on February 27, 2017.

[51] `http://biomec.upc.edu/project-items/hybor-low-cost-motor-fes-hybrid-orthosis-gait-spinal-cord-injured-subjects-simulation-methods-support-design-adaptation/`, consulted on February 20, 2017.